Università degli studi di Napoli "Federico II"

DOTTORATO DI RICERCA IN FISICA

Ciclo XXIX

Coordinatore: prof. Salvatore Capozziello

$\nu_\mu \rightarrow \nu_\tau$ oscillations with the OPERA experiment

Settore Scientifico Disciplinare FIS/01

Dottoranda
Giuliana Galati

Tutori
Prof. Giovanni De Lellis
Dott.ssa Maria Cristina Montesi

Anni 2014/2017

Contents

Introduction

Originated by the neutrino mass and the mixing between flavour and mass eigenstates, neutrino oscillations are now established thanks to several experimental efforts. In 1998, the first evidence for neutrino oscillations was provided by the Super-Kamiokande experiment, showing the disappearance of muon neutrinos produced in the atmosphere [1]. This result was interpreted as a possible transition from muon to tau neutrinos. An overview about the theoretical model and neutrino oscillation experiments is given in Chapter 1.

The OPERA experiment was conceived to demonstrate unambiguously the $\nu_\mu \to \nu_\tau$ oscillation by directly observing the τ lepton produced in charged-current ν_τ interactions. It was operated underground in the Gran Sasso INFN Laboratory (LNGS), 730 km away from the muon neutrino source, from 2008 to 2012, integrating a beam intensity of 1.8×10^{20} protons on target. Its apparatus was hybrid, consisting of nuclear emulsions acting as the micrometric tracking device to detect the τ lepton production and decay vertex, and electronic detectors for the muon measurement and for the time stamp of the interaction. The whole apparatus is described in Chapter 2.

My PhD work is focused on the study of $\nu_\mu \to \nu_\tau$ oscillations within this experiment. The appearance of the τ lepton relied on the detection of its characteristic decay topologies into 1-prong (hadron, muon or electron) or 3 hadrons. To improve the rejection of the background due to hadron re-interactions, I have implemented a specific analysis for large angle track search ($\tan\theta \leq 3$ rad) using a new microscope scanning system, developed by the Napoli group. I have applied this new analysis to the validation of the fifth ν_τ candidate, as reported in Chapter 3. With the observation of 5 ν_τ candidates satisfying stringent kinematic selection criteria, $\nu_\mu \to \nu_\tau$ appearance was claimed by the Collaboration in 2015 with a significance of 5.1σ [2].

After demonstrating $\nu_\mu \to \nu_\tau$ oscillations, the Collaboration has set a new goal: measure Δm^2_{23}, for the first time in appearance mode, and the ν_τ cross section, so far measured only by the DONuT experiment, that however could not separate ν_τ from $\bar{\nu}_\tau$ [3]. To reduce the statistical uncertainty, I studied a new strategy for the ν_τ selection, described in Chapter 4, replacing the stringent kinematical cuts with

looser ones. I evaluated the corresponding increase in the expected background and optimized the analysis by minimising the uncertainty of the measurements.

To study the new ν_τ candidates, I have applied the Boosted Decision Tree method, a multivariate machine learning method used to classify observations. I evaluated Δm^2_{23} and ν_τ cross section using the enlarged candidate events. Furthermore, I performed the first measurement of the leptonic number of τ neutrinos, never done before. The significance of the observation of $\nu_\mu \to \nu_\tau$ oscillations with this new analysis has been estimated using different approaches. All results are reported in Chapter 5.

Chapter 1

Neutrino Physics

1.1 Neutrino discovery

It was 1930 when Wolfgang Pauli postulated the existence of neutrinos to explain the continuous β decay spectrum, a puzzling issue for scientists.
Radioactivity had been discovered in 1896 by Henri Becquerel. Since the 1920s, physicists were confused: the phenomenon of β-decay (in which an electron is emitted from the atomic nucleus) seemed to violate conservation laws. Differently from both α and γ decay, where the resulting particle has a narrow energy distribution, due to the fact the particle carries the energy given by the difference between the initial and final nuclear states, the kinetic energy distribution of β particles measured by Lise Meitner and Otto Hahn in 1911 and by Jean Danysz in 1913 showed multiple lines. These measurements offered the first hint that β particles have a continuous spectrum. In 1914 James Chadwick made more accurate measurements which showed that the spectrum was continuous [4]. If β decay was simply an electron emission as assumed at that time, then the energy of the emitted electron should have a particular, well-defined value [5]. For β decay, however, the observed broad distribution of energies suggested that energy is lost in the β decay process.
This spectrum was puzzling for many years. Böhr, for example, suggested that the energy in microworld was conserved only on average, not on an event-by-event basis. Pauli, instead, in his "Open letter to the group of radioactive people at the Gauverein meeting in Tübingen" suggested a new idea [6]:

Dear Radioactive Ladies and Gentlemen,
as the bearer of these lines, to whom I graciously ask you to listen, will explain to you in more detail, because of the "wrong" statistics of the N- and Li-6 nuclei and the continuous β spectrum, I have hit upon a desperate remedy to save the "exchange theorem" of statistics and the law of conservation of energy. Namely, the possibil-

ity that in the nuclei there could exist electrically neutral particles, which I will call neutrons, that have spin 1/2 and obey the exclusion principle and that further differ from light quanta in that they do not travel with the velocity of light. The mass of the neutrons should be of the same order of magnitude as the electron mass and in any event not larger than 0.01 proton mass.
The continuous beta spectrum would then make sense with the assumption that in beta decay, in addition to the electron, a neutron is emitted such that the sum of the energies of neutron and electron is constant.
Now it is also a question of which forces act upon neutrons. For me, the most likely model for the neutron seems to be, for wave-mechanical reasons (the bearer of these lines knows more), that the neutron at rest is a magnetic dipole with a certain moment μ. The experiments seem to require that the ionizing effect of such a neutron cannot be bigger than the one of a gamma-ray, and then μ is probably not allowed to be larger than $e \cdot (10^{-13} cm)$. [...]
I admit that my remedy may seem almost improbable because one probably would have seen those neutrons, if they exist, for a long time. But nothing ventured, nothing gained, and the seriousness of the situation, due to the continuous structure of the beta spectrum, is illuminated by a remark of my honored predecessor, Mr Debye, who told me recently in Bruxelles: "Oh, It's better not to think about this at all, like new taxes." Therefore one should seriously discuss every way of rescue. Thus, dear radioactive people, scrutinize and judge. - Unfortunately, I cannot personally appear in Tübingen since I amindispensable here in Zürich because of a ball on the night from December 6 to 7.
With my best regards to you, and also to Mr. Back, your humble servant,

W. Pauli

Pauli did not expect that his hypothetical new particle would ever be observed.

In 1932, a new heavy neutral particle, called "neutron", was observed by J. Chadwick [7, 8]. But this particle was different from the "neutron" that Pauli had postulated to explain his theory of β-decay. In order to distinguish the neutron of W. Pauli from the light neutron of J. Chadwich, Edoardo Amaldi jokingly coined the name "neutrino", which entered the scientific vocabulary through Enrico Fermi.

Fermi not only gave the name to the particle, but also introduced his four fermion theory of β-decay of nuclei in 1934 [9]. He assumed that nuclei are bound states of protons and neutrons and, using the analogy from QED, assumed that electrons and neutrinos are produced by a quantum transition of neutron into a proton:

$$n \to p + e^- + \nu \tag{1.1.1}$$

Soon after the neutrino was proposed as a new particle, physicists started to think about possible ways of detecting it, a difficult task due to their very small interaction

cross section, which was first estimated by Bethe and Peierls [10] to be $\leq 10^{-44}$ cm^2. For this reason the general opinion was that neutrinos were undetectable particles.

1.1.1 ν_e

It took about 25 years to detect the electronic neutrino. It was clear that a very intensive source of neutrinos as well as a heavy target were needed in order to establish its existence. When the first nuclear reactors were constructed in the 1940s, Fermi and Pontecorvo realized that they were high-flux sources of neutrinos. The estimated neutrino flux was as high as $10^{12} - 10^{13}$/s·cm^2, many orders of magnitude larger than the corresponding flux from ordinary radioactive sources.

In 1956 following the idea of Wang Ganchang to use β capture to experimentally detect neutrinos [11], Clyde Cowan and Frederick Reines published confirmation that they detected the electron neutrino [12], a result that was rewarded almost 40 years later with the 1995 Nobel Prize [13].

The experiment used a target made of 400 litres of a mixture of cadmium chloride and water, surrounded by photomultiplier tubes, placed near a nuclear reactor [14]. $\bar{\nu}_e$ coming from Savannah River reactor were detected through the observation of the inverse β-decay:

$$\nu^- + p \rightarrow e^+ + n \tag{1.1.2}$$

The signal was a 5 μs delayed coincidence between the two photons produced in the positron annihilation and another γ from neutron capture.

1.1.2 ν_μ

In 1959 an experiment was proposed independently by B. Pontecorvo [15] and M. Schwartz [16], using pions that were produced by a proton beam hitting a carbon target, in order to understand whether the same kind of neutrino could explain the decay of π^- and μ in cosmic rays. In 1962, L.M. Lederman, M. Schwartz, J. Steinberger *et al.* detected muon neutrino using a neutrino accelerator with an experiment carried out at Brookhaven National Laboratory.
To obtain the π^+ beam, a 15 GeV/c proton beam hit a beryllium target, producing a beam of π^+ which decayed into muons and neutrinos. A shielding material was located at the end of the decay tunnel, absorbing all charged particles. The neutrino detector was a sparkle chamber of 10 tons, which could observe the charged lepton produced in the neutrino interactions. 29 muon events were detected, while 6 detected electron candidates were explained by the background.
Therefore, by 1962 it became clear that two kinds of neutrinos exist: one associated with electrons and one with muons [17].

In 1988, L.M. Lederman, M. Schwartz, J. Steinberger were awarded a Nobel Prize for the discovery of muon neutrino and for developing the neutrino beam method. The discovery of the second neutrino type was a proof for existence of al least two different lepton families.

1.1.3 ν_τ

Having already discovered two leptons, scientists formulated the hypothesis that other leptons, heavier than muon could exist, and so other neutrinos associated to those leptons.

In 1957-1977, with the e^+e^- collider at Stanford, M. Perl *et al.* discovered the third lepton, namely the τ particle [18]. In 1989, the study of the Z boson width at LEP (Large Electron-Positron Collider) showed that only three neutrinos exist [19].

In 2001, the existence of the expected neutrino associated to the τ lepton was confirmed by the DONUT experiment at Fermilab [3, 20]. DONUT was conceived to observe ν_τ charged current interactions through to the identification of the τ lepton created at the interaction vertex. The high spatial resolution needed to resolve the short τ decay was obtained thanks to nuclear emulsion detectors. Nuclear emulsions had been widely used in the 1940-1960s, leading, for example to the discovery of the charged pion in 1947, thanks to Powell and Occhialini [21]. Then, faster and more digitally oriented modern devices were preferred for big experiments. However, nuclear emulsions have benefits that the latest detectors cannot compete with: they can resolve particle tracks with a micrometric resolution, providing data about the mass, energy, and modes of interaction and decay of incident particles. For this reason, only using nuclear emulsions the extremely short decays of the τ produced by tau neutrinos interacting in the detector could be detected.
The DONUT neutrino beam was created using 800 GeV protons from the Fermilab Tevatron interacting in a tungsten beam dump. When protons collide with tungsten nuclei, they produce D_s, along with other charmed hadrons such as D^+. The primary source of ν_τ is the decay of D_s into a τ and ν_τ; a smaller contribution (14%) comes from secondary interactions of D_s in the dump, D^+ decays and B meson decays. At the end of the experiment, 9 ν_τ charged current interactions were observed, from a total of 578 neutrino interactions.

1.2 Neutrinos in the Standard Model

The Standard Model (SM) [22, 23] of Particle Physics is the theory which describes the weak, electromagnetic and strong interactions of particles by exchanging spin-1 gauge bosons. The theory is renormalizable and gauge-invariant. Including the

quantum field theory of strong interactions (QCD) and the unified theory of electromagnetic and weak interactions, the SM turned out to be an extremely successful description of matter at the fundamental level.

In the SM, fermions are divided into two main groups: one made of 6 quarks, which have fractional charge, and the other one composed by 6 leptons, with integer charge. Leptons are subdivided into 3 families. All fermions have their anti-particle which differs in charge, lepton number for leptons and chirality.

The strong interaction is due to 8 massless gluons, while the electromagnetic one to a massless photon, and the weak interaction is mediated by the massive $W^{\pm}$ and Z^0 bosons.

The discovery, by ATLAS [24] and CMS [25] experiments at CERN, of the Higgs boson, the particle that generates the mass of all other particles, has completed the SM puzzle.

Neutrinos in the SM are assumed to be massless, electrically neutral, weakly interacting particles with spin $^1/_2$. They come in three flavours: ν_e ($\bar{\nu}_e$), ν_μ ($\bar{\nu}_\mu$) and ν_τ ($\bar{\nu}_\tau$). In the SM, lepton numbers are conserved and neutrino flavours do not change. Goldhaber, Grodzins and Sunyar, in 1957, showed that neutrinos are left handed and anti-neutrinos are right handed particles [26].
Neutrinos' weak interactions are mediated by $W^{\pm}$ and Z^0 bosons. If the interaction is mediated by the $W^{\pm}$, it is said "*charged current interaction*". In this process the $W^{\pm}$ couples to the neutrino and to a charged lepton from the same family: $W^{\pm} \rightarrow l_i^{\pm} + \nu_i(\bar{\nu}_i)$, where $i = e$, μ or τ. The boson Z^0, instead, mediates the "*neutral current interaction*", in which it is exchanged between neutrino or quark pair.

1.3 Neutrinos beyond the Standard Model

In the SM, fermions get mass through the Spontaneous Symmetry Breaking (ssb).

The Yukawa interaction describes the coupling between the Higgs field and massless quark and lepton fields. The mass that fermions acquire through the ssb is proportional to the vacuum expectation value of the Higgs field v:

$$m_i = \frac{Y_i v}{\sqrt{2}} \tag{1.3.1}$$

having denoted with Y_i the Yukawa coupling. Neutrino masses in the eV range require that Y_i is 10^{-11} or smaller, being $v \sim 246$ GeV. The introduction of such small coupling constants into a theory is generally considered unnatural.

Nevertheless, since 1998, several experiments have proven that neutrinos oscillate and so they are massive particles [27]. Neutrino oscillation theory says that each neutrino flavour is a mixture of the neutrino mass eigenstates and that oscillations

can happen only if mass eigenstates and flavour eigenstate do not coincide and neutrinos have non-zero masses: if each neutrino type has a different mass, during its propagation in space and time its flavour changes periodically. The existence of neutrino oscillations is one example of physics beyond the Standard Model.
So, despite its success, the SM cannot be considered as a final theory of the particle physics and cannot describe completely neutrinos. Neutrino oscillation results, indeed, show a strong evidence for the need of an extension of the SM.

1.3.1 Neutrino masses

In the SM, two types of mass exist for fermions: Dirac and Majorana. All massive fermions, both quark and leptons, have Dirac masses. In this case there exists a lepton charge carried by each neutrino which is conserved by the particle interactions and particle and antiparticle are distinct, since $L(\nu_i) = -L(\nu_i)$. A massive Majorana particle, instead, is identical with its antiparticle and lepton charge is not conserved. Only neutral fermions can have Majorana masses, otherwise charge conservation would be violated.

Neutrinos could have both mass terms.

Dirac mass terms are:

$$m_D \bar{\Psi}_L \Psi_R + h.c. \tag{1.3.2}$$

where Ψ_L and Ψ_R are Weyl spinor fields and m_D couples to right-handed and left-handed fields.

Majorana mass terms, instead, are:

$$m_M = \Psi^{\bar{C}}_{R(L)} \Psi^{C}_{R(L)} \tag{1.3.3}$$

where m_M is the Majorana term and C the charge conjugation matrix. Majorana mass couples right fields or left fields to themselves. Since only one Weyl spinor is necessary to generate a Majorana mass term, there are only two degrees of freedom with the same mass. When more neutral fields exist, therefore, m_M becomes a symmetric matrix:

$$(m_M)_{ij} (\bar{\Psi^C_R})_i (\Psi_R)_j \tag{1.3.4}$$

where i and j ranges from 1 to the number of neutral fields.

The most general neutrino mass term contains both Dirac and Majorana terms:

$$-L = (\bar{\nu_L} \bar{\nu^c_L}, \bar{\nu_R} \bar{\nu^c_R}) M \begin{pmatrix} \nu_L + \nu^c_L \\ \nu_R + \nu^c_R \end{pmatrix} \tag{1.3.5}$$

being the mass matrix M defined as:

$$M = \begin{pmatrix} m_t & m_D \\ m_D^T & m_s \end{pmatrix} \tag{1.3.6}$$

For three generations, m_t, m_D and m_s are complex matrices 3×3, while ν_L and ν_R are 3-components vectors: $\nu_L = (\nu_{eL}, \nu_{\mu L}, \nu_{\tau L})$.

See-saw mechanism

In many extension of the SM, like the Grand Unified Theory (GUT), massive neutrinos are introduced and lepton number is not conserved.
In the GUT, neutrino mass is generated through the *See-saw* mechanism [28], and its mass term is Dirac-Majorana. In this hypothesis, there is a hierarchy between the mass matrix elements given in eq. 1.3.6, so that m_s elements are larger than m_D ones, while m_t elements are negligible with respect to the others. In this assumptions, eq. 1.3.6 becomes:

$$M = \begin{pmatrix} 0 & m_D \\ m_D^T & M \end{pmatrix} \tag{1.3.7}$$

Diagonalizing the mass matrix, one obtains six Majorana neutrinos: three of them are light and active, while the other three are heavy and sterile, which means that they can interact with matter only through the gravitational force. These neutrinos will have mass eigenvalues ($i = 1, 2, 3$) equal to:

$$\begin{aligned} m_{\nu_i} &\simeq \frac{m_{D_i^2}}{M_i} \\ m_{N_i} &\simeq M_i \end{aligned} \tag{1.3.8}$$

where m_{D_i} are the masses of the quarks *up, charm* and *top*, ($m_{D_i} = (m_u, m_c, m_t)$) or lepton masses ($m_{D_i} = (m_e, m_\mu, m_\tau)$) according to the model. Eigenvalues M_i define the scale at which new physics shows up.

This mechanism could explain why neutrinos have such a different mass from charged leptons. In the See-saw models, M_i elements are not fixed. The See-saw mechanism is said to be *quadratic* if the M_i elements are considered equal to each other, since $m_{\nu_i} \propto m_{D_i}^2$. Otherwise a hierarchy similar to the one of charged leptons or quarks can be assumed and the See-saw mechanism is *linear*: $m_{\nu_i} \propto m_{D_i}$.

The possible range of the magnitude order of the mass matrix elements is very wide, going from 10^{10} to 10^{16} GeV or even down in the extension of the neutrino

minimal standard model by three right-handed neutrinos with masses smaller than the electroweak scale [29].

Generally the quadratic mechanism is used and so:

$$m_{\nu_1} : m_{\nu_2} : m_{\nu_3} = m_e^2 : m_\mu^2 : m_\tau^2 \tag{1.3.9}$$

$$m_{\nu_1} : m_{\nu_2} : m_{\nu_3} = m_u^2 : m_c^2 : m_t^2 \tag{1.3.10}$$

Having introduced a mass term for neutrinos implies a mixing between them, independently from their nature (Dirac or Majorana). If this mixing exists and their spectrum is not degenerate, oscillations between neutrino flavours happens.

Neutrino mass measurements

Up to now, no experiments managed to measure the tiny mass of neutrinos, so only upper limits are available.

Limits for the electron neutrino mass can be obtained by measuring the end-point of the electron spectrum in Tritium decay [30, 31, 32, 33, 34] and from cosmological and astrophysical data. The most stringent upper bounds on the ν_e mass were obtained in the Troitzk experiment [34]:

$$m_{\nu_e} < 2.05 \text{ eV } (95\% \ C.L.) \tag{1.3.11}$$

Similar result was obtained in the Mainz experiment [32]: $m_{\nu_e} < 2.3$ eV at 95% C.L.

The mass of the muon neutrino can be determined from momentum analysis of pion decay $\pi^+ \to \mu^+ \nu_\mu$ and its upper limit is [35]:

$$m_{\nu_\mu} < 0.17 \text{ MeV } (90\% \ C.L.) \tag{1.3.12}$$

The mass of the tau neutrino is derived by fitting the visible energy versus the invariant mass in the process: $\tau^- \to 3\pi^- + 2\pi^+ + \nu_\tau(+\pi^0)$ and it is [36]:

$$m_{\nu_\tau} < 18.2 \text{ MeV } (95\% \ C.L.) \tag{1.3.13}$$

The Cosmic Microwave Background (CMB) data of the WMAP experiment, combined with data on galaxy clustering and supernovae, is used to obtain an upper limit on the sum of neutrinos masses [37]:

$$\sum m_\nu < (0.3 - 1.3) \text{ eV } (95\% \ C.L.) \tag{1.3.14}$$

The Planck Collaboration put a more stringent constraint [38]. In the assumption of the existence of three light massive neutrinos and the validity of the Λ

Cold Dark Matter model, the Planck Collaboration used data on the CMB spectrum anisotropies, polarization, gravitational lensing effects, supernovae and Baryon Acoustic Oscillations, obtaining the following limit:

$$\sum m_\nu < 0.23 \text{ eV } (95\% \ C.L.) \tag{1.3.15}$$

1.4 Neutrino Oscillation and matter effect

In 1957, Bruno Pontecorvo hypotized that neutrinos produced in weak interaction could be a state superimposion of two different massive neutrinos [39]. The idea of mixing between neutrinos of different flavours was then proposed by Maki, Nakagawa and Sakata in 1962 [40] and investigated in 1969 by Gribov and Pontecorvo [41].

If we assume that neutrino is massive, and that weak interaction eigenstates do not coincide with mass eigenstates, its eigenstate of weak interaction can be expressed as a superimposition of eigenstates ν_i with mass m_i, where i runs on the number of flavours:

$$\nu_l = \sum_{i=1}^{3} U_{l_i}^* \nu_i \tag{1.4.1}$$

where U_{l_i} is a unitary mixing matrix. In the following, we assume that $m_1 \leq m_2 \leq m_3$. Let's consider a neutrino beam in vacuum, propagating along x axis with a defined momentum p_ν. Then $\forall i$:

$$E_i = \sqrt{(p_\nu^2 + m_i^2)} \approx p_\nu + \frac{m_i^2}{2p_\nu} \tag{1.4.2}$$

where the approximation relies on the fact that $m_i \ll p_\nu$.
If the beam is created in $x = 0$ at the time $t = 0$, the weak eigenstate at a given (x, t) is described by the wave function:

$$\Psi(x,t) = \sum_i U_{l_i}^* e^{ip_\nu x} e^{-iE_i t} \nu_i(0) \approx e^{ip_\nu(x-t)} \sum_i U_{l_i}^* e^{-\left(\frac{m_i^2}{2p_\nu}\right)t} \nu_i(0) \tag{1.4.3}$$

Transition probability between two eigenstates with different flavour at time t and distance $x = L \approx t$ is given by:

$$P_{ll'} = |\langle \nu_{l'} | \nu_l \rangle|^2 = \left| \sum_{k=1}^{3} U_{l'k} e^{-iE_k t} U_{lk}^* \right|^2 \tag{1.4.4}$$

where U^*_{lk} is the probability to find the mass eigenstate ν_k and energy E_k in a flavour eigenstate ν_l at a generic instant t, while the factors $e^{-iE_k t}$ and $U_{l'k}$ indicate, respectively, time evolution of the mass eigenstate and the transition probability of $\nu_{l'}$ in ν_k.

According to unitarity relation, $\left(\sum_{k=1}^{3} U_{l'k}U^*_{lk} = \delta_{l'l}\right)$, one gets:

$$P_{ll'} = \left|\delta_{ll'} + \sum_{k=2}^{3} U_{l'k}U^*_{lk}\left[exp\left(-i\frac{\Delta m^2_{k1}L}{2E}\right) - 1\right]\right|^2 \tag{1.4.5}$$

where we used 1.4.2 and took into account that $\Delta m^2_{kj} = m^2_k - m^2_j$.
The probability $P_{ll'}$ depends on the elements of the mixing matrix, on the factor $|\Delta m^2_{k1}|\,(k = 2, 3)$ and on the parameter L/E, whose range is determined by the experimental apparatus.

If there was no mixing ($U = I$) and/or $\frac{\Delta m^2_{k1}L}{E} \ll 1$, there would be no transition between different flavours.

In case the oscillation occurs between two flavours only, we get:

$$P_{ll'} = \left|\delta_{l'l} + U_{l'2}U^*_{l2}\left[exp\left(-i\frac{\Delta m^2 L}{2E}\right) - 1\right]\right|^2 \tag{1.4.6}$$

where $\Delta m^2 = m^2_2 - m^2_1$ and, being the unitary matrix U elements being expressed in function of the mixing angle θ:

$$U = \begin{pmatrix} \cos\theta & \sin\theta \\ -\sin\theta & \cos\theta \end{pmatrix}$$

the oscillation probability results:

$$P_{ll'} = \sin^2(2\theta)\sin^2\left(1.27\frac{\Delta m^2 L}{E}\right) \tag{1.4.7}$$

where L is measured in m (km), E in MeV (GeV) and m in eV.
Equation 1.4.7 shows that $P_{ll'}$ is a periodic function of L/E, where L is the distance between the neutrino source and the detector and E is the neutrino energy.
The amplitude of the oscillation is $\sin^2 2\theta$ and the oscillation length:

$$L_{oscill} = \frac{2.48E}{\Delta m^2} \tag{1.4.8}$$

If we consider all three flavours, the mixing matrix is parametrized by three angles, which can be denoted as θ_{12}, θ_{13} and θ_{23} and a phase δ for CP violation.
The unitary mixing matrix connecting flavour and mass eigenstates

$$\begin{pmatrix} \nu_e \\ \nu_\mu \\ \nu_\tau \end{pmatrix} = \begin{pmatrix} U_{e1} & U_{e2} & U_{e3} \\ U_{\mu 1} & U_{\mu 2} & U_{\mu 3} \\ U_{\tau 1} & U_{\tau 2} & U_{\tau 3} \end{pmatrix} \begin{pmatrix} \nu_1 \\ \nu_2 \\ \nu_3 \end{pmatrix} \tag{1.4.9}$$

gets the form:

$$\begin{pmatrix} 1 & 0 & 0 \\ 0 & \cos\theta_{23} & \sin\theta_{23} \\ 0 & -\sin\theta_{23} & \cos\theta_{23} \end{pmatrix} \begin{pmatrix} \cos\theta_{13} & 0 & \sin\theta_{13}e^{-i\delta} \\ 0 & 1 & 0 \\ -\sin\theta_{13}e^{-i\delta} & 0 & \cos\theta_{13} \end{pmatrix} \begin{pmatrix} \cos\theta_{12} & \sin\theta_{12} & 0 \\ -\sin\theta_{12} & \cos\theta_{12} & 0 \\ 0 & 0 & 1 \end{pmatrix} \tag{1.4.10}$$

Separation in sub-matrices also shows the different experimental areas. Atmospheric and long baseline accelerator experiments have measured θ_{23}; reactor and accelerator experiments have measured θ_{13}, while solar experiments have measured θ_{12}. δ phase can bring to CP violation in neutrino oscillations, which is very difficult to verify experimentally. First results find the best fit value of $\delta = 3\pi/2$ [42, 43, 44].

CP violation in the leptonic sector could be one of the necessary ingredients to explain the asimmetry in the Universe between barions and anti-barions, since CP violation for quarks, the only source of CP violation known up to now, is not sufficient to explain it.

Neutrino oscillation experiments measure the squared mass differences instead of the absolute mass, therefore the mass ordering is not yet known.
Considering three neutrino mass eigenstates ν_1, ν_2, ν_3, there are three mass differences Δm^2_{ij}, for which, of course, $\Delta m^2_{23} + \Delta m^2_{12} + \Delta m^2_{13} = 0$. Present measurements determined Δm^2_{12} (often indicated also as $m^2_\odot$) for solar neutrinos and Δm^2_{23} (often indicated also as Δm^2_{atm}). From these measurements it is not possible to know the mass ordering. If $m_3 \gg m_2 > m_1$ it is said *normal hierarchy*, while $m_3 \ll m_1 < m_2$ is defined as *inverted hierarchy* (see fig. 1.1).

The formalism described in section 1.4 was based on the assumption that neutrinos travel in vacuum from the source to the detector, but neutrinos travel through matter and may interact with it: indeed, neutrinos are scattered on electrons, protons and neutrons in matter [46].

First Wolfenstein and later Mikheyev and Smirnov figured out that the neutrino oscillation probabilities are strongly affected by the presence of matter, so this effect is called *Mikheyev-Smirnov-Wolfenstein effect* (MSW).

Neutrino scattering in matter occurs either via a Charged Current (CC) or Neutral Current (NC) reaction as shown in fig. 1.2. All the neutrino flavours participate to the neutral current interactions and this does not effect neutrino oscillations, while

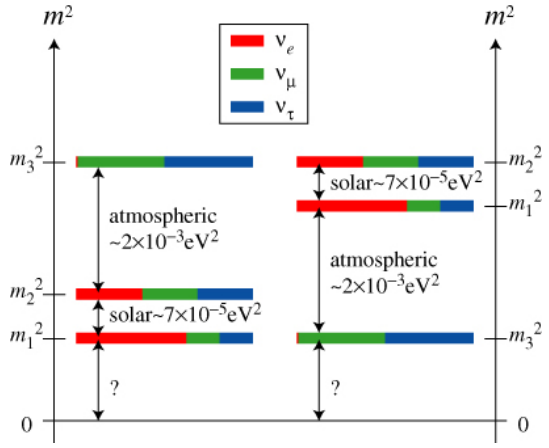

Figure 1.1. Neutrino masses spectra obtained from neutrino oscillation experiments [45]. The left plot represents the so called normal hierarchy, while the right plot is the inverted hierarchy.

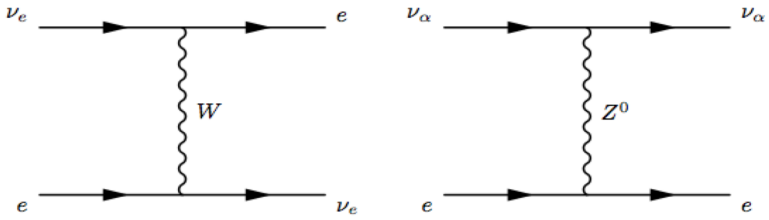

Figure 1.2. Charged current (CC) on the right and Neutral Current (NC) on the left neutrino interactions [47]

the charged current process can only occur for ν_e. This asymmetry between neutrino flavours creates an effective mass term and thus affects the mass splitting and flavour changing probabilities.

Electron neutrinos interact with electrons through the vector boson W and this scattering creates the following additional potential term in the Hamiltonian:

$$V_W = +\sqrt{2} G_F N_e \tag{1.4.11}$$

where G_F is the Fermi coupling constant and N_e the electron density. If we consider a $\bar{\nu}_e$ beam, V_W will be negative. If, instead, a vector boson Z is exchanged with an electron, proton or neutron, independently from the neutrino flavour, and in the hypothesis of a electrically neutral matter ($N_e = N_p$), the extra term of potential energy V_Z will be:

$$V_Z = -\frac{\sqrt{2}}{2} G_F N_n \tag{1.4.12}$$

since the contributions from electrons and protons to the interaction cancels and V_Z only depends from the neutron density. As before, if an antineutrino beam is considered, the sign of V_Z will be inverted.

Propagation of a neutrino through matter can be described with good approximation by the Schrödinger equation, which Hamiltonian can be obtained summing the contributions given in 1.4.11 and 1.4.12 to the Hamiltonian in vacuum. It can be demonstrated that [48]:

$$\mathcal{H} = \frac{\Delta m^2}{4E} \begin{bmatrix} -(\cos 2\theta - x) & \sin\theta \\ \sin\theta & (\cos 2\theta - x) \end{bmatrix} \tag{1.4.13}$$

where x stands for:

$$x \equiv \frac{V_W/2}{\Delta m^2/4E} = \frac{2\sqrt{2} G_F N_e E}{\Delta m^2} \tag{1.4.14}$$

The parameter x for neutrinos is positive in case of normal hierarchy and negative otherwise, the opposite for antineutrinos.

An asymmetry between neutrinos and antineutrinos oscillation is due to the MSW effect. From this asymmetry, hints about mass hierarchy could be derived.
Defining the quantity:

$$\Delta m^2_M \equiv \Delta m^2 \sqrt{\sin^2 2\theta + (\cos 2\theta - x)^2} \tag{1.4.15}$$

$$\sin^2 2\theta_M \equiv \frac{\sin^2 2\theta}{sin^2 2\theta + (cos 2\theta - x)^2} \tag{1.4.16}$$

the oscillation probability between two different flavours is given by:

$$P_M(\nu_l \to \nu_{l'}) = \sin^2 2\theta_M \sin^2 \left(|\Delta m^2_M| \frac{L}{4E} \right) \tag{1.4.17}$$

which differs from the vacuum one only for the replacement of θ and Δm^2 with the equivalent in matter.

1.5 Neutrino Oscillation Experiments

Since 1970, many evidences confirmed that neutrinos do oscillate. All neutrino detectors have masses of the order of tons, in order to compensate the small neutrino

cross section. Often they are placed underground to minimize the background due to cosmic rays. Experiments can be grouped according to the neutrino source used and the L/E range. When artificial neutrino sources are used, experiments can be classified as *short-baseline*, where L is of the order of some kilometres, and *long-baseline*, where L is of the order of hundreds of kilometres.

There are six ways to produce neutrinos:

- the Sun produces MeV ν_e in its nuclear fusion;
- stars emit MeV neutrinos during their gravitational collapse in Super-Novae;
- nuclear fission reactors produce $\bar{\nu}_e$ of about 1-10 MeV, which may travel for about 10 to 100 km, according to the detector position;
- cosmic rays interact with atmospheric nuclei originating ν_e and ν_μ called "*atmospheric neutrinos*" in a wide range of energy. The distance travelled are of the order of 10-20 km for neutrinos coming from overhead, of the order of 10^4 km for neutrinos that crossed the Earth;
- accelerators can produce neutrinos in a wide range of energy. Usually from the decay of π it is possible to obtain almost pure ν_μ and $\bar{\nu}_\mu$ beams with little ν_e contamination.

Measurement of Δm^2_{12} and θ_{12} with solar and reactor neutrino experiments

The nuclear fusion process in the core of the Sun produces solar neutrinos. In this process, neutrinos are produced exclusively with electron flavour in a wide energy spectrum, as shown in fig. 1.3.

The first solar neutrino detector was constructed in the 1960s, deep underground in the Homestake gold mine in Lead, South Dakota, by Raymond Davis Jr. The first results from Homestake experiment, in 1968, showed an observed flux much lower than the theoretical predictions of Solar Standard Model (SSM) [50], this being known as the "*solar neutrino problem*". Davis was given the 2002 Nobel Prize in Physics, being a pioneer in the detection of cosmic neutrinos based on radiochemical method.

Also other experiments confirmed that there was a deficit of about 30% with respect to what predicted by the standard solar model, but at that time it was not possible to exclude that the problem was in the solar model [51].

This deficit was also confirmed by Kamiokande (Kamioka Nucleon Decay Experiment) in 1989 [52]. The experiment used a water Cherenkov detector located in the Mozumi mine near Kamioka in Japan, about 1000 m underground and measured the

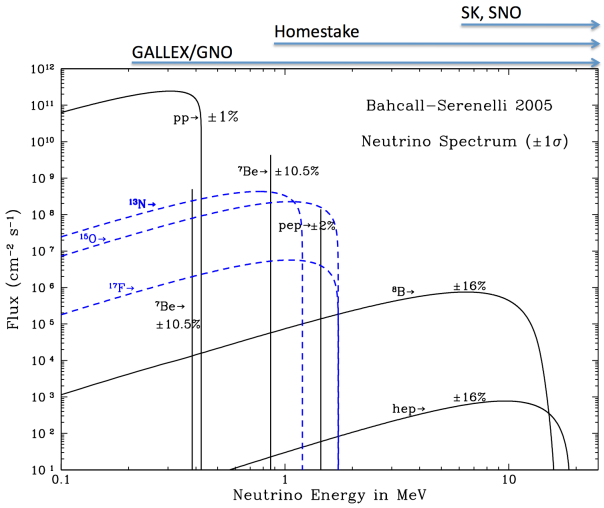

Figure 1.3. Solar neutrino fluxes according to the Standard Solar Model [49]. Continue lines are ν coming from the pp chain, while the dotted ones are the spectra from the CNO cycle. The three vertical lines correspond to processes with a final two body state and therefore the emitted neutrino is almost monochromatic. The arrows above the diagram indicate the energy ranges accessible to experiments

solar neutrino flux from ^{8}B through the elastic scattering reaction $\nu_x + e^- \rightarrow \nu_x + e^-$, with $x = e, \mu, \tau$. The average measured flux of ^{8}B neutrinos was about 50% lower than expected [53, 54]. A more precise result was later obtained by the next generation Super-Kamiokande experiment [55, 56, 57, 58].

By the end of the millennium it became clear that the discrepancy between the solar flux measurements and the SSM predictions could not be explained by large uncertainties and meanwhile the solar models had improved, showing that model predictions agree well with the independent helioseismological observations [59]. The only consistent hypothesis to explain the deficit of solar neutrinos was neutrino oscillations: some of the ν_e produced in the solar core might change flavour during propagation, becoming ν_μ or ν_τ, which are not detected by the radiochemical experiments on Earth and, due to differences in cross section, only partially detected by Kamiokande or Super-Kamiokande.

The puzzle was solved by the SNO solar neutrino experiment [60], which started observations in 1999. The SNO detector was built 2 km underground, in INCO's Creighton mine, near Sudbury, Ontario, Canada. It was a Cherenkov detector filled with 1000 tons of heavy water (D_2O), contained by a 12 m diameter acrylic vessel and instrumented with 9600 photomultiplier tubes.

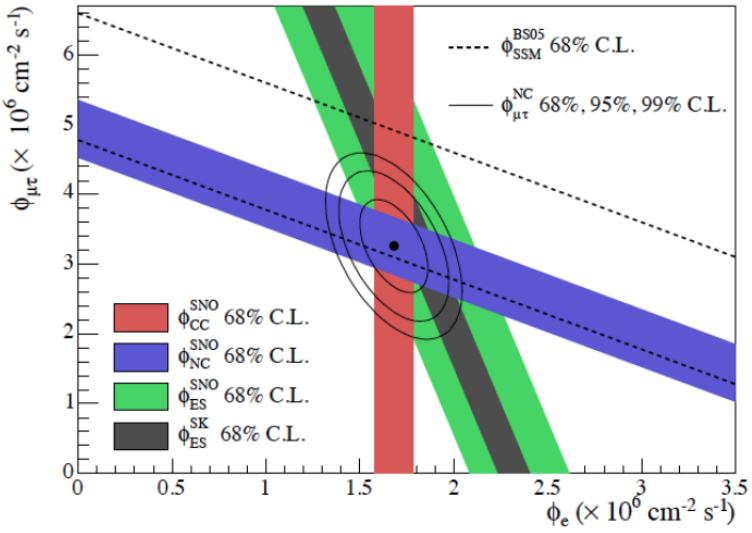

Figure 1.4. Neutrino fluxes from SNO [61]. The x axis shows ν_e flux, the y axis flux of other neutrinos. The red band shows the result of the CC analysis, only sensitive to ν_e. The blue band is the NC analysis, equally sensitive to all types. The band between the dotted lines is the total ν flux expected in the Solar SM

SNO detected ^{8}B solar neutrinos via the reactions:

$$\begin{aligned} \text{Charged Current (CC): } \nu_e + {}^2H &\rightarrow e^- + p + p \\ \text{Neutral Current (NC): } \nu_x + {}^2H &\rightarrow \nu_x + p + n \\ \text{Elastic Scattering (ES): } \nu_x + e^- &\rightarrow \nu_x + e^- \end{aligned} \tag{1.5.1}$$

The CC reactions are sensitive only to ν_e and provide the flux $\phi(\nu_e)$, while NC reactions to all neutrino flavours $\phi(\nu_e) + \phi(\nu_\mu) + \phi(\nu_\tau)$. ES reactions occur for all three flavours, but are predominant for ν_e.

SNO measured ϕ CC flux as $1.76 \pm 0.06(stat) \pm 0.09(syst) \times 10^6$ cm^{-2} s^{-1} while ϕ NC flux was $5.09 \pm 0.44(stat) \pm 0.46(syst) \times 10^6$ cm^{-2} s^{-1} which was a clear confirmation of neutrino flavour changing [61]. SNO was able to confirm that the total neutrino flux ($\phi_e + \phi_\mu + \phi_\tau$) was consistent with the solar models. The deficit in the ν_e flux was compensated by a non-zero ν_μ and ν_τ fluxes as a result of the neutrino oscillation. A comparison with the total ^{8}B flux, indeed, demonstrated that about two thirds of the solar ν_e changed flavour, arriving at Earth as ν_μ or ν_τ (see fig. 1.4).

The SNO evidence for neutrino flavour conversion was confirmed a year later by the KamLAND (Kamioka Liquid scintillator AntiNeutrino) reactor experiment [62, 63].

From the solar and nuclear reactors experiments we can get the oscillation parameters Δm^2_{12} and θ_{12}. The best-fit values with 3σ allowed ranges, derived from a global fit of the current neutrino oscillation data as summarised in [64], are:

$$\Delta m^2_{12} = 7.37^{+0.60}_{-0.44} \times 10^{-5}\ eV^2 \tag{1.5.2}$$

$$\sin^2\theta_{12} = 0.297^{+0.057}_{-0.047} \tag{1.5.3}$$

Measurement of Δm^2_{32} and θ_{23} with atmospheric and terrestrial neutrino

The oscillation parameters Δm^2_{32} and θ_{23} are obtained from the atmospheric neutrinos and the artificial neutrino beams.

Atmospheric neutrinos are produced in the decay of secondary particles, created in the collisions of the cosmic rays with the nuclei in the atmosphere. Cosmic rays are mainly protons ($\sim 80\%$), α particles ($\sim 15\%$) and a small fraction of heavy nuclei.

When primary cosmic rays hit the atmosphere, hadronic showers are produced, originating pions and kaons. Pions promptly decay into muons and ν_μ ($\bar{\nu}_\mu$). Muons travel long distance before decaying into electrons, ν_μ ($\bar{\nu}_\mu$) and ν_e ($\bar{\nu}_e$) neutrinos. At low energies ($\leq$1 GeV), the majority of μ decay before hitting Earth's surface, so the flux ratio of ν_μ to ν_e, defined as the sum of the fluxes of neutrinos and antineutrinos of a specific flavour, is expected to be ~ 2 [65]. First indications of deviations from the expected 2:1 ratio appeared in the middle of the 1980s [66]. The ratio R can be defined as:

$$R = \frac{\left[N\left(\nu_\mu + \bar{\nu}_\mu\right)/N\left(\nu_e + \bar{\nu}_e\right)\right]_{data}}{\left[N\left(\nu_\mu + \bar{\nu}_\mu\right)/N\left(\nu_e + \bar{\nu}_e\right)\right]_{theory}} \tag{1.5.4}$$

and should equal 1 in the hypothesis of no neutrino oscillation. However, experiments such as Kamiokande [67], IMB [68] and Soudan-2 [69] measured R significantly lower than one. This was known as the *atmospheric neutrino anomaly* and was interpreted as another indication of neutrino oscillations.

The second generation of Kamiokande experiment, called Super-Kamiokande, showed in fig. 1.5 (b), launched its operations in April 1996. Atmospheric neutrinos are produced high in the atmosphere and the flux at the surface of the Earth is expected to be isotropic, independent of the zenith angle. This implies that the observed fluxes of up-going and down-going neutrinos in an underground detector like SK should be equal, while SK reported a deficit in the number of up-going high energy muon-neutrinos, strongly varying with the zenith angle (i.e. the angle between the neutrino direction and vertical). Down-going neutrinos travel around 10-20 km before reaching the detector, while up-going neutrinos travel up to 12000 km. Therefore, by studying the neutrino flux as a function of the zenith angle, one can observe the modulation in the neutrino flux for different baselines, as shown in fig. 1.5 (a).

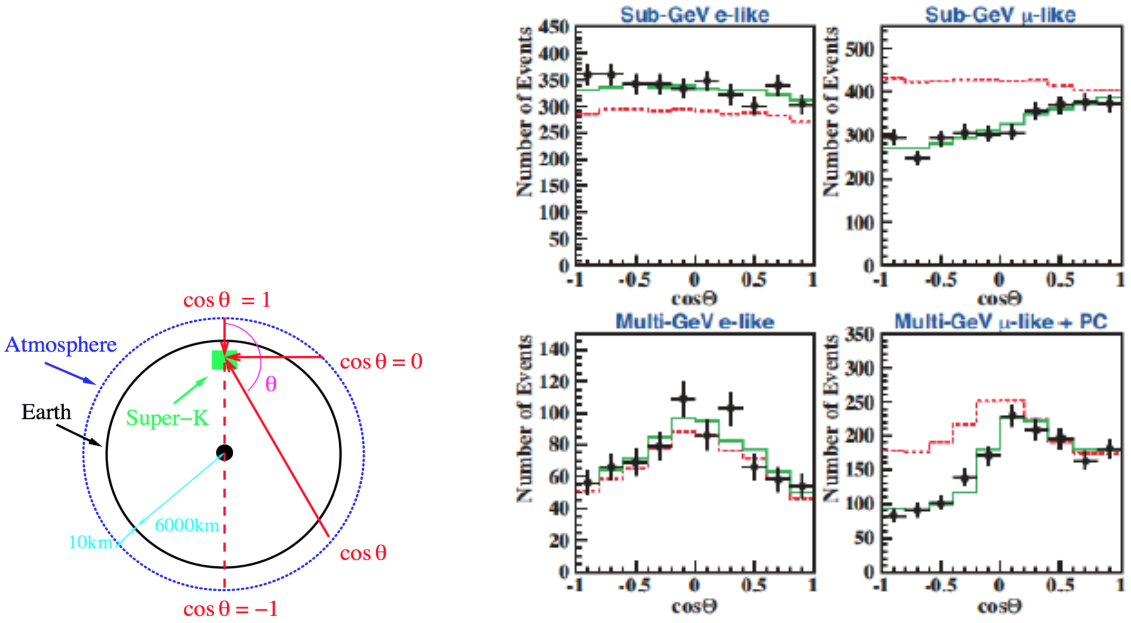

(a) (b)

Figure 1.5. (a) A sketch showing the relation between the zenith angle and the distance travelled by atmospheric neutrinos; (b) zenith angle distribution of fully contained 1-ring e-like and μ-like events in the Super-Kamiokande detector with visible energy below or above 1.33 GeV, corresponding to the Sub-GeV and Multi-GeV samples. The dashed curves show non-oscillated expected flux and solid curves show the best fit for $\nu_\mu \to \nu_\tau$ oscillation [1]

Results were presented by T. Kajita of the Super-Kamiokande Collaboration at the international neutrino conference Neutrino'98 [1]: strong discrepancy with respect to no-oscillation hypothesis was observed in the distributions of the cosine of the zenith angle for the sub-GeV and the multi-GeV muon-like events, while no significant asymmetry was detected for the e-like events (see fig. 1.5 (b)): since there is no indication of an increased ν_e flux, the missing ν_μ must have oscillated into ν_τ or into a new non-interacting "sterile" neutrino ν_x. The answer to this will be given by the OPERA experiment, which was conceived to directly and unambiguously detect the appearance of ν_τ in a ν_μ beam. Being the object of this thesis, the experiment and its results will be largely described in the following Chapters.

To confirm SK result, an experiment using a controlled neutrino source was needed. K2K (KEK to Kamioka) [70] was the first long-baseline neutrino oscillation experiment and used ν_μ beam created by 12 GeV protons by the KEK proton synchrotron. The beam was sent from the KEK to the Super-Kamiokande detector, located 250 km away. After exiting the pipe, neutrinos went through a 1-kiloton water Cherenkov neutrino detector called "near detector", located at about 300 m, used to determine the neutrino beam characteristics. The aim of the experiment was to measure the deficit in the far detector. K2K took data from 1999 to 2004 and confirmed the results of the Super-Kamiokande atmospheric neutrino oscillation with a significance of 4σ [71].

The present best results have been reported by MINOS (Main Injector Neutrino Oscillation Search experiment) [72]. MINOS used neutrinos from NuMI (Neutrinos at the Main Injector) neutrino beam created by 120 GeV protons at Fermilab. It was a disappearance experiment with 1 kton near detector and 5.4 kton far detector. Both the detectors were functionally identical, and used magnetized steel/scintillator calorimeters. The oscillation analysis was performed by comparing the observed ν_μCC rate with the expected one from the near detector. MINOS searched both for ν and $\bar{\nu}$ oscillations. Global best fit are shown in figure 1.6.

The best-fit values for normal (NH) hierarchy and inverted (IH) hierarchy with 3σ allowed ranges, derived from a global fit of the current neutrino oscillation data as summarised in [64], are:

$$\begin{aligned} \left|\Delta m^2_{23}\right| &= 2.50^{+0.13}_{-0.13} \times 10^{-3} eV^2 \text{ (NH)} \\ \left|\Delta m^2_{23}\right| &= 2.46^{+0.14}_{-0.13} \times 10^{-3} eV^2 \text{ (IH)} \end{aligned} \tag{1.5.5}$$

$$\begin{aligned} \sin^2\theta_{23} &= 0.437^{+0.179}_{-0.058} \quad \text{(NH)} \\ \sin^2\theta_{23} &= 0.569^{+0.068}_{-0.186} \quad \text{(IH)} \end{aligned} \tag{1.5.6}$$

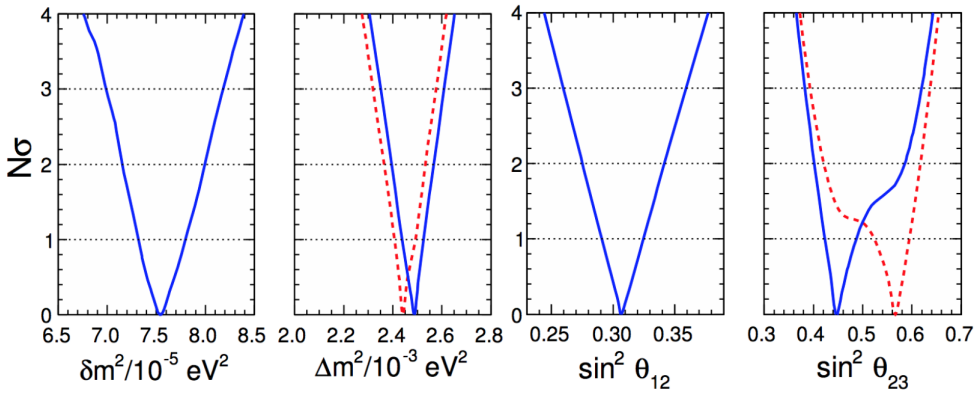

Figure 1.6. Global best fit for normal and inverted hierarchy using data from LBL, KamLAND, solar, SBL and atmospheric neutrinos [64]. $\delta m^2 = m_2^2 - m_1^2$; $\Delta m^2 = m_3^2 - (m_1^2 + m_2^2)/2$

Measurement of θ_{13}

For the oscillation parameter θ_{13} only an upper limit had been measured by the short baseline experiment CHOOZ [73, 74], which was the first one to observe $\bar{\nu}_e$ disappearance. It used neutrinos from two pressurized water reactors, which provide an almost pure ν_e source. A scintillator detector was located underground, 1 km far from the nuclear reactor core, to measure the $\bar{\nu}_e$ that are produced at a nuclear power plant in France. Neutrinos were observed via the inverse beta decay reaction:

$$p + \bar{\nu}_e \rightarrow n + e^+ \tag{1.5.7}$$

The CHOOZ experiment found $\sin^2 2\theta_{13} < 0.17$ [74].

The new generation experiments to measure θ_{13} follow two strategies:

- measure the disappearance of $\bar{\nu}_e$ from antineutrinos flux produced from reactors (Double-CHOOZ [75], RENO [76] and Daya Bay [77]);
- study the $\nu_\mu \rightarrow \nu_e$ oscillation, measuring the appearance of ν_e in a ν_μ beam generated by accelerators (T2K [78] and NOνA [79]).

In 2012, measurements from Double Chooz [80], RENO [81] and T2K [78] indicated $\theta_{13} \neq 0$. Later on, the Daya Bay reactor experiment measured the value of the $\sin_2^2 \theta_{13} = 0.092 \pm 0.016(stat.) \pm 0.005(syst.)$, with a significance of 5.2σ [82]. In 2013, T2K reported $\sin^2 2\theta_{13} = 0.140^{+0.038}_{-0.032}$ with 7.3σ [83].

The best-fit values with 3σ allowed ranges, derived from a global fit of the current

neutrino oscillation data as summarised in [64], are:

$$\begin{aligned} \sin^2\theta_{13} &= 0.0214^{+0.0032}_{-0.0029} \quad \text{(NH)} \\ \sin^2\theta_{13} &= 0.0218^{+0.0030}_{-0.0032} \quad \text{(IH)} \end{aligned} \tag{1.5.8}$$

The observation of non-zero θ_{13} opened a new scenario for CP-violation search in the neutrino sector.

1.6 Open questions

After the big experimental progresses made in the study of neutrino oscillations, further understanding of the pattern of neutrino masses and neutrino mixing, of their origins and of the status of CP symmetry in the lepton sector requires an extensive and challenging research program.

The first open question is the value of the CP phase δ, important since leptonic CP violation effects might have played a role for the baryon-antibaryon asymmetry in the universe through a mechanism called leptogenesis [33]. Latest results by the T2K experiment find δ_{CP} equal to $(-3.13, -0.39)$ for normal ordering and to $(-2.09, -0.74)$ for inverted ordering at 90% C.L. [84]. The CP conservation hypothesis ($\delta_{CP} = 0, \pi$) is excluded at 90% C.L.

The second missing piece in the whole scenario is the mass hierarchy. From the experimental point of view, in fact, only the modules of the squared mass differences are known with a satisfactory statistical significance, except for Δm^2_{21}, which is known to be positive and whose sign was determined using the different matter effects between neutrino and anti-neutrino [85].

Also the absolute scale of neutrino masses is not known, yet. Obtaining significant constraints on it would give important information about the detailed structure (hierarchical, quasi-degenerate, etc.) of the neutrino mass spectrum.

Another open question is the nature of neutrino masses: if they are Dirac or Majorana. This is of fundamental importance for understanding the origin of neutrino masses and mixing and of the symmetries governing the lepton sector of particle interactions. Progress in the theory of neutrino mixing might also lead to a better understanding of the mechanism of generation of baryon asymmetry of the Universe.

Chapter 2

The OPERA experiment

After the establishment of ν_μ disappearance in 1998 [1], the direct and unambiguous detection of its oscillation in a different neutrino flavour was still an important missing tile in the oscillation scenario: the ν_μ, in fact, could oscillate to ν_τ or to a new non-interacting "sterile" neutrino ν_x.

The OPERA experiment [86, 87] was designed to conclusively prove the existence of $\nu_\mu \rightarrow \nu_\tau$ oscillations in an almost pure ν_μ beam. Furthermore, even though the existence of ν_τ oscillations was accepted, it had never been observed.
The direct appearance search was based on the detection of τ leptons produced in ν_τ charged current interactions (CC). The detector was located at Gran Sasso Underground laboratory in Italy and used the high-intensity and high-energy CNGS (Cern Neutrino to Gran Sasso) beam. It was a *long-baseline* experiment, since the distance between the neutrino source and the detector was 730 km. OPERA took data from 2008 to 2012, for a total CNGS beam intensity of $1.8 \cdot 10^{20}$ protons on target (p.o.t.).

2.1 The CNGS beam

The CNGS beam was designed and optimized to study $\nu_\mu \rightarrow \nu_\tau$ oscillation in appearance mode [88]. For a nominal CNGS cycle there were two SPS extractions (10.5 μs each, separated by 50 ms) of $\sim 2.0 \cdot 10^{13}$ p.o.t per pulse. Each CNGS cycle in the SPS was 6 s long. The time information of the proton extraction was saved and used to select only events on-time with the CNGS beam, in order to reduce backgrounds.

The neutrino beam was generated by a 400 GeV/c proton beam extracted from the CERN SPS. The proton beam was transported through the transfer line TT41 to the target T40 [89]. The target was made of 13 graphite rods, each 2 m long, well encompassing the proton beam.

When the proton beam hit the target, secondary particles such as pions and kaons were produced. Positively charged particles were focused into decay pipe by two magnetic lenses, called horn and reflector. A 1000 m long decay pipe allowed them to decay into μ^+ and ν_μ in forward direction with an opening angle of about 2 mrad. A 18 m long dump placed at the end of the decay pipe, absorbed the remaining non-decayed hadrons. Two muon detector stations allowed the measurement of the beam profile and the beam intensity to monitor and tune the neutrino beam. At the end of the beam line, muons were absorbed within a short distance in the rock, while ν_μ continued their travel towards the LNGS underground laboratory.

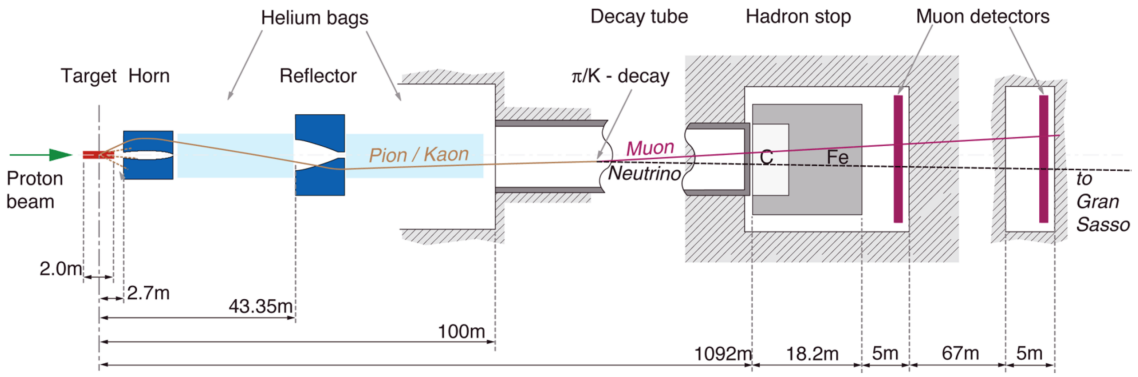

Figure 2.1. Main components of the CNGS beam line

The neutrino beam energy was set in order to maximize the oscillated ν_τ interactions, given the distance between the neutrino source and the detector: the average neutrino energy at LNGS was ∼17 GeV, while the the average L/E_ν ratio was 43 km GeV^{-1}. Expected flux of ν_μ at the LNGS site is shown in fig. 2.2, together with the ν_τ cross section (σ_{ν_τ}) multiplied by the oscillation probability, which is given by:

$$\mathcal{P}_{\nu_\mu \to \nu_\tau} = \sin^2 2\theta_{23} \cdot \sin^2 \left(\frac{1.27 \cdot \Delta m^2_{23} \cdot L}{4\ E} \right) \tag{2.1.1}$$

Properties of the CNGS neutrino beam at the LNGS site are summarized in table 2.1. The $\bar{\nu}_\mu$ contamination was ∼ 4% (2% as interaction rate, given the ν_μ cross section), the ν_e and $\bar{\nu}_e$ contamination lower than 1%, while the number of prompt ν_τ from D_s production and decay was negligible. More detailed information about the CNGS beam can be found in [89, 90].

The integrated p.o.t. in all OPERA runs are reported in table 2.2.

The low contamination of ν_e and $\bar{\nu}_e$ allowed to search also for $\nu_\mu \to \nu_e$ oscillation, looking for an excess of ν_e CC interactions, although the experiment L/E is not

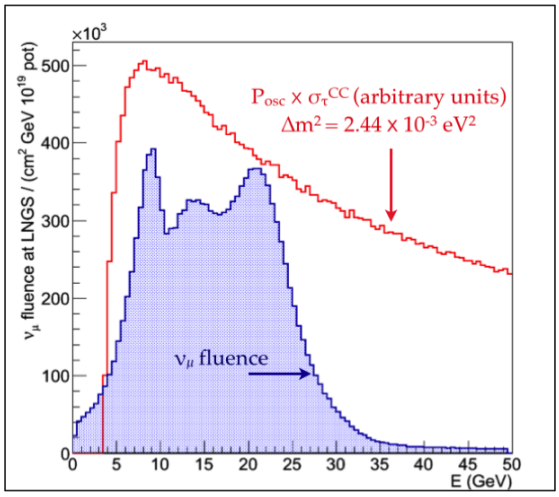

Figure 2.2. $\sigma_{\nu_\tau CC} \times \mathcal{P}_{\nu_\mu \to \nu_\tau}$ for $\Delta m^2 = 2.44 \cdot 10^{-3}$ eV^2 and $\sin^2 2\theta - 23 = 1$, compared to ν_μ flux

$\nu_\mu(m^{-2}p.o.t)$	$7.45 \cdot 10^{-9}$
ν_τ CC $events/p.o.t/kton$	$5.44 \cdot 10^{-17}$
$\langle E \rangle_{\nu_\mu}$	$17GeV$
ν_e/ν_μ	0.8%
$\bar{\nu}_\mu/\nu_\mu$	2.0%
$\bar{\nu}_e/\nu_\mu$	0.05%

Table 2.1. CNGS neutrino beam properties at LNGS [91]

Run	**Beam days**	**p.o.t**$\cdot 10^{19}$
2008	123	1.74
2009	155	3.53
2010	187	4.09
2011	243	4.75
2012	257	3.86
Total	**965**	**17.97**

Table 2.2. Integrated protons on target in the OPERA runs, from 2008 to 2012

optimised for that. In this case, the systematic error related to the ν_e contamination plays an important role. This uncertainty depends on the knowledge of the kaons produced: a 5% systematic uncertainty is assumed on the overall ν_e flux [92].

2.2 The OPERA detector

The OPERA detector (10 m×10 m×20 m) was located in the Hall C of the Gran Sasso underground laboratory [90]. A picture can be seen in fig. 2.3.

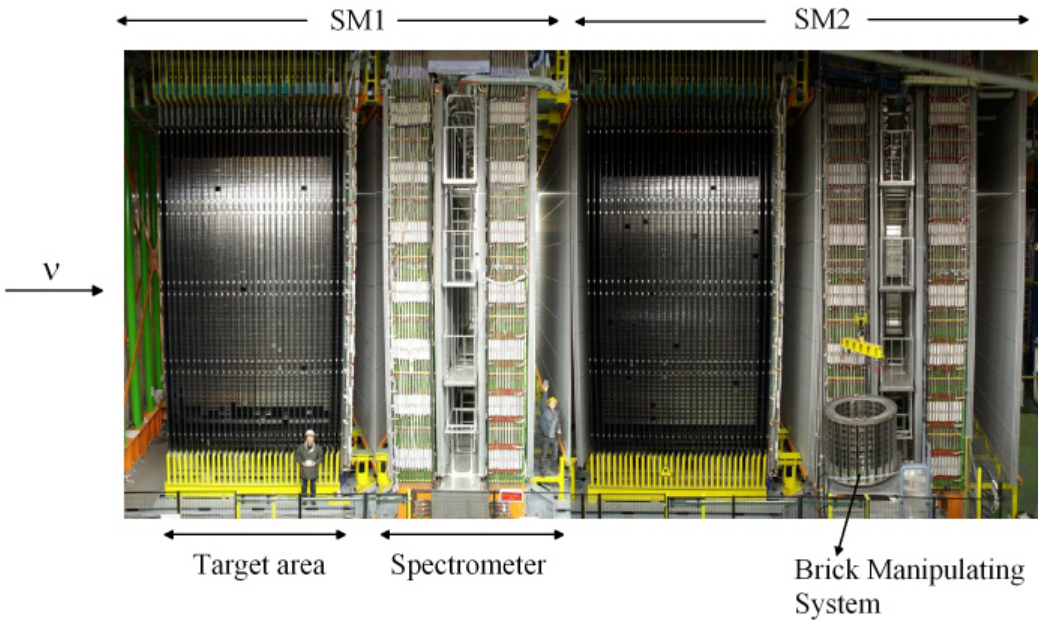

Figure 2.3. OPERA detector

The OPERA reference frame has the z axis parallel to the longest dimension of the detector, oriented along the beam direction; the y axis is the vertical axis, pointing to the vault of the gallery; the x axis is parallel to the floor.

The detector was an hybrid apparatus consisting of an emulsion/lead target complemented by electronic detectors. To compensate the short lifetime and the small interaction cross-section of the τ lepton, nuclear emulsion films, having high spatial resolution, were combined with lead to form the target and the main detector. Thanks to nuclear emulsions it was possible to study in detail interaction and decay topologies. The electronic detectors, on the other hand, provided time resolution to the emulsions, preselected the interaction region, identified muons and measured their charge and momentum.

OPERA detector was made up of two identical super-modules (SM) aligned along the CNGS beam direction, each made of a target section and a muon spectrometer. In front of the first SM there was a veto plane made of two planes of resistive plate chambers (RPC).

Each super-module was composed of a target section followed by a muon spectrom-

eter. The target consisted of a multi-layer array of 31 target walls interleaved with 31 Target Trackers (TT), made of a double layered plane of long scintillator strips. A target wall was an assembly of horizontal trays each loaded with Emulsion Cloud Chamber target units, called *bricks*. In the whole apparatus there were more than 150000 bricks, each consisting of 57 emulsion films, 300 μm thick, interleaved with 56 lead plates, 1 mm thick, for a total mass of 8.3 kg. The muon spectrometer was composed of a magnet equipped with resistive plate chambers and drift tubes. Interface emulsion detectors, called Changeable Sheets, were attached to the downstream face of each brick.

2.2.1 The OPERA emulsion film

Nuclear emulsions are a particular type of photographic emulsions used for elementary particle study. Techniques for their production and application have been developed in the first half of 1900. Their micrometric spatial resolution made them one of the first particle detector, largely employed in the High Energy Physics field.

The OPERA emulsion film has a pair of 44 μm emulsion layers coated on both sides of a 205 μm transparent cellulose tri-acetate base plastic base, for a total thickness of (293 ± 5) μm [93]. The emulsion layer consists of silver bromide (AgBr) crystals dispersed in a gelatin binder. The size of the grains is about 0.2 μm. A picture of the cross-sectional view of the OPERA emulsion film, its crystal structure and a particle trace on it are shown in fig. 2.4.

When a charged particle passes through the emulsion medium, the energy released frees silver atoms creating metallic silver on the surface of a bromide crystal, called latent image, not visible yet, made of a few silver atoms on crystals, each of them made of billions of atoms.

Photographic developer is a chemical amplifier acting on the latent image, with a gain factor up to several billion. Under chemical development procedure, indeed, silver atoms with diameter of about 0.6 μm are created, visible as "grains" with an optical microscope. The intrinsic position resolution of the gelatin treated with the normal OPERA developer is about 50 nm, which corresponds to a 0.25 mrad intrinsic angular resolution. The density of the emulsion gel is 2.7 g/cm^3 and its radiation length X_0 is 5.0 cm. The sensitivity of OPERA emulsion films is measured to be about (36 ± 1.1) grains/(100 μm) for Minimum Ionizing Particles (MIPs) [94].

No experiments before OPERA needed such a large amount of nuclear emulsions (more than 110000 m^2). Of course, it was impossible to produce such an amount of films with the previous manual pouring techniques, therefore a dedicated industrial production and an R&D program was set up in collaboration with the Fuji Film Company.

Emulsion films are sensitive to charged particles until they are chemically devel-

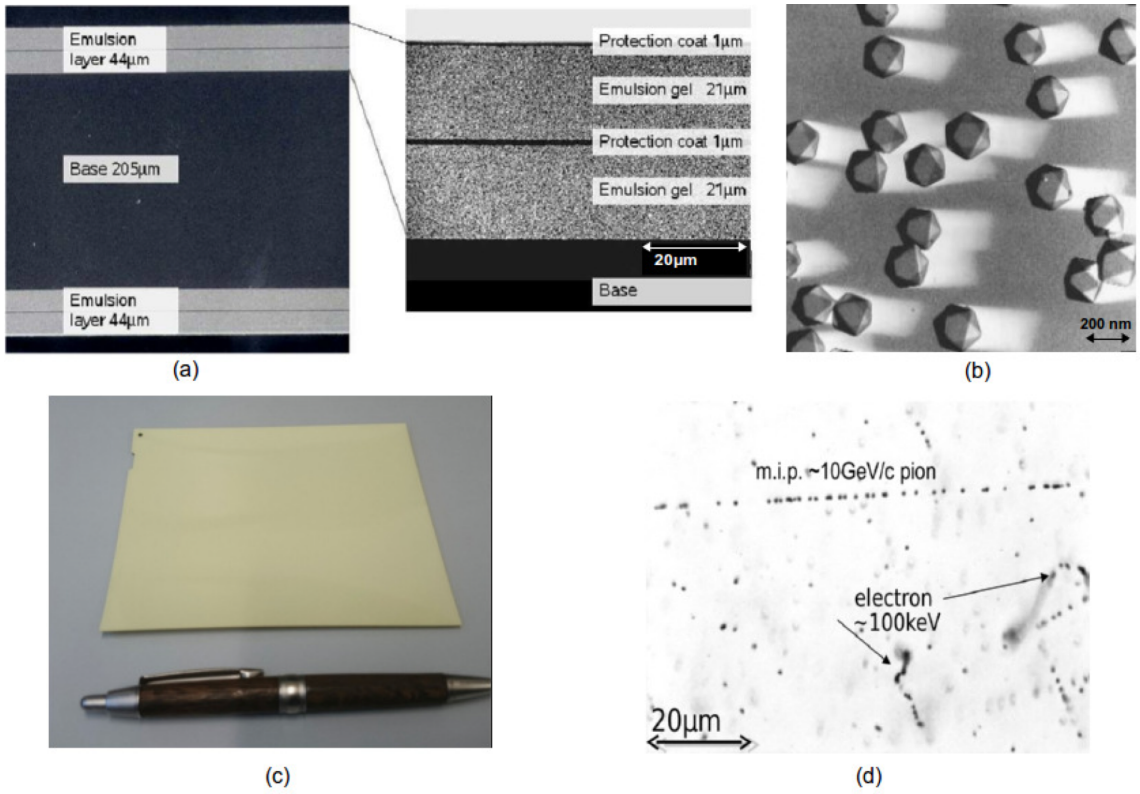

Figure 2.4. (a) Electron microscope view of the emulsion with 44 μm emulsion layer coated on both sides of a 205 μm plastic base; (b) crystals of the emulsion; (c) OPERA emulsion film; (d) examples of signal tracks (MIP) and Compton electrons formation in nuclear emulsions

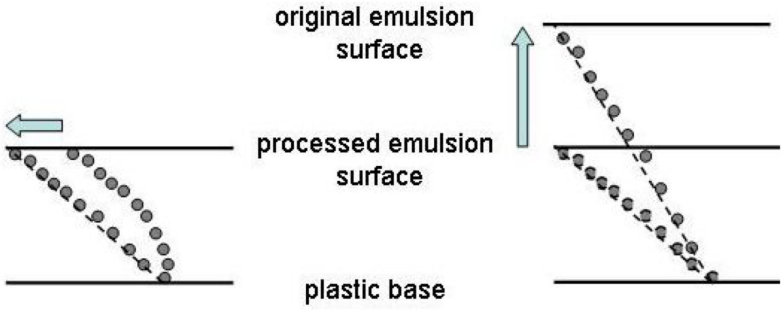

Figure 2.5. Track distortion (left); Shrinkage (right)

oped. Therefore, on top of the tracks associated to neutrino interactions, during their lifetime they integrate all particle tracks from cosmic rays and environmental radioactivity. During the production process at the Fuji Film industrial plant in Japan, each film integrated about 3000 tracks/cm^2. In order to reduce this uncorrelated background, a new procedure called *refreshing* was set up, based on the fading of latent image under high humidity ($\sim$ 98% RH) and defined temperature (28°C) conditions. To process the about 10 millions films needed for the experiment, a refresh facility was constructed in Tono mine in Gifu (Japan), and all OPERA films were refreshed before they were shipped to LNGS. This process reduces the integrated number of tracks from about 3000 to less than 100 tracks/cm^2, without affecting the emulsion sensitivity to tracks detected later on. In addition, the Changeable Sheets emulsion films were refreshed again in the Gran Sasso underground refreshing facility.

Fog, distortion and shrinkage effects

Thermal excitation induces randomly distributed grains called "*fog*", which constitute a background for track reconstruction. The fog density was slightly increased by refreshing: measurements showed a fog density of 3 and 6 grains per 1000 μm^3 of emulsion before and after the refreshing, respectively. Example of fog compared to MIP in emulsion can be seen in fig. 2.4 (d).

After being treated in Tono mine, emulsions were transported to Italy by ship, the films placed vertically to minimize the cosmic ray flux, integrating about 1000 tracks/cm^2. Unlike the films in the bricks exposed to the neutrino beam, during the transportation, the films were not interleaved with lead plates, in such a way that the tracks accumulated had a different alignment and could be discarded at the analysis level. Other two effects had to be taken into account: distortions and shrinkage (see fig.2.5).

The distortion shifts the position of the recorded trajectories stresses accumulated

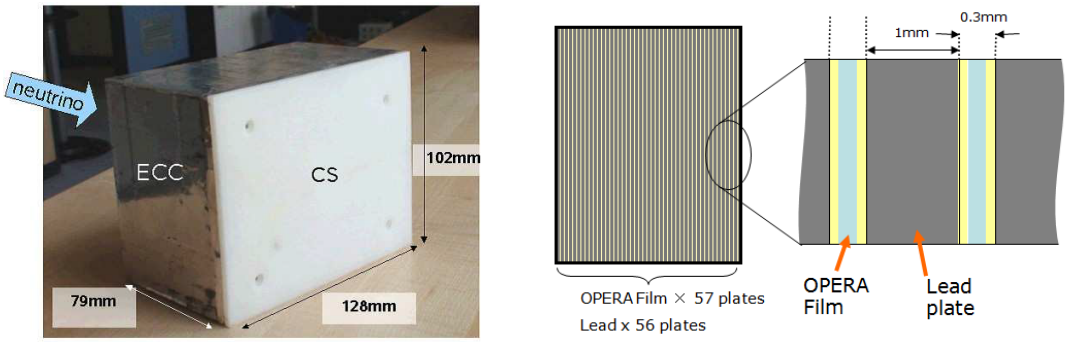

(a) (b)

Figure 2.6. Photo (a) and schematic drawing (b) of an Emulsion Cloud Chamber (ECC)

in the gelatin layer. Tracks changed their direction by an amount which depends on the magnitude and direction of the shear.

The Shrinkage is a reduction of the emulsion thickness after the development process. The shrinkage factor is defined as the ratio between the thickness of the emulsion before and after the development: measured track slopes must be multiplied by this factor to obtain the real value.

2.2.2 OPERA ECC Brick

The Emulsion Cloud Chamber (ECC) brick, shown in fig. 2.6, was the fundamental element of the OPERA detector. Every brick consists of 57 emulsion films interleaved by 56 lead plates, 1 mm thick, packed together in a box 10.2 cm×12.7 cm×7.5 cm, for a total weight of 8.3 kg [95, 96].

The thickness of the brick corresponds to 10 radiation lengths X_0 along the beam direction. Lead plates act as high density material to compensate the low neutrino cross section, while emulsion plates provide micrometric position resolution and 3D particle tracking. The brick size is designed by different requirements; its thickness allows to measure the momentum of hadrons through the multiple Coulomb scattering method [97] and also to identify electrons and reconstruct their electromagnetic (EM) showers.

A total number of 150036 bricks was assembled by a dedicated Brick Assembly Machine composed by anthropomorphic robots, ensuring a high precision in the piling up.

An automated system called Brick Manipulator System (BMS) took care of the target filling and extraction. Two BMS robots were placed on each side of the detector and could load and unload bricks using a small vehicle equipped with a suction grip.

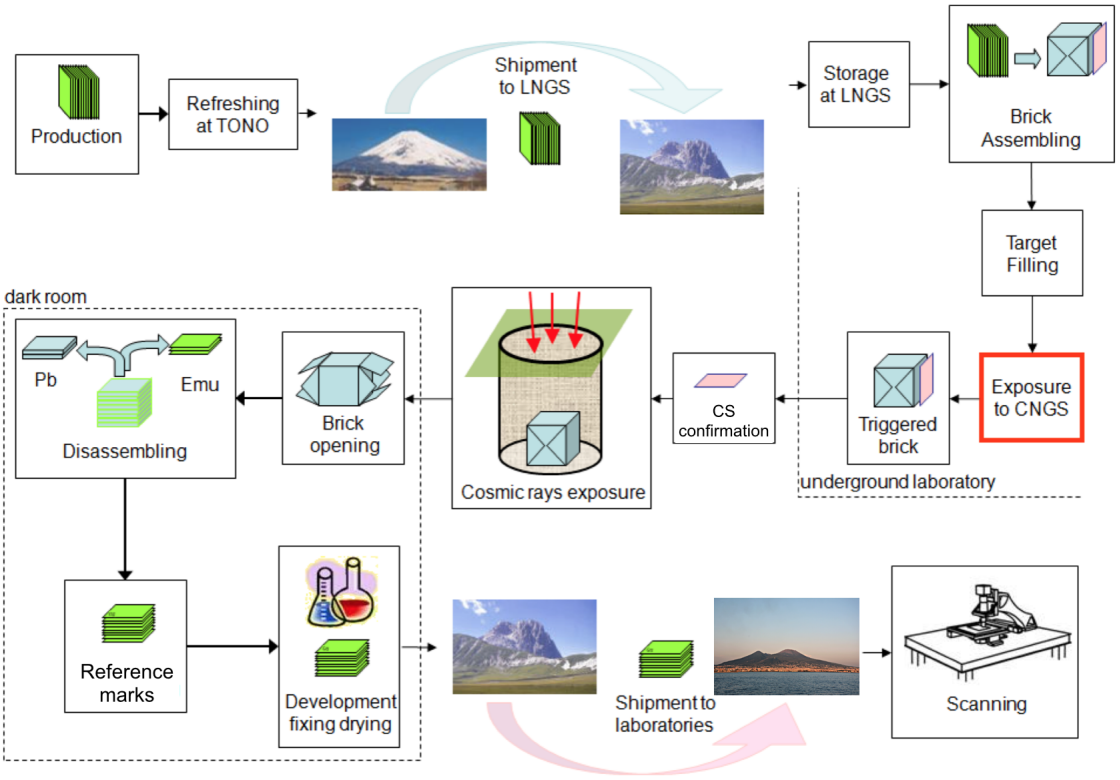

Figure 2.7. Flow of the emulsion brick: from the production to the analysis.

Changeable Sheet Doublet

Changeable Sheet Doublet (CSD) was a sub-detector placed downstream of each brick [98]. It was made of two emulsion films, packed in an envelope placed inside a plastic cover, to be removed without opening the brick. It worked first of all as an interface between the brick and the closest downstream TT plane, in order to confirm that the brick predicted by the electronic detector actually contained the neutrino interaction vertex. Moreover, the CSD made possible to go from TT resolution, of the centimetre order, to the micrometre spatial resolution of nuclear emulsions inside the brick. Lastly, CSD provided predictions about the area to be scanned, strongly reducing the ECC scanning load. The use of the CSD also increased the brick finding efficiency by reducing ambiguities related to the back-scattered tracks and saved the detector target mass.

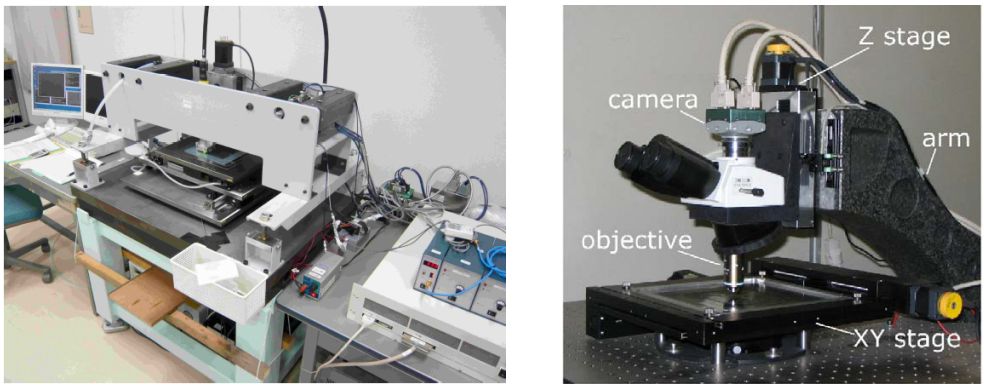

(a) (b)

Figure 2.8. Example of the (a) S-UTS, the Japanese Scanning System, and (b) the ESS, the European Scanning System

The European Scanning System

In the OPERA scanning laboratories the emulsion measurements are performed by an automatic scanning system. Two different approaches were followed by Japanese and European groups.

The Japanese Scanning System is called S-UTS [99] and has a scanning speed of 72 cm^2/h, achieved in 2010. The European Scanning System (ESS) [100, 101] was developed by a joint effort of several European laboratories and the first prototype was assembled in Naples in 2004. Example of a S-UTS and an ESS can be found in fig. 2.8.

The ESS consists of a CMOS camera, a frame-grabber, an on-board image processor, a movable stage, an optical system, an illumination system, a motion control unit and a workstation to perform on-line and off-line processes. With this configuration, it has a scanning speed of 20 cm^2/h. The scanning output is a collection of raw data files which are saved into a database.

During the scanning, the emulsion is placed on a glass plate equipped with a vacuum system. Moving the focal plane of the objective through the emulsion thickness, a sequence of 16 tomographic images of each field of view is obtained [102], where the images are taken at equally spaced depth levels. The acquired images are then converted into a grey scale of 256 levels, sent to a vision processor board, hosted in the control workstation, and analysed to search for sequences of aligned grains.
Grains produced by the particle, indeed, are recognized as a cluster of pixels and form the so called *micro-track* (MT) in one emulsion layer. Micro-tracks on the top and bottom emulsion layers are then connected across the plastic base to form a *base-*

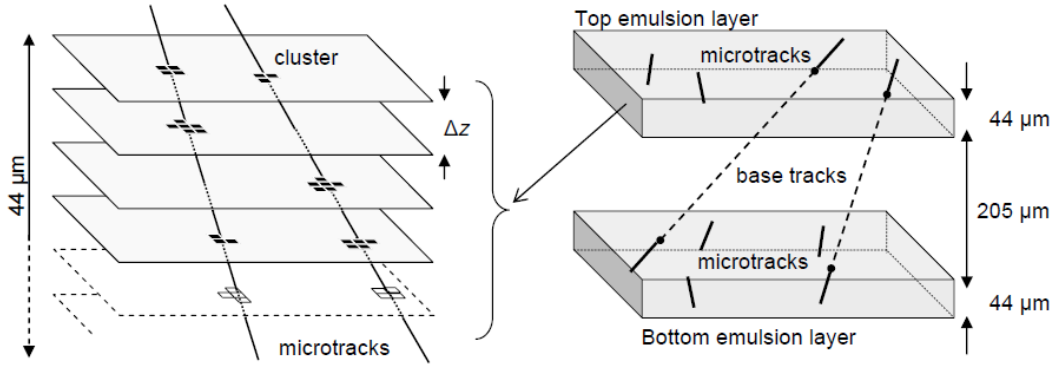

Figure 2.9. Schematic visualization of the image grabbing and "micro-track" reconstruction by combining clusters at different levels

track (BT). A sequence of base-tracks from different emulsion plates reconstructs the particle track inside the ECC (fig. 2.9). Base-tracks and micro-tracks are measured within an angular acceptance of $\tan\theta < 0.6$, where θ is the angle between the track and the direction orthogonal to the plate. Track position and slope is determined by a linear fit.

2.2.3 Target Tracker

The electronic detector placed downstream of each brick wall was called Target Tracker (TT) [103]. The TT recorded all the charged particles passing through, providing real-time detection of the outgoing charged particles and therefore the time stamp of neutrino interactions. TT primary goal was the localization of the brick in which the neutrino interaction took place and to guide the scanning of the CSD by defining the region to be scanned. They also provided a rough calorimetric measurement of the hadronic shower energy.
A TT wall, shown in fig. 2.10, consisted of two scintillator planes, which provided vertical and horizontal coordinates. Each plane consisted of 256 plastic scintillator strips 6.86 m×2.63 cm×1.06 cm. Along the strip, a 1 mm diameter Wavelength Shifting fiber (WLS) was read on both sides by a multi-anode photomultiplier (PMT), giving a position resolution of $\sim$ 1 cm (fig. 2.11). The strips were grouped in four modules, each module read out by a 64-channel Hamamatsu PMT; 16 PMTs per TT wall were used. Signals were measured at each end of the scintillator strips in terms of ADC counts and then converted into energy deposit [104]. Fig. 2.12 shows the reconstructed energy in the TT for events where a muon track was reconstructed in the electronic detectors.

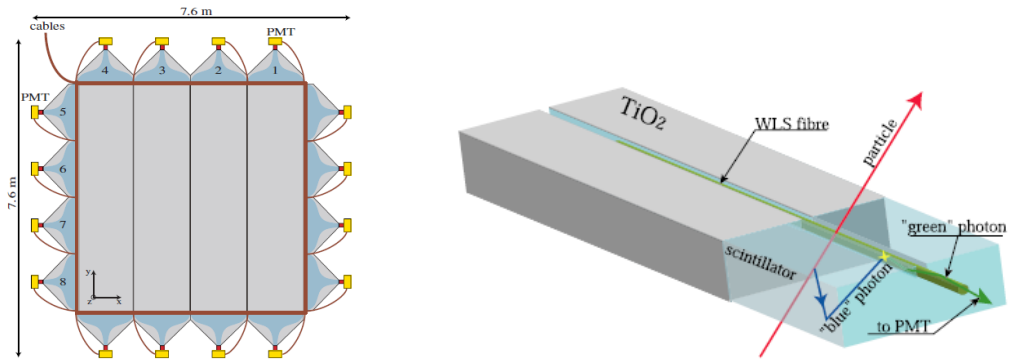

(a) a (b)

Figure 2.10. Schematic view of (a) the two scintillator planes of a TT wall and (b) a scintillator strip with the wave length shifting fibers on the right

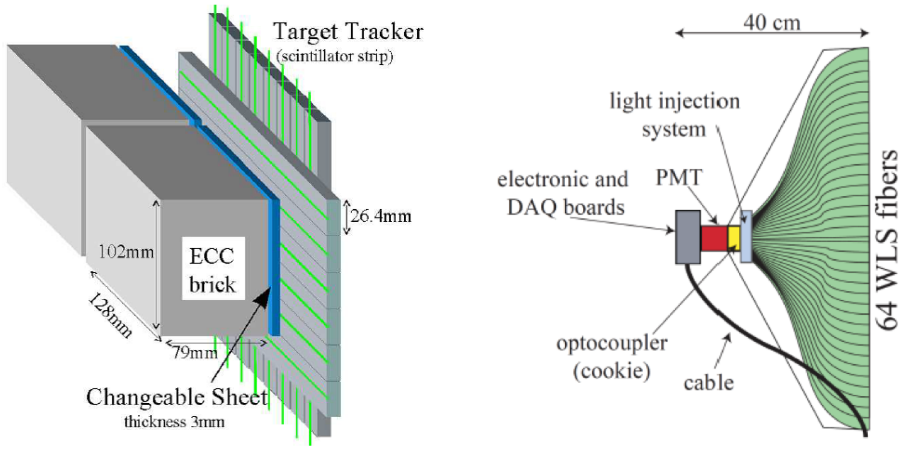

(a) (b)

Figure 2.11. Schematic view of (a) a scintillator strip with the WLS fiber and (b) a strip module end-cap with the front-end electronics and DAQ board

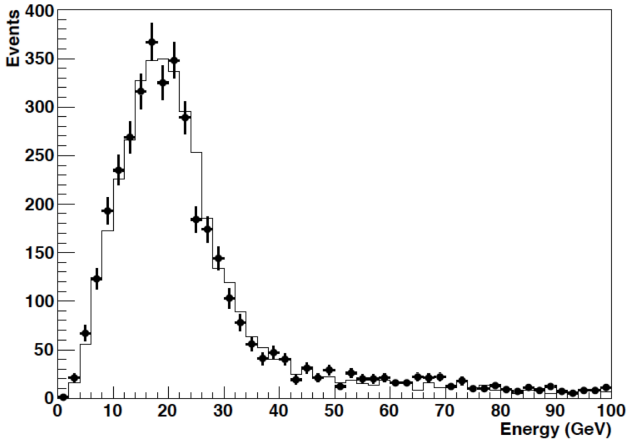

Figure 2.12. Energy deposit in the TT for events with at least one reconstructed muon. Dots with error bars correspond to data and solid lines to MC

2.2.4 Muon Spectrometer

A muon spectrometer [90] was placed downstream of each target section to identify muons and measure their momentum and charge. Each spectrometer consisted of a dipole magnet made of two iron walls interleaved with RPCs, HPTs (High Precision drift tubes) and two XPCs (RPCs with readout strips inclined by $\pm 42.6°$ with respect to the horizontal) [105, 106, 107].
RPCs' and XPCs' provided a trigger signal for HPTs.
The transverse size of the magnets was 8.75 m and 8 m in the horizontal and vertical directions respectively: this provided an adequate geometrical acceptance also for muons originating in the upstream target volume. Each arm was made of 12 iron plates, 5 cm thick, interleaved with 2 cm gaps, filled with 11 planes of RPCs whose size was 8.7 m $\times$ 7.9 m, transverse to the beam direction. The iron was magnetized by a current of about 1200 A circulating in the top and bottom copper coils. The measured magnetic field strength was about 1.52 T. The vertical field lines had opposite directions in the two magnet walls.

RPCs (fig. 2.13) were made up of electrode plates where each electrode plate consisted of a 2 mm thick high resistivity plastic laminate, painted with graphite.

On each side of the RPC planes, the induced pulses were collected by 3 cm wide readout copper strips in the horizontal direction and by 2.6 cm wide ones in the vertical direction. These detectors provided a coarse tracking inside the magnet, allowing muon identification. The scheme of the magnets can be seen in fig. 2.14.

To precisely measure the bending of the muon, six drift tubes with 0.5 mm resolution are interleaved between the two arms, as shown in fig. 2.15, constituting the

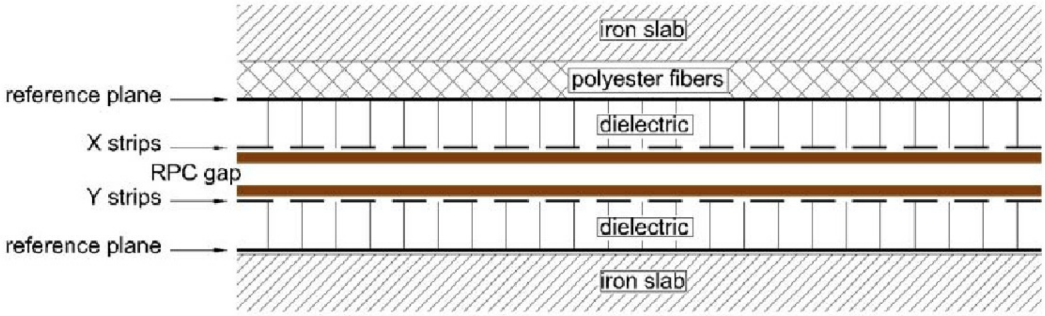

Figure 2.13. Section of a magnet gap with RPC and pick-up strips

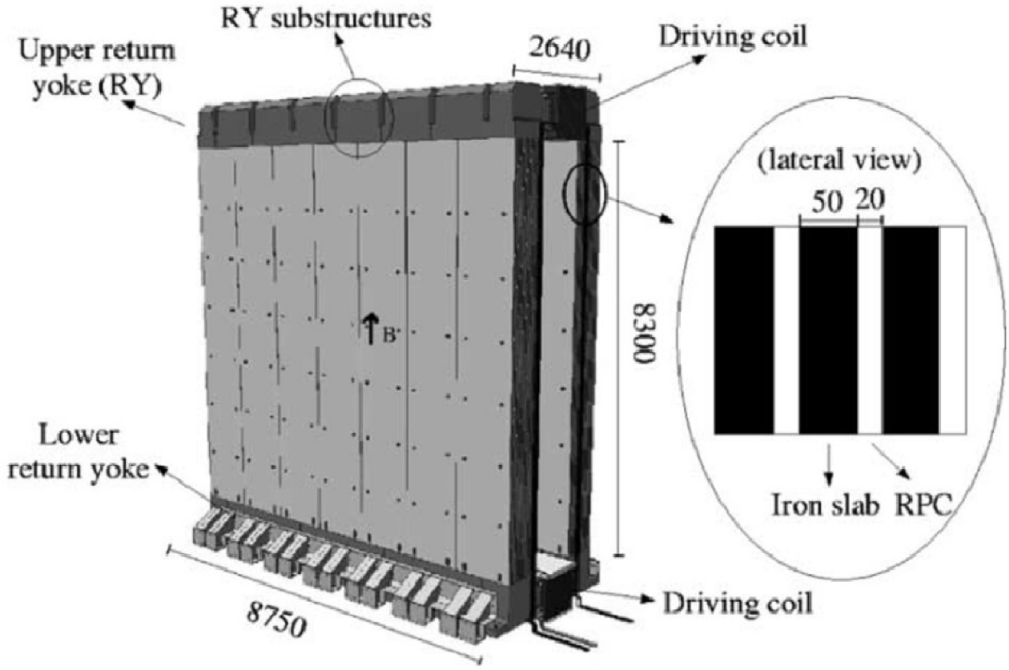

Figure 2.14. Details of the OPERA magnets. Quotes are expressed in mm

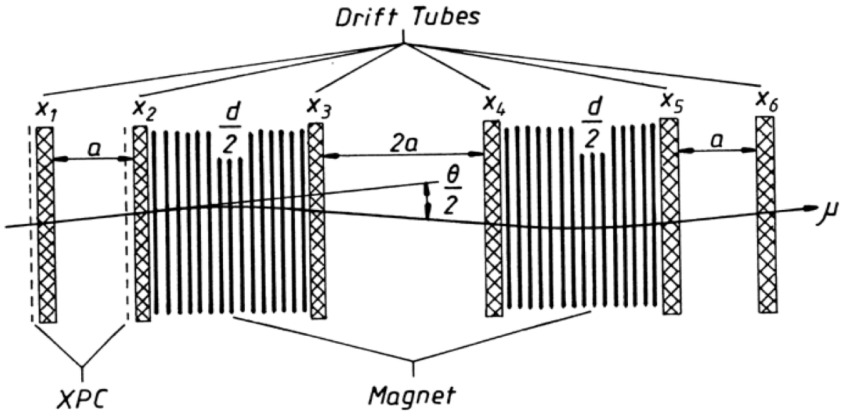

Figure 2.15. Drift plane arrangement in the muon spectrometer. Two planes of RPCs with inclined strips (XPCs) are also shown

HPTs. Two of them were located upstream of the first magnet wall, two between the magnet walls and two downstream of the magnet walls.

The XPCs are an additional pair of inclined RPCs located directly in front of the magnet to improve the measurement of the angular resolution and resolve the ambiguities.

2.2.5 Veto System

The CNGS beam may have interacted in the rock, in the mechanical structures or in Borexino detector, before reaching the OPERA detector. Secondary particles produced in this kind of events could enter the detector and generate false triggers for brick extractions. In order to reject these events, a VETO system was located in front of the OPERA detector in order to reject this kind of events.
The VETO consisted of two glass RPC planes (9.6×9.2) m^2, each one with 32 units. Each plane was equipped with horizontal and vertical copper strips with a pitch of 2.5 cm [108].

2.3 ν_τ search in the OPERA experiment

2.3.1 Signal

The observation of the $\nu_\mu \to \nu_\tau$ appearance was the main goal of the OPERA experiment. The signal of the oscillation occurrence was the charged current interaction of ν_τ in the detector target ($\nu_\tau N \to \tau^- X$), where X stands for hadrons. The interaction was identified by the detection of the τ lepton or its decay products. Given the short

lifetime of the τ lepton ($c\tau = 87$ μm), only the unique tracking capability of nuclear emulsions allows to observe the τ decay, with a signature given by a "kink" topology or an additional downstream vertex. The τ decay channels investigated by OPERA were the electronic, muonic and hadronic decay channels, as reported in table 2.3. The hadronic channel can be divided further in 1-prong and 3-prong.

Channel	**Branching Ratio**
$\tau^- \to h^- \nu_\tau (n\pi^0)$	49.5%
$\tau^- \to e^- \nu_\tau \bar{\nu}_e$	17.8%
$\tau^- \to \mu^- \nu_\tau \bar{\nu}_\mu$	17.7%
$\tau^- \to h^- h^- h^+ \nu_\tau (n\pi^0)$	15.0%

Table 2.3. τ decay modes and the corresponding branching ratios [109]

The τ decays occurring inside the ECC were classified as short or long decays:

- short-decays are events where the neutrino interaction took place in the same lead plate of the τ decay;
- long-decays refer to events where τ decays occurred in the first or second lead plate downstream of the neutrino interaction.

This means that in the long decays a parent particle is observed, while in the short decays is not. τ candidates were first selected on the basis of the detection of a reasonably large kink angle between the τ and its daughter tracks and on the impact parameter (IP) of the τ daughter track with respect to the interaction vertex. Therefore, it was not possible to identify a short decay for quasi-elastic (QE) interactions, where the τ is the only charged particle detected at the primary vertex.

In the OPERA analysis, only long decays were considered for $\tau \to 1h$ and $\tau \to \mu$, due to the less sensitivity and high background for the short decays, while for $\tau \to 3h$ and $\tau \to e$ channels both short and long decays have been taken into account.

2.3.2 Background sources

Background for the ν_τ search came from the processes that mimic the τ decay topologies. These are listed in the following, ordered according to the decreasing importance:

- **Decay of charmed particles**

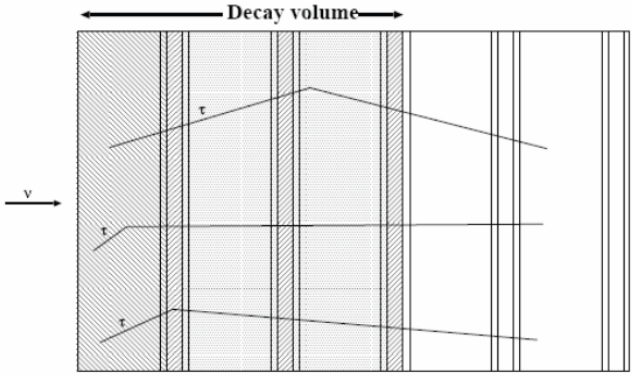

Figure 2.16. Different decay topologies: short decay (left-hatched region); long decay in base (right-hatched region) and long decay outside the base (shaded region).

Charmed hadron production (D^0, D^+, D_s^+ and Λ_c^+) was the main background for the ν_τ search, since their flight length is similar to the τ one, as shown in table 2.4. Charm particles are produced in the $\nu_\mu CC$ interactions: $\nu_\mu N \to \mu^- cX$. Charm hadrons can decay in semileptonic or hadronic ways: $c \to \mu^+(e^+)\nu_\mu(\nu_e)X$. These processes constituted background for the $\tau \to 1h$ and $\tau \to 3h$ if the μ^- at primary vertex was not identified and for $\tau \to \mu$ and $\tau \to e$ if also the charge of the secondary $\mu^+(e^+)$ was misidentified or not identified (see fig. 2.17 (a)).

Particle	**Quark Component**	**Mass (MeV)**	$c\tau(\mu$**m**$)$	**hadronization fractions (%)**
D^0	$c\bar{u}$	1865 ± 0.5	122.9	43.8 ± 3.0
D^+	$c\bar{d}$	1869 ± 0.5	311.8	21.7 ± 3.4
D_s^+	$c\bar{s}$	1969 ± 0.6	149.9	9.2 ± 3.8
Λ_c^+	udc	2285 ± 0.6	59.9	25.3 ± 4.9

Table 2.4. Quark contents, masses, lifetimes and production hadronization fractions for charm particles at 17 GeV OPERA average beam energy.

- **Hadronic re-interactions**
  A source of background for $\tau \to 1h$ and $\tau \to 3h$ decay channels was given by the re-interactions in lead of hadrons produced in ν_μNC and ν_μCC events, where the primary muon was not identified. A schematic representation is shown in fig. 2.17 (c) and (d). Evaluation of the hadron re-interaction background was performed with a FLUKA based simulation and test beam exposures. OPERA bricks exposed to 2, 4 and 10 GeV/c π beams and data-driven checks on FLUKA

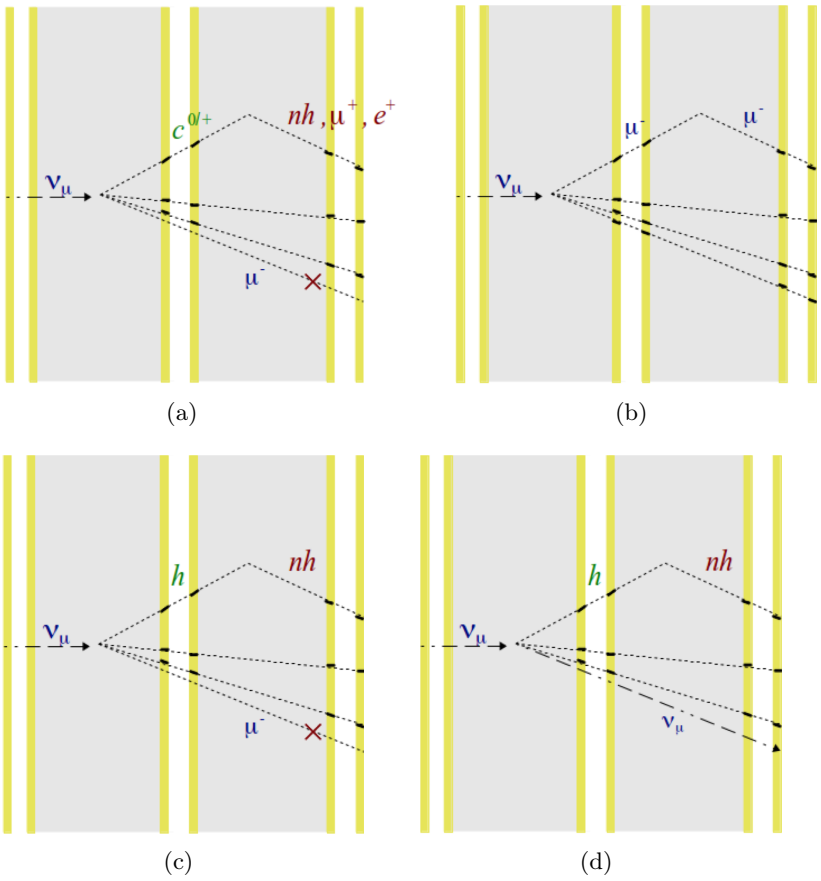

Figure 2.17. Schematic drawing of the background sources in the OPERA experiment: (a) Decay of a charm particle where the primary muon is not identified; (b) large angle μ scattering, background source for muonic τ decays; (c) re-interaction of a primary hadron in a ν_μCC process where the primary muon is not identified; (d) re-interaction of a primary hadron in a ν_μNC process

description of hadronic interactions were performed [110]. Good agreement between the data and the simulation was observed.

- **Large angle muon scattering**
  Muons produced in ν_μCC interactions may be scattered in the lead plate downstream of the vertex plate and, if the scattering angle was larger than the selection cut, could mimic a τ decaying into a muon. Evaluation of the expected background for the $\tau \to \mu$ decay channel was performed with FLUKA and GEANT4 based simulations. See fig. 2.17 (b) for the schematic drawing of the process.

- **Prompt ν_τ from CNGS target**
  The CNGS beam had a small contamination of D_s mesons, a fraction of which decayed into τ, producing a ν_τ. The expected contribution from this background source, taking into account the cross section, the branching ratio, the features of the beam and the distance of the detector to the source, is of the order of $\mathcal{O}10^{-7}$ ν_τCC interactions per ν_μCC event and therefore is considered totally negligible, given a number of located interactions of the order of $\mathcal{O}10^4$.

2.4 OPERA results

A sample corresponding to 1.8×10^{20} protons on target (p.o.t.) has been collected from 2008 to 2012 and resulted in 19505 neutrino interactions in the target fiducial volume. In the first phase of the OPERA experiment, it was decided to apply severe kinematical cuts in order to improve the purity of the ν_τ signal, getting a Signal to Noise ratio of about 10.

Over about 7000 located events, five ν_τ candidates, surviving these kinematical cuts, were found [111, 112, 113, 114, 2], with 0.25 background expected events, allowing to exclude the absence of $\nu_\mu \to \nu_\tau$ oscillations with a significance of 5.1σ [2]. The five ν_τ candidates will be described in Chapter 3, with particular emphasis to the last one, for which I personally contributed to the analysis.

Now, a new phase of the OPERA experiment is on-going: in order to estimate oscillation parameters with reduced statistical uncertainty, I have developed an analysis using looser selection cuts and multivariate techniques, which will be described in Chapters 4 and 5.

Chapter 3

Analysis status of the OPERA experiment

The aim of the experiment is to search for ν_τ candidates in order to confirm the $\nu_\mu \to \nu_\tau$ oscillation. Nevertheless, OPERA is able to identify all 3 neutrino flavours, so also the search for $\nu_\mu \to \nu_e$ oscillation and ν_μ disappearance are carried out. Moreover, the complete OPERA data set is being used to study very high energy atmospheric muons.

3.1 ν_τ candidates search

Since the beginning of the OPERA experiment, different strategies have been applied for the ν_τ search.

In the first two years of run (2008-2009) a conservative approach was chosen in order to get confidence on the detector performances, so all neutrino interactions occurring in the detector were analysed. On a sample of 505 0μ and 2268 1μ events, fully analysed up to the decay search, one 0μ event passed all the kinematical cuts and was declared a ν_τ candidate in the $\tau \to 1h$ decay channel.

From the 2010 run, since a good agreement between data and Monte Carlo simulation was confirmed [104], for 1μ events the kinematical cut $p_\mu < 15$ GeV/c was applied on the muon momentum, in such a way that events with $p_\mu \geq 15$ GeV/c were discarded. Furthermore, to speed up the analysis, priority was given to 0μ events and the most probable brick was analysed at first for each event. The analysis of second probable bricks was postponed since it increased efficiency by less than 50%, but doubled the analysis time. With this strategy, 486 0μ events and 818 1μ events went through all the analysis steps, up to the decay search. One 0μ event, showing a trident topology, survived all the selections and became a $\tau \to 3h$ candidate.

After Summer 2012, two additional candidates were found, in the $\tau \to \mu$ and $\tau \to 1h$ decay channels, respectively. A fifth ν_τ candidate was found in 2012 run and analysed in 2015. Since I personally contributed to its analysis, it will be described in-depth in paragraph 3.1.3.

A summary of the collected data samples and the contained events is given in table 3.1, where the number of detected ν_τ candidates for each run year is also reported.

	2008	2009	2010	2011	2012	Total
0μ events	149	253	268	270	204	1144
1μ events ($p_\mu < 15$ GeV/c)	543	1020	968	966	768	4264
Total events	691	1273	1236	1236	972	5408
Detected ν_τ candidates	-	1	-	1	3	5

Table 3.1. Summary of the collected data sample and the detected ν_τ candidates for each run year

3.1.1 Expected signal and background

The requirements to select ν_τ candidates are not merely topological. If an interesting topology is detected, kinematic cuts are applied in order to discriminate between signal and background. Moreover, additional procedures such as *Track Follow Down* and the search for large angle tracks are carried out for the events passing the selection criteria.

Selection criteria consist of strong kinematic constraints depending on the decay channel, as reported in table 3.2, which were defined at the very beginning of the experiment. This selection maximizes the signal to noise ratio to about 10.

The variables used are listed below.

- **Decay z** (z_{dec}) is the z-coordinate of the decay vertex with respect to the downstream face of the lead plate containing the primary vertex ($z_{dec} < 44$ μm for short decays).
- **Transverse momentum at secondary vertex** (p^T_{2ry}) is the transverse component of daughter momentum with respect to the parent direction, for 1-prong decays.
- **Missing transverse momentum** (p^T_{miss}) is the module of the vectorial sum of the transverse momenta of primaries (except the parent) and daughters with respect to the neutrino beam direction.

Variable	$\tau \to 1h$	$\tau \to 3h$	$\tau \to \mu$	$\tau \to e$
z_{dec} (μm)	$[44, 2600]$	<2600	$[44, 2600]$	<2600
p^T_{miss} (GeV/c)	$< 1\star$	$< 1\star$	/	/
ϕ_{lH} (rad)	$>\pi/2\star$	$>\pi/2\star$	/	/
p^T_{2ry} (GeV/c)	$>0.6\,(0.3)$*	/	>0.25	>0.1
p_{2ry} (GeV/c)	>2	>3	$[1, 15]$	$[1, 15]$
θ_{kink} (rad)	>0.02	<0.5	>0.02	>0.02
m, m_{min} (GeV/c^2)	/	$[0.5, 2]$	/	/

Table 3.2. Kinematic selection. The variables are defined in the text. * The cut on p^T_{2ry} for the 1-prong hadronic decay is set at 0.3 GeV/c in the presence of γ particles associated to the decay vertex and to 0.6 GeV/c otherwise. Cuts marked with $\star$ are not applied for QE event. Only long decays are considered for the $\tau \to \mu$ and $\tau \to h$ channels due to a large background component in short decays from charmed particles and hadronic re-interactions respectively

- **Momentum at secondary vertex** (p_{2ry}) is the total momentum of the visible tracks coming out from the secondary vertex.
- **Kink angle** (θ_{kink}) is the average 3D angle between the parent and its daughters.
- **Invariant mass** (m) of the daughters is calculated assuming the π mass for all daughters and it is used only for the 3-prong decay channel.
- **Minimum invariant mass** (m_{min}) takes into account that a neutrino may be produced in the decay [115].
- **Lepton-hadron transverse angle** (ϕ_{lH}) is one of the variables that better discriminate signal and background, so it will be described in detail.
  It is the angle in the transverse plane between the parent track and the hadron shower direction. If the primary multiplicity (including the τ track candidate) is larger than two, the track with the largest difference in ϕ_{lH} with respect to the τ candidate is removed, unless it is identified as a hadron with high probability by the track follow-down procedure, which will be described in the next paragraph. This is intended to reject the background due to a genuine muon not tagged as a muon by the electronic detectors. For these events, indeed, if the track with the largest ϕ_{lH} difference is not excluded, the angle would be large and thus the kinematic cut on this variable would not be effective. As an example, ϕ_{lH} distributions for signal and background for single hadron and three hadrons decay channel are reported in fig. 3.1.

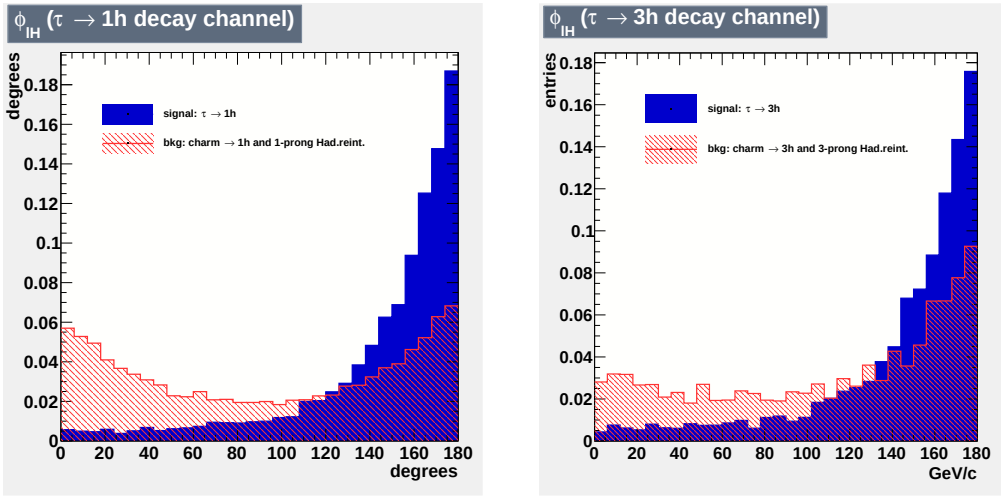

(a) (b)

Figure 3.1. ϕ_{lH} angle distribution for signal (white area) and charm background (red shaded area) for single hadron and three hadrons decay channel.

Track Follow Down In order to reduce the muon identification inefficiency, primary tracks of the events fulfilling previous selections are followed along the downstream ECC, with an angular acceptance up to $\tan\theta = 1$, until either a stopping point, an interaction or a muon decay topology is found. This procedure is called *Track Follow-Down* (TFD) and allows to discriminate between muons and hadrons using the topology at the end point, momentum-range correlations, track length and energy loss in proximity of the stopping point.

Momentum-range correlation is characterised by the following discriminating variable:

$$D_{TFD} = \frac{L}{R_{lead}(p)} \frac{\rho_{lead}}{\langle\rho\rangle} \tag{3.1.1}$$

where L is the track length, $R_{lead}(p)$ is the range in lead of a muon with a momentum p, $\langle\rho\rangle$ is the average density along the path and ρ_{lead} is the lead density. A cut value is defined from the distribution of D_{TFD} to separate muons and hadrons as shown in fig. 3.2. According to this selection, a track is classified as a muon if it has $D_{TFD} > 0.8$, as a hadron if $D_{TFD} < 0.6$.

This procedure results in a significant reduction of the background due to the not identification of primary μ in the ED, namely ν_μCC charm production for all decay channels and hadron re-interactions in ν_μCC events for the hadronic decay channels.

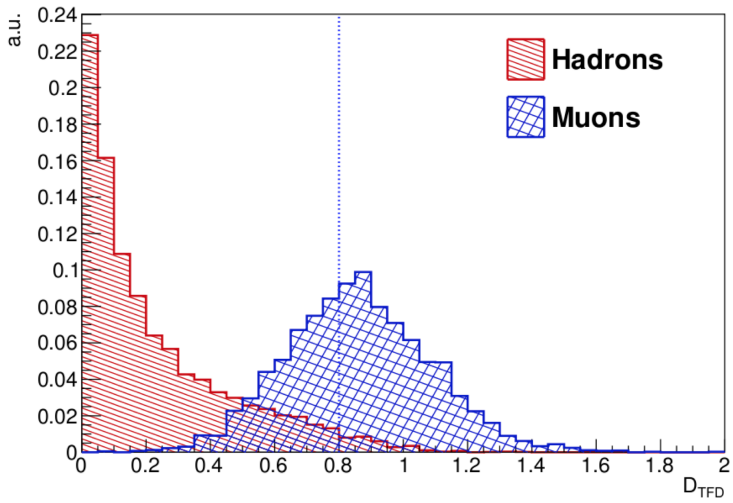

Figure 3.2. D_{TFD} distribution for hadrons and muon tracks. Blue line represents the cut above which a track is classified as muon

Large angle track search An indication of hadron re-interactions comes from highly ionizing particles, which are the low energy protons or nuclear fragments produced as a result of a nuclear evaporation process initiated by the primary particle interactions. These particles leave a visible black track in the emulsion.

To reduce the hadron re-interaction background, an automatic image analysis tool with an angular resolution up to $\tan\theta = 3$ has been developed and 40% additional reduction in the background has been achieved.

The expected numbers of signal and background events for each decay channel are summarised in table 3.3, normalised to the sample in table 3.1. Assuming $\Delta m^2_{23} = 2.44 \cdot 10^3$ eV^2 [116] and $\sin^2 2\theta_{23} = 1$, the total expected signal is 2.64 ± 0.53 events, whereas the total background expectation is 0.25 ± 0.05 events [2].

Five ν_τ candidates, surviving the kinematical cuts reported in table 3.2 have been found and will be described in the following. All the τ candidate events have been analysed both in European and Japanese laboratories, finding consistent measurements. The mean values were used for the analysis.

Channel	Expected Background				Expected Signal
	Charm	Had. re-interaction	Large μ-scat.	Total	
$\tau \to 1h$	0.017 ± 0.003	0.022 ± 0.006	–	0.04 ± 0.01	0.52 ± 0.10
$\tau \to 3h$	0.17 ± 0.03	0.003 ± 0.001	–	0.17 ± 0.03	0.73 ± 0.14
$\tau \to \mu$	0.004 ± 0.001	–	0.0002 ± 0.0001	0.004 ± 0.001	0.61 ± 0.12
$\tau \to e$	0.03 ± 0.01	–	–	0.03 ± 0.01	0.78 ± 0.16
Total	0.22 ± 0.04	0.02 ± 0.01	0.0002 ± 0.0001	0.25 ± 0.05	2.64 ± 0.53

Table 3.3. Expected signal and background events for the analysed data sample

3.1.2 The first four candidates

First ν_τ candidate

The first ν_τ interaction occurred in a brick situated in wall 11 of the first SM and well inside the target (3 bricks from the top and 24 bricks from the left), on 22 August 2009 [111]. The position of the brick allowed a comprehensive study of the event: the Track Follow Down procedure was performed and secondary vertices, including electromagnetic showers, were searched for in a large volume.

fig. 3.3 shows a zoom of the electronic detector on the interaction region. No muon was identified by electronic detector reconstruction.

The ν interaction occurred in the lead plate between film 18 and 19, 6.5 X_0 far from the downstream edge of the brick. The interaction was fully reconstructed in the brick, looking for tracks within an angular acceptance of 1 rad.

The complete picture of the event at the emulsion level is shown in figures 3.4 and 3.5. The primary neutrino interaction is defined by 7 tracks, one of which exhibits a visible kink. Two electromagnetic showers caused by γ-rays were located and are associated with the event. All the tracks of the event are described below, following the notation in figures 3.4 and 3.5:

- Track 1 was left by a particle of momentum $0.78^{+0.13}_{-0.10}$ GeV/c, likely interacting in the target tracker: the track, indeed, exits from the primary interaction brick, but was not found in the brick immediately downstream. Using the momentum-range correlation it was identified as a hadron, being the $D_{TFD} = 0.1$.

- Track 2, attached at primary vertex, shows high ionization and stops inside the brick. From its residual range (32.0 ± 0.5) g·cm^{-2} and the value of $p\beta = 0.32^{+0.31}_{-0.11}$ GeV/c, measured on the upstream half of the track, the particle was identified as a proton and the kaon hypothesis was rejected with 97%

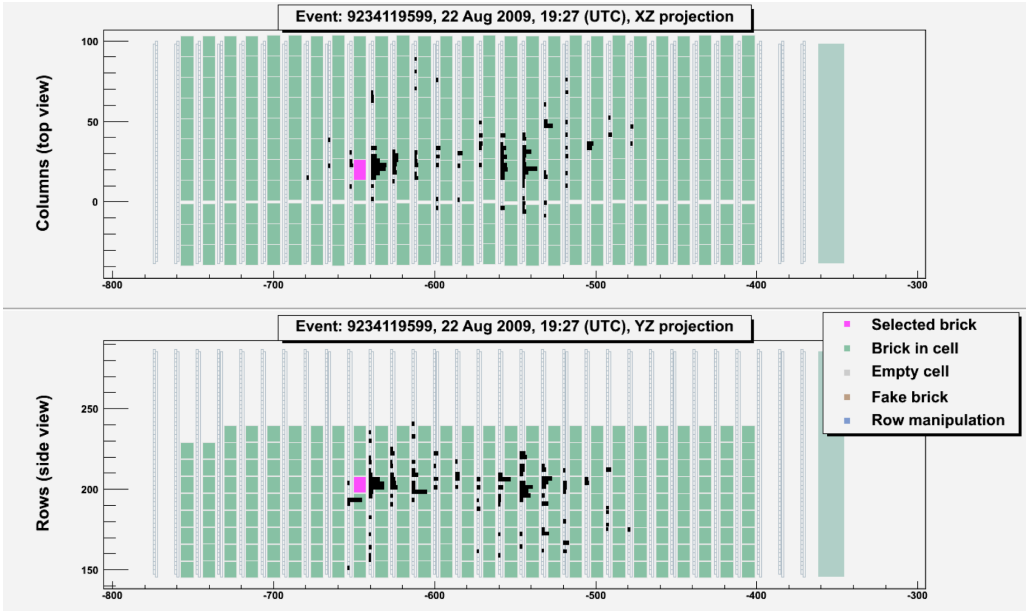

Figure 3.3. Electronic detector display of the first ν_τ candidate event: zoom on the interaction region. The brick containing the interaction is highlighted in magenta

C.L. The proton momentum, resulting from the residual range, corresponded to (0.60 ± 0.05) GeV/c.

- Track 3 was found on CSD and attached to the primary vertex. Its momentum is $1.97^{+0.33}_{-0.25}$ GeV/c. It made a 2-prong interaction in the fourth brick downstream of the primary vertex.

- Track 4 is the τ candidate given its kink topology with $\theta_{kink} = (41 \pm 2)$ mrad, after a path length of (1335 ± 35) μm.

- Track 5 was found on CSD and attached to the primary vertex. It was followed in the downstream walls and disappeared in wall 13 after a total distance of 174 g·cm^{-2}, with a measured momentum of $1.30^{+0.22}_{-0.16}$ GeV/c, allowing to classify it as a hadron, having $D_{TFD} = 0.27$.

- Track 6 ends in the brick containing the primary vertex. It was classified as a pion of very low momentum $0.36^{+0.18}_{-0.09}$ GeV/c. For this track $D_{TFD} = 0.15$.

- Track 7 starts two lead plates downstream of the primary vertex, stops in the same brick and is not directly attached to the primary vertex, being its impact parameter $IP = 43^{+45}_{-43}$ μm. It was likely originated by a prompt neutral

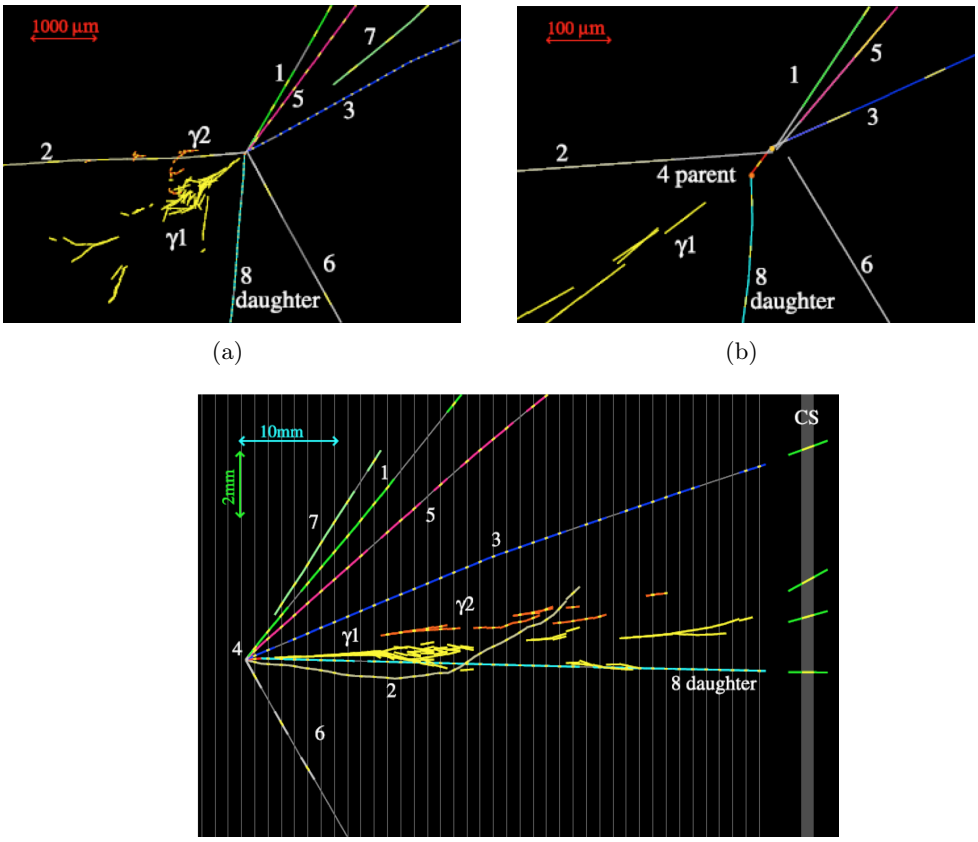

Figure 3.4. Display of the first ν_τ candidate event, as reconstructed in the emulsion films: (a) view transverse to the neutrino direction; (b) zoom on the vertices for the same view; (c) longitudinal view

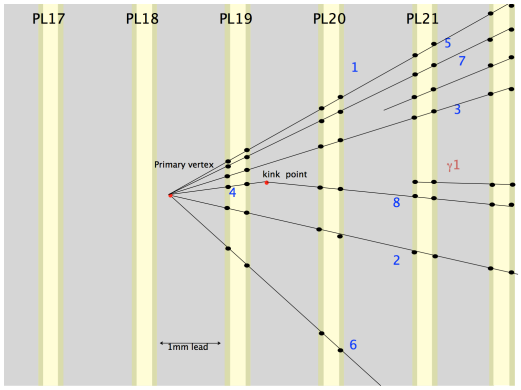

Figure 3.5. Schematic picture of the first ν_τ candidate event. Zoom on the primary and secondary vertices. Tracks 1 to 7 come from the primary vertex; track 4 is the τ candidate decaying in the lead plate between film 19 and film 20, track 8 is the decay daughter. The starting point of the shower originating from track 1 is also visible in the film 21

particle. Its momentum $0.49^{+0.29}_{-0.13}$ GeV/c was added to the total momentum at the primary vertex.

- Track 8 is the τ daughter. It was found on CSD, but was not attached to primary vertex because of the high impact parameter: (55 ± 4) μm. It was left by a high momentum particle of 12^{+6}_{-3} GeV/c and generated a 2-prong interaction, 7 walls downstream of its emission vertex.

- Shower 1 originated from track 1, 2.2 mm downstream of the secondary vertex. The probability that it pointed to secondary vertex was estimated to be 32%, the impact parameter being (7.5 ± 4.3) μm, while the probability that it was attached to primary vertex was less than 10^{-3}, the IP being (45.0 ± 7.7) μm.

- Shower 2 was compatible with pointing to both vertices, with a significantly larger probability of 82% at the secondary vertex, the IP being 22^{+25}_{-23} μm, while the probability that it was related to primary vertex was 10%, with $IP = (85 \pm 38)$ μm. Its distance to both vertices is about 13 mm and its energy $(1.2 \pm 0.4(stat.) \pm 0.4(syst.))$ GeV.

Thanks to TFD, all tracks were classified as hadrons. The probability that tracks 1, 5 and 6 belonged to muons was estimated to be less than 0.001. The remaining tracks were identified as hadrons through their interaction. None of the charged particles emitted at either vertices was compatible with being produced by an electron. A scanning with an angular acceptance up to $\tan\theta = 3$ was performed and no additional tracks were found.

In table 3.4 the results of the topological and kinematical analysis for this event are reported, together with the selection criteria defined for the $\tau \to 1h$ decay channel. All variables considered pass the selection cuts necessary to define a ν_τ candidate.

Variable	**Selection cut**	**Measurement**
z_{dec} (μm)	$[44, 2600]$	435 ± 35
p^T_{miss} (GeV/c)	<1	$0.570^{+0.320}_{-0.170}$
ϕ_{lH} $(degrees)$	>90	173 ± 2
p^T_{2ry} (GeV/c)	>0.3 (γ attached)	$0.470^{-0.120}_{+0.230}$
p_{2ry} (GeV/c)	>2	12^{+6}_{-3}
θ_{kink} (rad)	>0.02	0.041 ± 0.002

Table 3.4. Selection criteria for ν_τ candidate events in the $\tau \to 1h$ decay channel and corresponding measured values for the first observed candidate

The second ν_τ candidate

The second ν_τ candidate interaction occurred on 23 April 2011 in a brick situated in the wall 4 of the first SM [112]. The display of the ED is shown in fig. 3.6. No muon track was reconstructed by electronic detectors and the estimated hadronic energy is (22.0 ± 6.2) GeV, so it was classified as 0μ.

The scan-back procedure was applied to the tracks found on CSD and the total-scan was performed around their stopping point. The neutrino interaction occurred in the lead plate between film 22 and film 23, 6.1 X_0 far from the downstream edge of the brick. The complete picture of the event at the emulsion level is shown in fig. 3.7.

Primary vertex (V_0 in fig. 3.7) lies close to the downstream emulsion film, at a depth in lead of only 120 μm, and consists of two tracks, the τ lepton candidate and another hadronic track, called p_0. A nuclear fragment going forward was also detected at a large angle and associated to the primary vertex, with an $IP = 15$ μm.

The τ lepton decay occurred in the plastic base (V_1 in fig. 3.7), showing a trident topology after a flight length of (1466 ± 10) μm. Having found the decay vertex in the plastic base allowed to exclude the emission of highly ionising nuclear fragments with an efficiency above 99.8% at 90% C.L. up to $\tan\theta = 3$ [117].

The details about the reconstructed tracks are reported in the following:

- Track 1 (p_0) was found on CS and attached to the primary vertex. Its measured momentum is (2.8 ± 0.7) GeV/c. It was classified as a hadron, since $D_{TFD} = 0.05$.

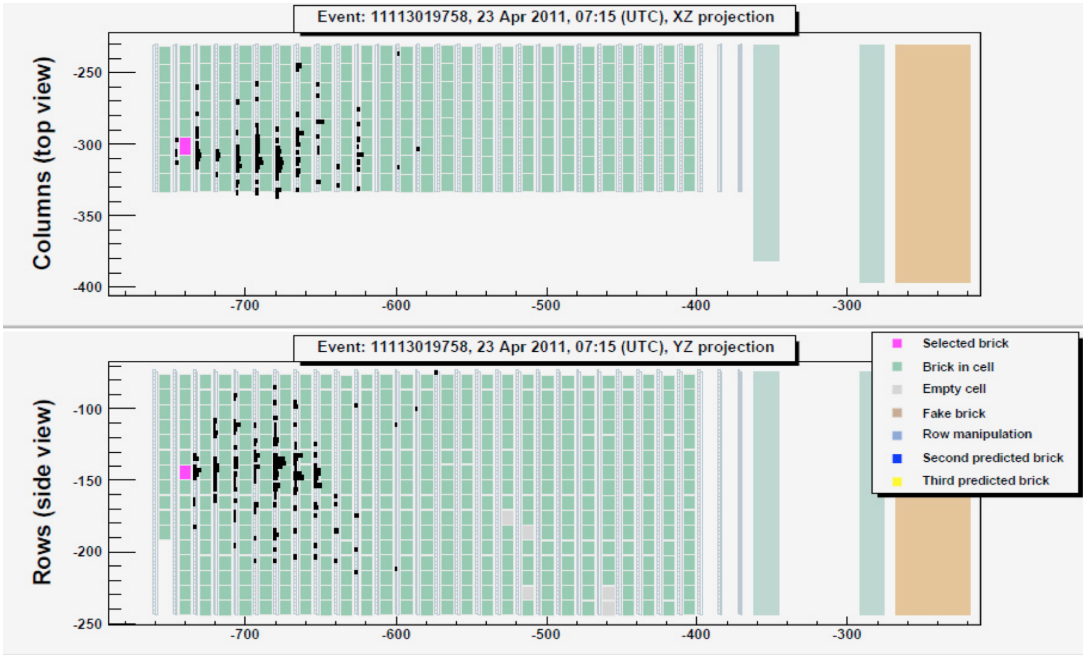

Figure 3.6. Electronic detector display of the second ν_τ candidate event: zoom on the interaction region. The brick containing the interaction is highlighted in magenta

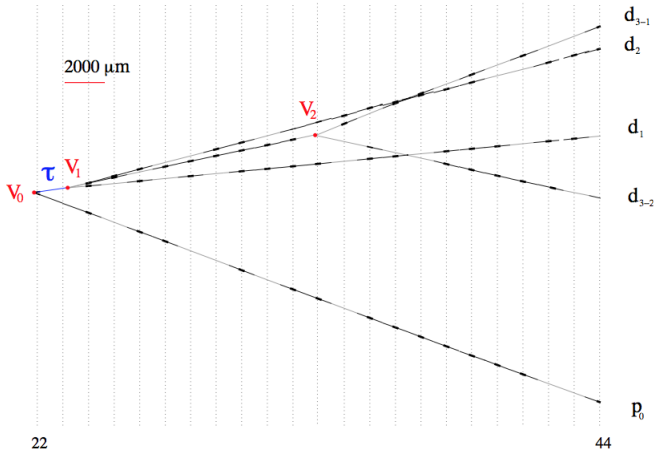

Figure 3.7. Event display of second ν_τ candidate: reconstruction in the brick (side-view). Vertical lines indicate the position of the middle-point of emulsion films 22 to 44, numbering them from 1 to 57 according to their increasing z coordinate. The black segments represent reconstructed base-tracks while the grey lines are the result of the track fit

- Track 2 is the τ candidate.
- Track 3 (d_1) is one of the three decay daughters. It has a measured momentum of $6.6^{+2.0}_{-1.4}$ GeV/c and $IP = (70 \pm 5)$ μm with respect to the primary vertex. It generates a 2-prong interaction 4 bricks downstream.
- Track 4 (d_2) is the second τ daughter, with an $IP = (61 \pm 5)$ μm w.r.t. the primary vertex. Its measured momentum is (1.3 ± 0.2) GeV/c. It has $D_{TFD} = 0.25$, due to the fact that its stopping point is two walls downstream, and therefore was identified as a hadron.
- Track 5 (d_3) is the last τ daughter. Its IP w.r.t. the primary vertex is (170 ± 5) μm and its measured momentum is $2.0^{+0.9}_{-0.6}$ GeV/c. It interacted 1.3 cm downstream, in the same brick containing the neutrino vertex. The final state is composed of two charged tracks and four back-scattered nuclear fragments.

Table 3.5 shows the values of the decay topological and kinematical quantities computed for this event, together with the selection criteria defined for the $\tau \to 3h$ decay channel. All variables pass the selection cuts required to select a τ candidate.

Variable	**Selection cut**	**Measurement**
z_{dec} (μm)	<2600	1446 ± 10
p^T_{miss} (GeV/c)	<1	0.31 ± 0.11
ϕ_{lH} $(degrees)$	>90	167.8 ± 1.1
p_{2ry} (GeV/c)	>3	8.4 ± 1.7
θ_{kink} (rad)	<0.5	0.0874 ± 0.015
m (GeV/c^2)	$[0.5, 2]$	0.96 ± 0.13
m_{min} (GeV/c^2)	$[0.5, 2]$	0.80 ± 0.12

Table 3.5. Selection criteria for ν_τ candidate events in the $\tau \to 3h$ decay channel and corresponding measured values for the observed candidate

The third ν_τ candidate

The third ν_τ interaction found in the OPERA analysis occurred on 2 May 2012 in a brick situated in the wall 8 of the first SM [113]. Fig. 3.8 shows the electronic detector display of this event.

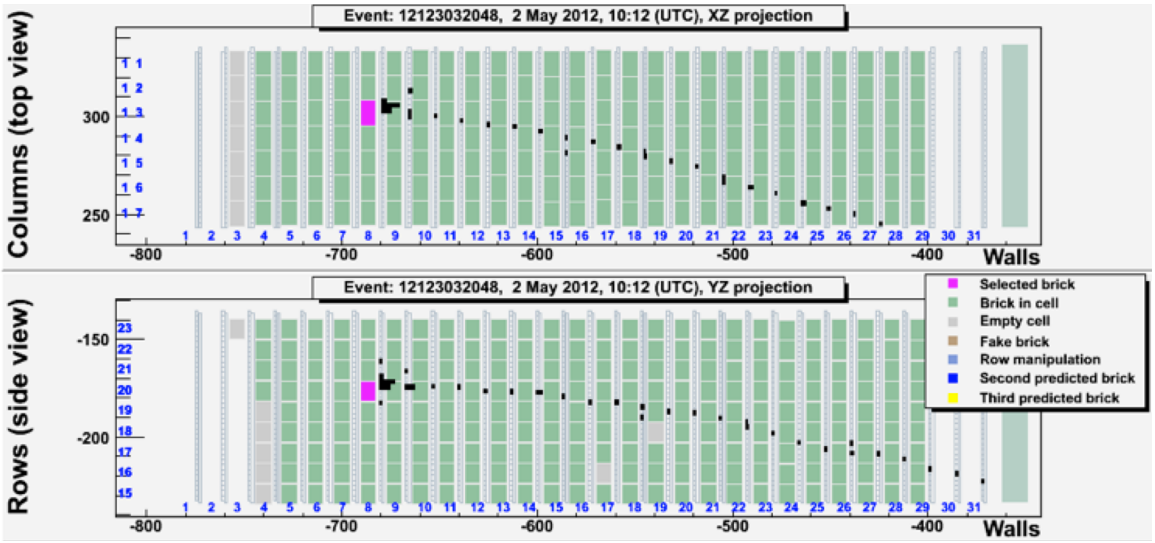

Figure 3.8. Electronic detector display of the third ν_τ candidate event: zoom on the interaction region. The brick containing the interaction is highlighted in magenta

An isolated, penetrating track was reconstructed in the electronic detectors: the particle was recorded in 24 TT planes and crossed 6 RPC planes before stopping in the spectrometer. This range corresponds to 1650 g/cm^2 of material.

The scanning of the CSD of the interaction brick was performed around the electronic detector prediction and 6 tracks were found, one matching the muon direction. A converging path was also found. The muon track was found as well as a converging pattern, satisfying the conditions for event validation.

The neutrino interaction occurred well inside the brick, 3.3 X_0 from its downstream face. All tracks possibly related to the interaction were searched for in the brick with an angular acceptance up to $\tan\theta = 1$. The display of the event as reconstructed in the brick is shown in fig. 3.9.

The primary vertex (V_0) consists of two tracks: the τ lepton candidate and a hadron track (p_0) having a distance of closest approach of (0.5 ± 0.5) μm. The τ lepton decay occurred after a flight length of (376 ± 10) μm in the plastic base of the first film immediately downstream of the primary vertex. The decay particle is compatible with the muon track reconstructed in the electronic detectors.
An electromagnetic shower produced by a γ-ray and pointing to the primary vertex was also observed.

The details about the reconstructed tracks are reported in the following:

- Track 1 (p_0) was found on CS and attached to the primary vertex. Its momentum, measured by MCS, is $0.90^{+0.18}_{-0.13}$ GeV/c. Its interaction in the downstream

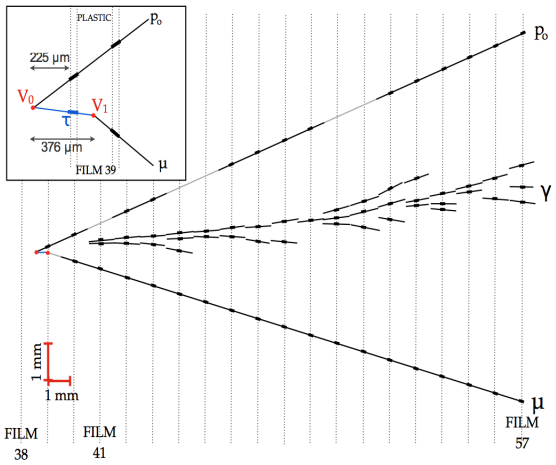

Figure 3.9. Display of the third candidate event in the xz projection: tracks τ and p_0 come from the primary vertex; the τ candidate decays in the plastic base of film 39, track d_1 is the τ decay daughter identified as a muon. The starting point of the shower generated by the γ is visible in film 41

wall was reconstructed, but no charged particle track could be detected at the interaction point. Having $D_{TFD} = 0.1$ it was classified as a hadron by the momentum-range correlation.

- Track 2 is the τ candidate. It exhibits a decay topology in one prong after a flight length of (376 ± 10) μm.
- Track 3 (d_1) is the τ daughter, with $\theta_{kink} = (245 \pm 5)$ mrad and $IP = (93.7 \pm 1.1)$ μm w.r.t. the primary vertex. The track was found on the CSD, and it is in agreement with the muon track reconstructed in the electronic detectors both in momentum ($\Delta p = 0.3^{+0.9}_{-0.5}$ GeV/c) and angle ($\Delta\theta = (18 \pm 25)$ mrad).
- The electromagnetic shower has an energy of $3.1^{+0.9}_{-0.6}$ GeV and originates from γ-ray conversion, 2.1 mm downstream of the primary vertex. It is compatible with pointing to primary vertex with an the impact parameter of (18 ± 13) μm. Its probability to be attached to the secondary vertex is less than 10^{-3}, the impact parameter being (96 ± 12) μm.

The muon momentum at the interaction vertex was accurately estimated from the range of the particle in the electronic detector: a Kalman filter-based algorithm yielded a value of $p_\mu = (2.8 \pm 0.2)$ GeV/c, compatible with the value found using measurements based on the emulsion data and MCS: $3.1^{+0.9}_{-0.5}$ GeV/c.

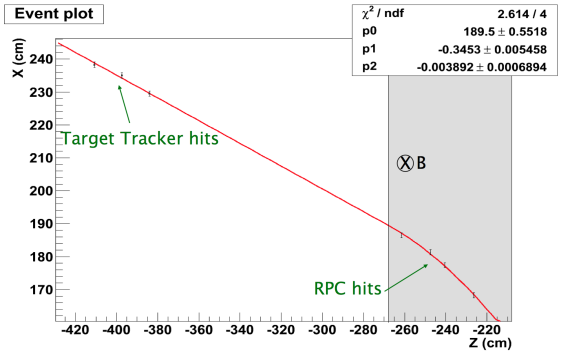

Figure 3.10. TT and RPC hits are used to perform the muon charge measurement. A fit is performed with a straight line in the not magnetized region (TT hits) and with a parabola in the magnetized region (RPC)

The charge of the secondary muon track must either be measured to be negative or be undetermined in order to classify the event as ν_τ candidate. For the charge measurement, the bending of the track in the magnetised iron was used. In this case, four available RPC hits were available, while no hits could be recorded by the PT planes due to an inefficiency of the trigger (the trigger is given by a 2 out of 3 majority of the first RPC plane within the magnet and two upstream dedicated RPC planes, the so-called XPC planes [90]). A fit was performed (as shown in fig. 3.10) with a straight line in the not magnetized region (TT hits) and with a parabola in the magnetized region (RPC hits). The parabolic part was meant to approximate the circular trajectory. The fit gave a parabola with the concavity towards the bottom, corresponding to a radius of ~ 85 cm. Given the direction of the magnetic field, this is compatible with a negative charge with a significance of 5.6σ.

Table 3.6 shows the value of the decay topological and kinematical quantities computed for this event, together with the selection criteria defined for the $\tau \to \mu$ decay channel. All variables pass the selection cuts required to identify a τ candidate.

Variable	**Selection cut**	**Measurement**
z_{dec} (μm)	$[44, 2600]$	151 ± 10
p^T_{2ry} (GeV/c)	>0.25	0.690 ± 0.050
p_{2ry} (GeV/c)	$[1, 15]$	2.8 ± 0.2
θ_{kink} (rad)	>0.02	0.245 ± 0.005

Table 3.6. Selection criteria for ν_τ candidate events in the $\tau \to \mu$ decay channel and corresponding measured values for the observed candidate

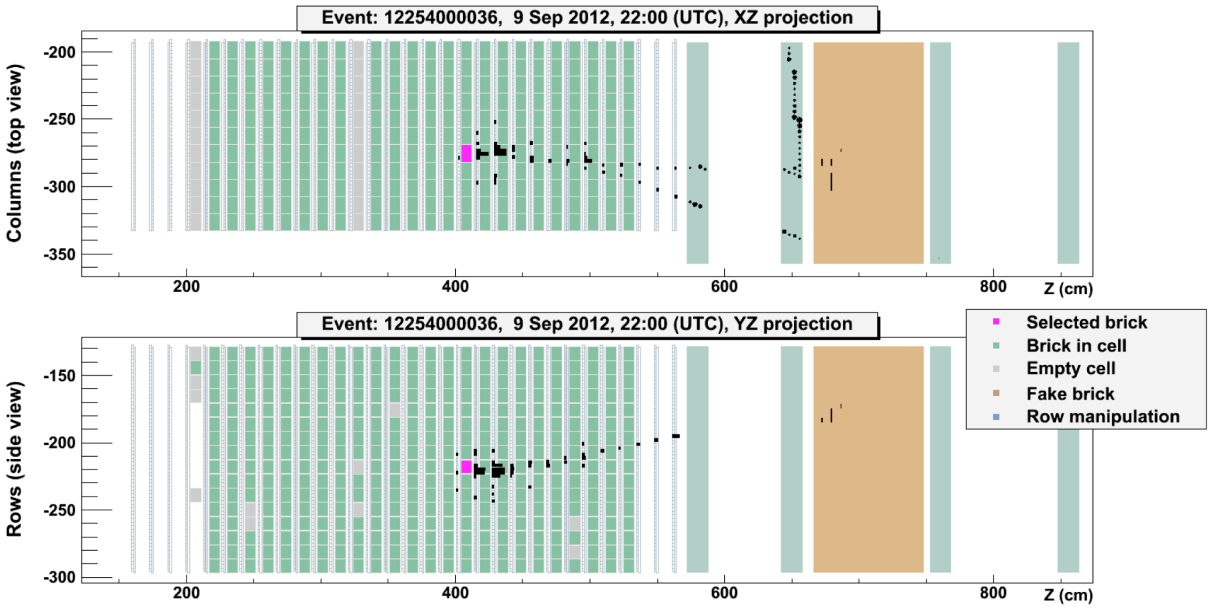

Figure 3.11. Electronic detector display of the fourth ν_τ candidate event: zoom on the interaction region. The brick containing the interaction is highlighted in magenta

The fourth ν_τ candidate

The fourth neutrino interaction occurred on 9 September 2012 in the second SM, 10 brick walls upstream of the spectrometer [114]. No muon track was reconstructed by the electronic detectors and the event was classified as 0μ. Fig. 3.11 shows the display of the event as seen by the electronic detectors.

The CSD scan revealed a converging path of 10 tracks. By following back these tracks with the scan-back method, the neutrino interaction was located 18 plates from the downstream face. The primary vertex is defined by four tracks, one of which has a kink topology. In addition, two electromagnetic showers originated by the conversion of γ-rays were detected, both pointing to the primary vertex. The complete topology of the event as reconstructed in emulsion is shown in fig. 3.12 and is described in the following.

- Track 1 corresponds to the τ candidate, which decays after a flight length of (1090 ± 30) μm with a θ_{kink} of (137 ± 4) mrad.
- Track 2 has a momentum of $1.9^{+0.3}_{-0.2}$ GeV/c. It was followed in the downstream bricks till the end of the target. The track entered the spectrometer, leaving hits in the PT but not in the RPC.

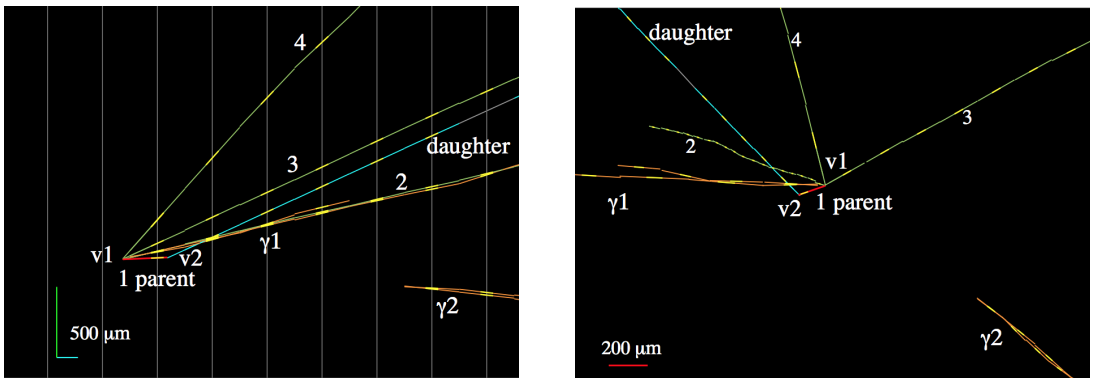

(a) (b)

Figure 3.12. Event display of the fourth ν_τ candidate event as seen in emulsion a) in the y-z projection longitudinal to the neutrino direction and b) in the view transverse to the neutrino direction. The primary and decay vertices are indicated as "v1" and "v2" respectively

- Track 3 has a momentum of $1.1^{+0.2}_{-0.1}$ GeV/c and undergoes an interaction just before entering the second downstream brick, giving origin to a 2-prong vertex.
- Track 4 is a heavily ionising particle having $p\beta = (0.4 \pm 0.1)$ GeV/c. It stops between the first and second downstream bricks. Having range $= (94 \pm 1)$ g/cm^2 and momentum (0.7 ± 0.1) GeV/c, the particle was identified as a proton by the momentum-range correlation.
- Track 5 is the kink daughter, and has a measured momentum of $6.0^{+2.2}_{-1.2}$ GeV/c. Its impact parameter is (146 ± 5) μm w.r.t. the primary vertex. It was followed in the downstream bricks till it exited the target, stopping in the spectrometer after leaving a signal in three RPC planes.

All the quantities evaluated for this τ candidate are reported in table 3.7 and pass the kinematical cuts defined for the $\tau \to 1h$ decay channel.

3.1.3 The fifth ν_τ candidate

The fifth ν_τ candidate occurred on 14 August 2012 in the second SM, 7 brick walls upstream of the spectrometer [2]. No muon track was reconstructed by the ED and the event was classified as 0μ. The activity in the TT was limited to the 8 walls downstream of the vertex brick, as it can be seen in fig. 3.13. The visible energy of the event is (12 ± 4) GeV.

In the CDS analysis 15 tracks were detected, six of which showed a converging path, thus validating the brick extraction and development. By following back these

Variable	Selection cut	Measurement
z_{dec} (μm)	$[44, 2600]$	406 ± 30
p^T_{miss} (GeV/c)	<1	$0.55^{+0.3}_{-0.2}$
ϕ_{lH} $(degrees)$	>90	166^{+2}_{-31}
p^T_{2ry} (GeV/c)	>0.3 (γ attached)	$0.82^{-0.16}_{+0.30}$
p_{2ry} (GeV/c)	>2	$6^{+2.2}_{-1.2}$
θ_{kink} (rad)	>0.02	0.137 ± 0.004

Table 3.7. Selection criteria for ν_τ candidate events in the $\tau \to 1h$ decay channel and corresponding measured values for the fourth observed τ candidate

tracks with the scan-back procedure, the neutrino interaction was located 42 plates from the downstream face and the total-scan was performed.

The neutrino interaction vertex consists of two charged tracks, one of which exhibits a kink topology after a flight length of (960 ± 30) μm (see fig. 3.14). The distance of closest approach between the τ candidate and the other primary track is 0.1 μm.

In addition to these two tracks, four forward-going and two backward-going nuclear fragments pointing to the primary vertex were observed. The search for nuclear fragments will be discussed in a dedicated paragraph.

The τ daughter interacted after having crossed 22 plates, producing four charged particles and a photon, and could thus be unambiguously identified as a hadron. The complete topology of the event as observed in the ECC brick can be seen in fig. 3.14.

All tracks related to the events will be now described.

- Track 1 is the τ candidate, which exhibits a kink of (90 ± 2) mrad.
- Track 2 (p_1) is the other primary charged track. Its measured momentum is (1.1 ± 0.2) GeV/c and it was classified as a proton from its energy loss in the emulsion target. The linear density of grains along the track left by a particle, indeed, is correlated with its energy loss. The ratio between the grain density of this track and that of the τ daughter track is (1.45 ± 0.06), to be compared with (1.38 ± 0.14) expected for a proton/m.i.p. ratio. Therefore, track 2 is likely formed by a proton [118].
- Track 3 is the daughter track, with a measured momentum of $11.0^{+13.9}_{-3.9}$ GeV/c. Its IP w.r.t. the primary vertex is (83 ± 5) μm.

The measured values for this τ candidate are summarised in table 3.8, together with the criteria to validate a $\tau \to 1h$ candidate. The event satisfied all the cuts.

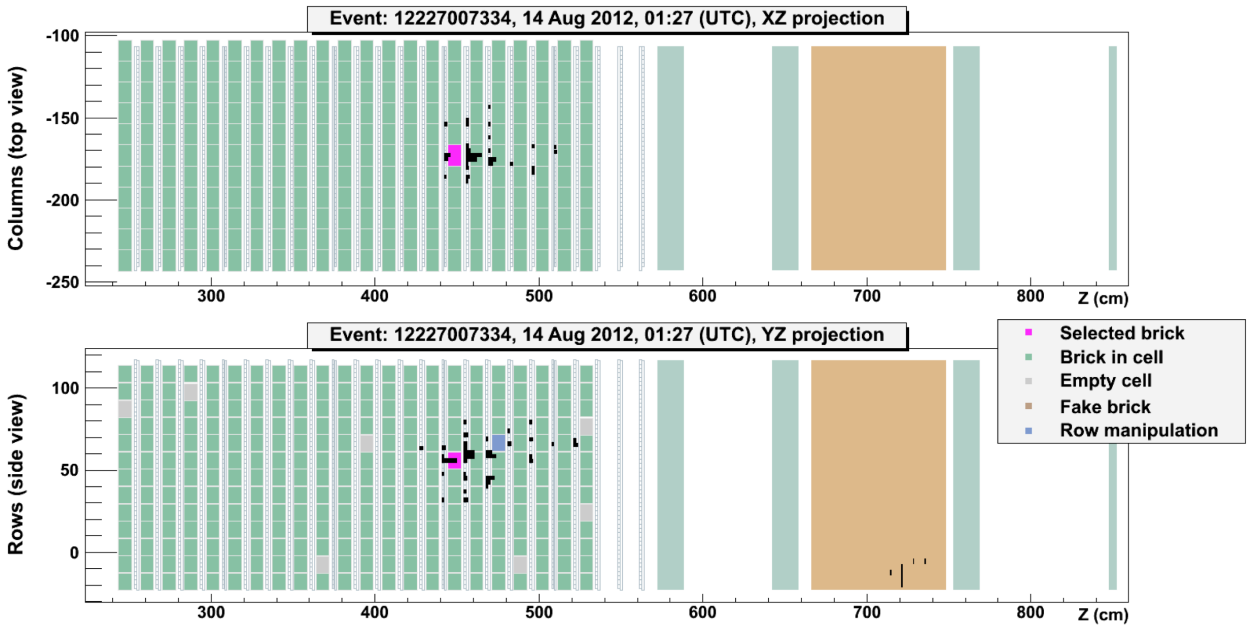

Figure 3.13. Electronic detector display of the fifth ν_τ candidate event: zoom on the interaction region. The brick containing the interaction is highlighted in magenta

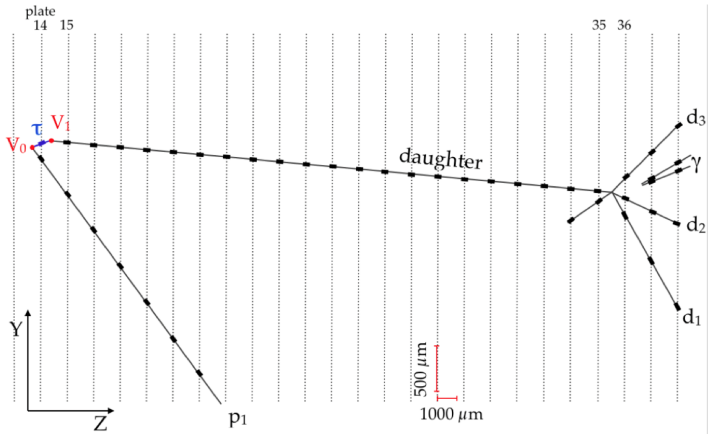

Figure 3.14. Event display of the fifth ν_τ candidate event in the horizontal projection longitudinal to the neutrino direction. The primary and secondary vertices are indicated as V_0 and V_1, respectively. The black stubs represent the track segments as measured in the films

Variable	Selection cut	Measurement
z_{dec} (μm)	$[44, 2600]$	630 ± 30
p^T_{miss} (GeV/c)	<1	0.3 ± 0.1
ϕ_{lH} $(degrees)$	>90	151 ± 1
p^T_{2ry} (GeV/c)	>0.6	$1.0^{+1.2}_{-0.4}$
p_{2ry} (GeV/c)	>2	11^{+14}_{-4}
θ_{kink} (rad)	>0.02	0.090 ± 0.002

Table 3.8. Selection criteria for ν_τ candidate events in the $\tau \to 1h$ decay channel and corresponding measured values for the fifth observed ν_τ candidate

Large angle track search

For all τ candidates, a search for nuclear fragments has been performed both upstream and downstream of the primary and decay vertices up to $\tan\theta = 3$, θ being the angle of the track with respect to the z axis.

Finding nuclear fragments in the forward and/or backward hemisphere is a further signature of the neutrino interaction, in case they point to the primary vertex. On the other hand, highly ionising tracks associated with nuclear fragments pointing to the secondary vertex would indicate the presence of hadronic activity and are a signature for hadronic re-interaction background. The identification of nuclear fragments is therefore used to reject background.

For the fifth ν_τ candidate, this task was assigned to the Naples scanning Laboratory and to the Toho (Japan) scanning Laboratory for a cross-check.

Nuclear emulsions do not have any intrinsic limit to detect particle direction, but standard scanning systems have been initially designed to recognize tracks within a limited angular acceptance. To perform the large angle scanning, a new fast scanning system, developed by the Napoli group with the aim of extending the track recognition to a wider angular range and improving the scanning speed, has been used [119].

I have been in charge of performing this analysis on behalf of the Naples scanning laboratory.

With this new scanning system, I scanned an area of (8×5) cm^2 around the neutrino vertex position ($20000 \leq x(\mu\text{m}) \leq 100000$, $49258 \leq y(\mu\text{m}) \leq 99258$), as shown in fig. 3.15, with an angular acceptance of $\tan\theta \leq 3$. The primary vertex occurred between film 13 and 14, while the secondary vertex between film 14 and 15. In total, 22 films were scanned, 2 upstream and 20 downstream the primary vertex.

First of all, I checked the quality of the scanning: the segment position distribu-

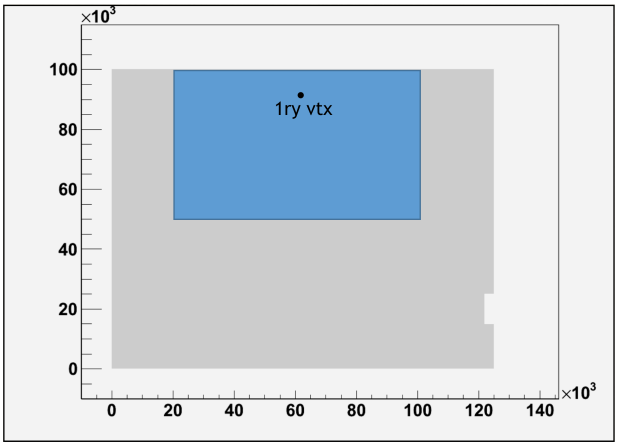

Figure 3.15. The area scanned for the large angle track search for the fifth ν_τ candidate is highlighted in blue. A total of 22 films were scanned, 2 upstream and 20 downstream the primary vertex

tion should be isotropic on the emulsion surface (x, y coordinates) and in all films (z coordinate). Even though vacuum is created between the emulsion to scan and the microscope stage where it is placed for the scanning, sometimes it can happen that some little bubbles of air remains entrapped, worsening segments acquisition. If a region with a minor number of segments was found, the origin of the problem was investigated and if it was not due to the emulsion quality, the plate was scanned again. The segment position distributions are reported in fig. 3.16, showing a good quality. The angle distribution of the reconstructed tracks is shown in fig. 3.17.

The efficiency as a function of track angle is evaluated as the ratio between the number of segments building up the track (N_{seg}) and the total number of crossed films (N_{pl}). Since by definition the first and last segments of a track are always present, the formula used for the efficiency evaluation is:

$$\frac{N_{seg} - 2}{N_{pl} - 2} \tag{3.1.2}$$

and results are reported in fig. 3.18.

After having validated the scanning performances for the scanned plates, I looked for large angle tracks both pointing to primary and secondary vertices. A selection criteria based on the impact parameter was applied, and the upper cut values for the different films are summarised in table 3.9.

The IP distribution for all the reconstructed tracks is shown in fig. 3.19 w.r.t. the primary (a) and the secondary (b) vertex.

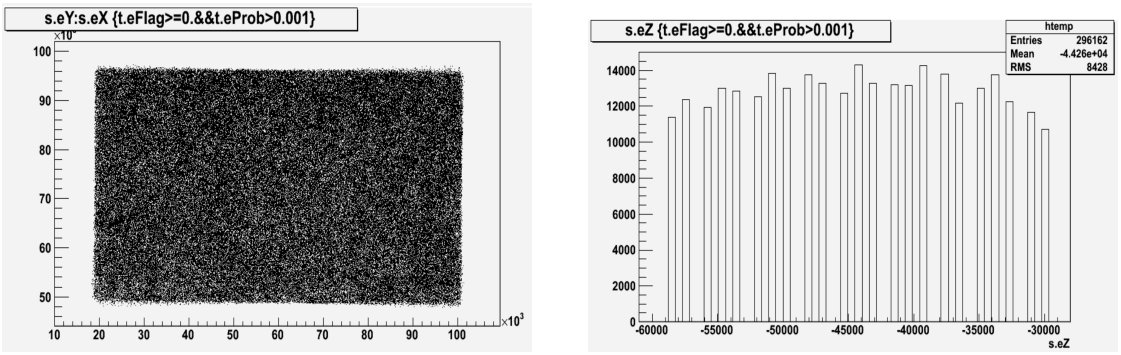

(a) (b)

Figure 3.16. Segment position for the scanned plates: a) $x - y$ distribution; b) z distribution

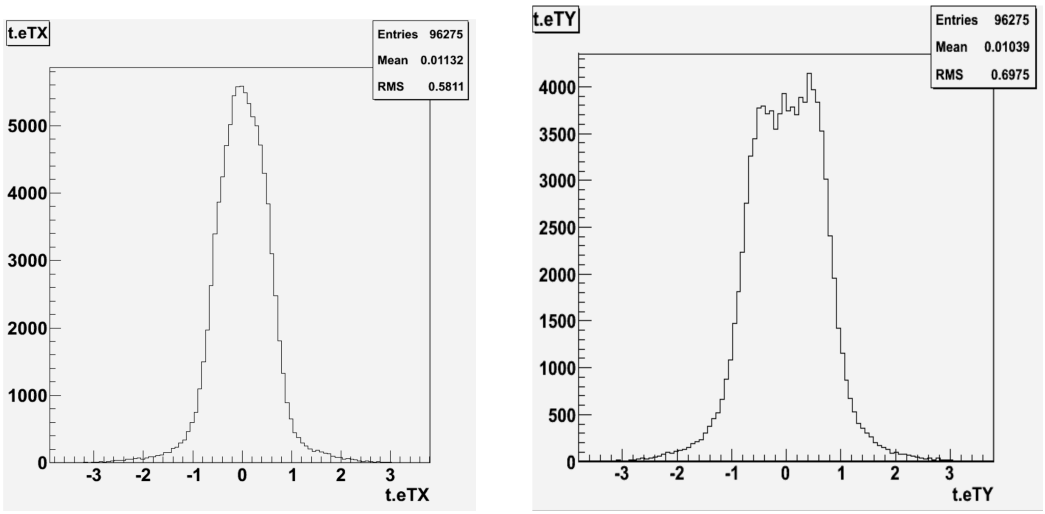

(a) (b)

Figure 3.17. Track angular distribution for the scanned plates: (a) slope x; (b) slope y

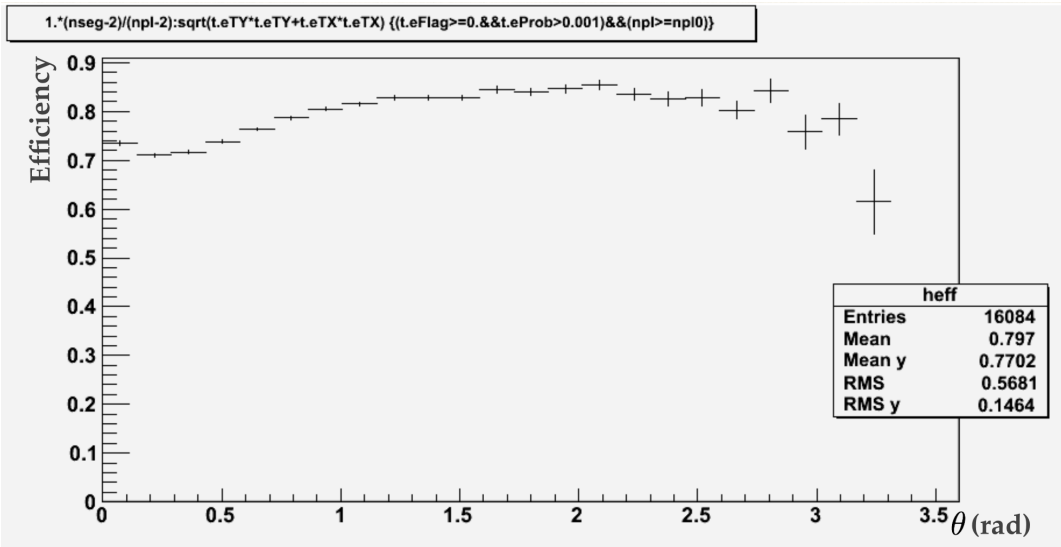

Figure 3.18. Track reconstruction efficiency as a function of the angle

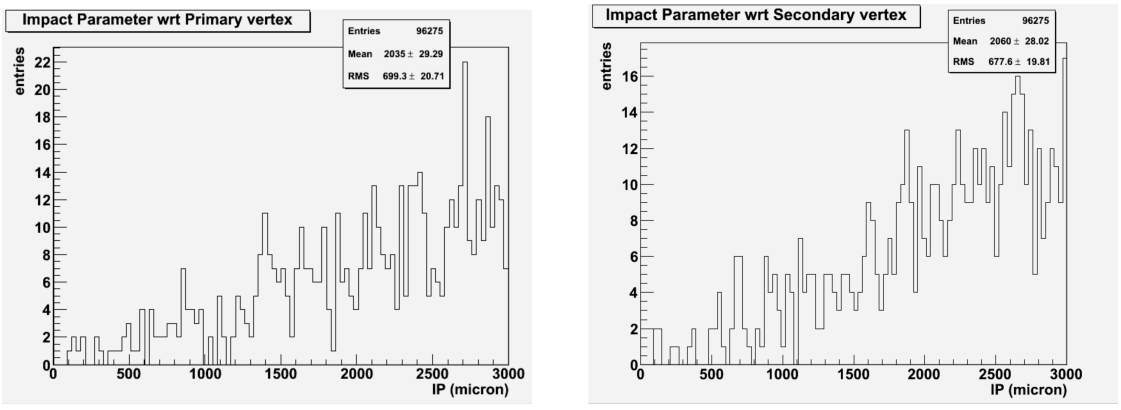

(a) (b)

Figure 3.19. Impact parameters for the reconstructed tracks: a) w.r.t. the primary vertex; b) w.r.t. the secondary vertex

	IP_{1ry} (μm)	IP_{2ry} (μm)
Plate 13	250	/
Plate 14	250	300
Plate 15	250	300
Plate 16	300	500

Table 3.9. Upper cut on the impact parameter for the large angle tracks search

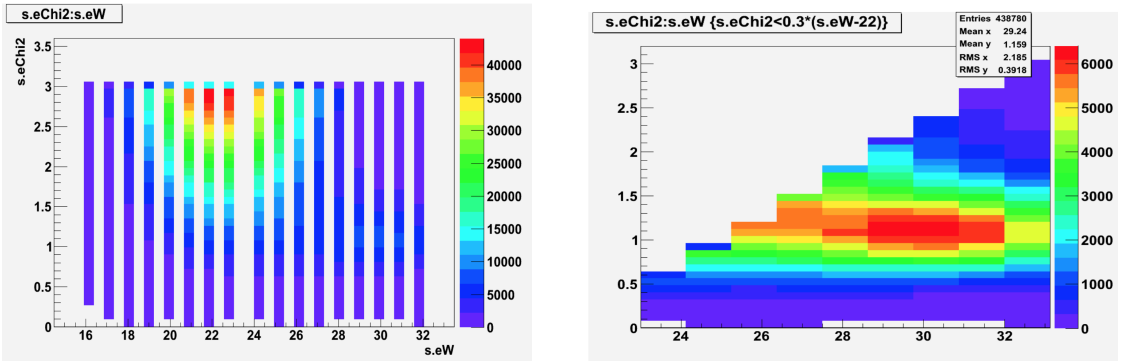

(a) (b)

Figure 3.20. χ^2 distribution versus W before the cut (a) and after the selection (b) defined in table 3.9

In total, 8 tracks were selected and visually inspected by myself. Only two of them were confirmed, corresponding to p_1 and the τ daughter candidate.

The following step was to search for single base-tracks pointing to primary or secondary vertices. In this case, the background is very high, so in addition to the cut on IP, I used a cut on the segment quality based on χ^2 and on the number of clusters (W) forming the base-track. An example is shown in fig. 3.21. The red region in the left plot, corresponding to $\chi^2 \sim 3$ and $W < 20$, is where the majority of fake base-tracks is, while signal is mostly in the region around $\chi^2 \sim 1$ and $W > 28$.

The cuts used, the number of base-tracks checked by eye and the ones confirmed are summarised in table 3.10.

The base-tracks confirmed were manually measured and their impact parameters w.r.t. primary and secondary vertices were computed. Six base-tracks, showing high ionization, were found to be related to the event under analysis, all pointing to primary vertex: four forward-going and two backward-going. No fragments were

	IP max w.r.t. 1ry vtx (μm)	IP max w.r.t. 2ry vtx (μm)	Quality cut	# of base-tracks checked	# of base-tracks confirmed
Plate 13	250	/	$\chi^2 < 0.3 \cdot (W - 22)$	78	7
Plate 14	250	300	$\chi^2 < 0.35 \cdot (W - 22)$	127	31
Plate 15	250	300	$\chi^2 < 0.35 \cdot (W - 23)$	150	21
Plate 16	300	500	$\chi^2 < 0.3 \cdot (W - 22)$	171	28

Table 3.10. Cut on the Impact Parameter for the large angle track search for the fifth ν_τ candidate

found pointing to the secondary vertex. This result confirms that the secondary vertex is not due to hadronic interaction, but consistent with that of a τ decay.

A schematic representation of all tracks and base-tracks related to the ν_τ event is shown in fig. 3.21. Details about slopes and IP of nuclear fragments, evaluated w.r.t. primary and secondary vertex, are reported in table 3.11, for each film.

Plate	**ID**	**Slope x**	**Slope y**	**IP**$_{1ry}$	**IP**$_{2ry}$
13	15 (black)	-0.274	0.445	19.8	/
	16 (black)	-0.444	1.188	51.1	/
14	parent	0.0798	0.0667	0.14	2.54
	p_1	-0.2697	-0.0745	0.09	270.6
	6 (black)	0.041	0.448	10.5	266.6
	7 (black)	0.345	0.575	31.5	321.7
	8 (black)	0.704	-0.162	47.5	356.1
	9 (black)	1.052	-0.213	16.3	516.5

Table 3.11. Details about slopes and impact parameters of all tracks related to the fifth ν_τ candidate. Tracks showing high ionization are indicated as "black"

BDT study

The neutrino interaction vertex of the fifth ν_τ candidate consists of the τ particle and a proton. This topology could be due to a Quasi Elastic (QE) interaction or a Deep-Inelastic Scattering (DIS) with some neutral particles undetected (QE-like). The schemes in fig. 3.22 illustrate the two cases.

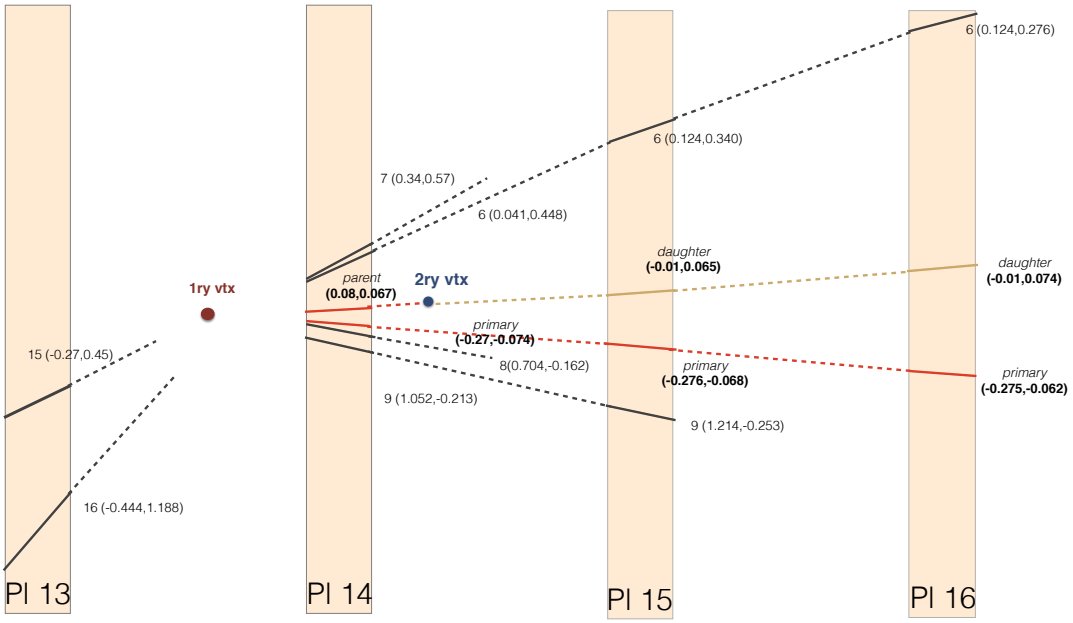

Figure 3.21. Draw of all the tracks and base-tracks found, related to the ν_τ event. Black thick lines correspond to particles with high ionization

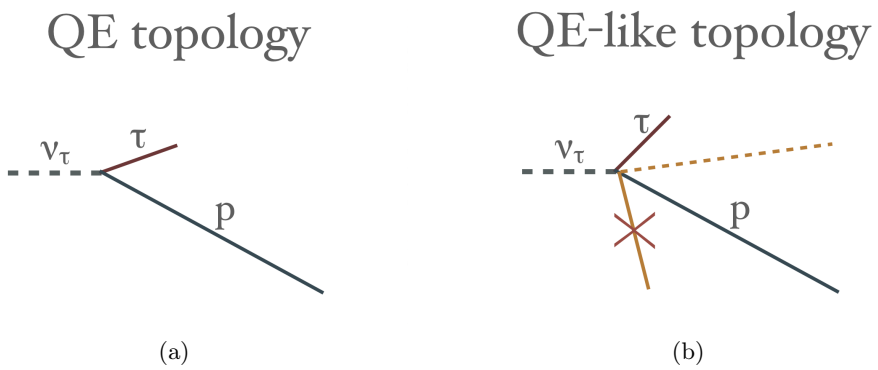

(a) (b)

Figure 3.22. Scheme of Quasi Elastic (a) and Quasi Elastic-like (b) neutrino interactions

In order to classify this event as QE or QE-like, I performed a multivariate analysis (MVA).

Using a sample of Monte Carlo ν_τ interactions with τ decaying into one single hadron, I evaluated the ratio of QE interactions on DIS, which is given by:

$$\frac{QE}{DIS} = \frac{\int \sigma_{QE_{\nu_\tau}} \phi_{\nu_\tau}\, dE}{\int \sigma_{DIS_{\nu_\tau}} \phi_{\nu_\tau}\, dE} = 0.20 \pm 0.04 \tag{3.1.3}$$

where the error takes into account the uncertainties on the ν_τ cross section which are about 10%.

The number of cases in which a DIS interaction is QE-like is:

$$\frac{QE\text{-}like}{DIS} = 0.070 \pm 0.002 \tag{3.1.4}$$

Therefore the ratio QE/QE-like is equal to:

$$\frac{QE}{QE\text{-}like} = \frac{QE}{DIS} \cdot \frac{DIS}{QE\text{-}like} = 2.8 \pm 0.6 \tag{3.1.5}$$

A series of kinematical variables have been studied in order to discriminate the two samples. These are:

- Proton angle: angle of the proton w.r.t. the neutrino beam;
- ϕ_{lH} Ang le: the angle in the transverse plane between the parent track and the hadron shower direction;
- P proton: proton momentum;

- τ scattering angle: angle of τ particle w.r.t. the neutrino beam;
- p^T_{miss}: module of the vectorial sum of the transverse momenta of primary (except the parent) and daughter with respect to the neutrino beam direction;
- P^T_{2ry}: transverse momentum at secondary vertex;
- p_{sum}: sum of the modules of all particles momenta;

and their distributions can be seen in fig. 3.23, where a green line indicate the values measured for the fifth ν_τ candidate, which are also reported in table 3.12. Distributions in fig. 3.23 are normalised to unity and weighted for the oscillation probability $\mathcal{P}_{\nu_\mu \to \nu_\tau}$, which is given by the equation 2.1.

Variable	$5^{th}\tau$ **candidate value**
τ scattering angle (rad)	0.078
Proton Angle (rad)	0.298
ϕ_{lH} Angle (degrees)	151
p^T_{miss} (GeV/c)	0.39
p_{sum} (GeV/c)	11.7
P proton (GeV/c)	1.1
P^T_{2ry} (GeV/c)	0.97

Table 3.12. Values of the variables used in the analysis for the fifth ν_τ candidate

The most discriminating variables are proton angle and ϕ_{lH}.

Correlations between these variables are expressed in the matrices in fig. 3.24. Not correlated variables are highlighted in green. The correlation between the variables used is kept low, so that every variable contributes to the BDT decision without redundancy.

The Receiver Operating Characteristic (ROC) curve is shown in fig. 3.25. It displays the background rejection versus the signal efficiency, and therefore it describes the efficiency of the BDT method. Other MVA methods, such as Neural Network, Fisher and Likelihood have been tried as well and their efficiencies are reported in the same graph. Background rejection, and thus the discrimination between the two samples, is better when the ROC curve lies in the upper right corner. It results that the best MVA method is confirmed to be BDT method [120] with Adaptive Boost, described in Appendix A.1.

The BDT response is shown in fig. 3.26. The value assumed by fifth ν_τ event are represented by green lines. In this plot, distributions are weighted for the oscillation probability and normalised to the ratio of QE/QE-like in equation 3.1.3.

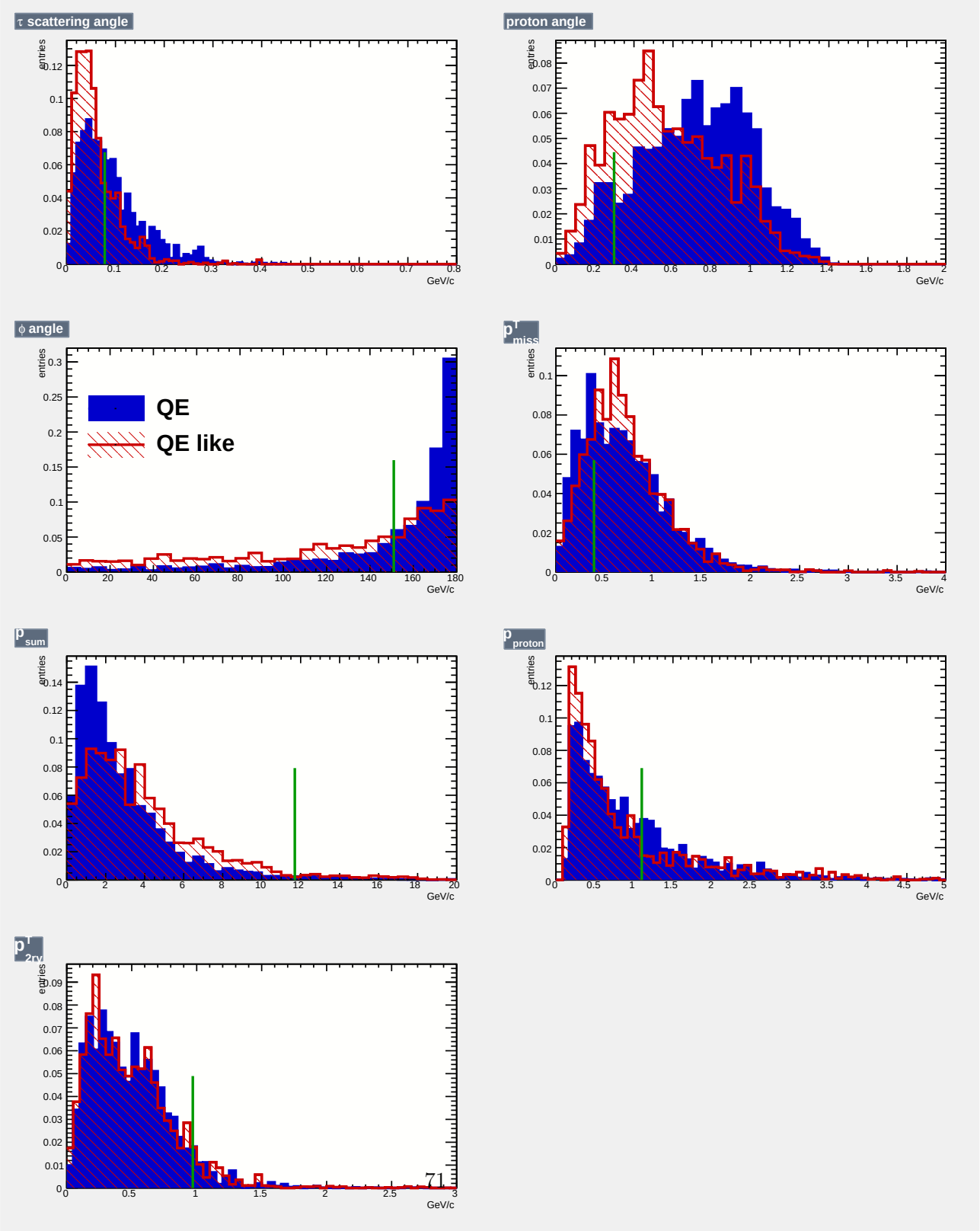

Figure 3.23. Distributions for the variables used in the analysis, normalised to unity and weighted for the oscillation probability. In blue QE, in red QE-like events

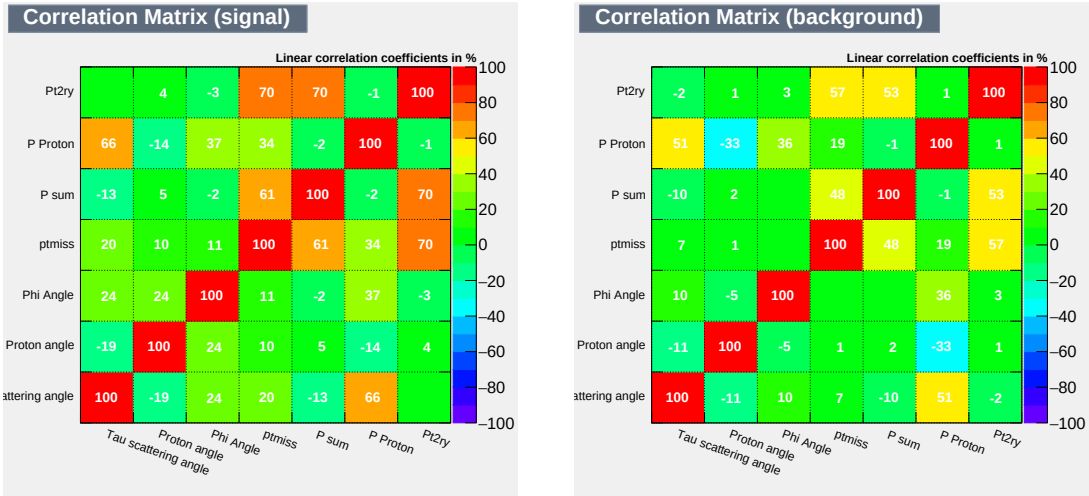

(a) (b)

Figure 3.24. Correlation between the variables used in the analysis: (a) QE events; (b) QE-like events

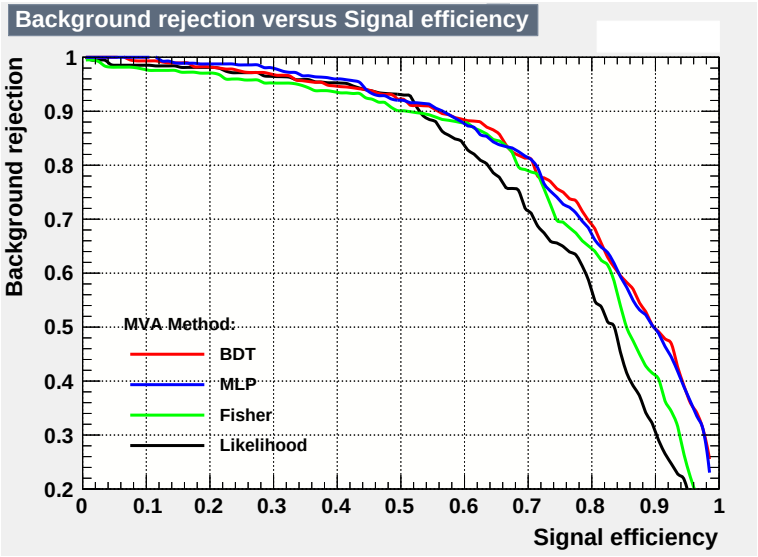

Figure 3.25. ROC curve for different MVA methods. Red: BDT with Adaptive Boost; blue: Neural Network; green: Fisher; black: Likelihood

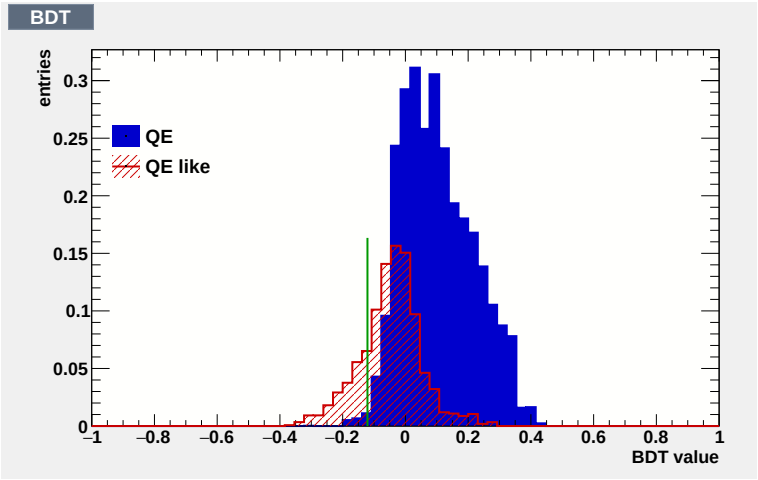

Figure 3.26. BDT results: QE MC events are in blue, while QE-like MC events in red. The green line corresponds to the fifth ν_τ event

The two distributions are partially overlapped. The green line represents the BDT value for data. The probability for the fifth ν_τ event to be QE or QE-like can be estimated through the p-value, which is defined as the probability to obtain a result equal to or larger than what was actually observed under the assumption of a certain hypothesis.

Evaluating the p-value as the fraction of events below the fifth ν_τ value, the following relation gives the probability of the event to be QE-like respect to the probability of being QE:

$$\frac{\text{p-value}_{QE-like}}{\text{p-value}_{\text{QE}}} = \frac{0.2282 \pm 0.0002}{0.008 \pm 0.009} = 27.50 \pm 0.02 \tag{3.1.6}$$

Therefore it is about 27 times more probable that the event is QE-like.

3.1.4 Significance of the observed events

Five ν_τ candidates satisfying all kinematical cuts expressed in table 3.2 have been observed in OPERA experiment: three in the $\tau \to 1h$ decay channel, one in the $\tau \to 3h$ and one in the $\tau \to \mu$ decay channel.

The significance of these candidates was evaluated as the probability that the background can produce a fluctuation larger than or equal to the observed data. Two test statistics have been adopted, using the expected signal and background events reported in table 3.3, compared with sampling distributions obtained with pseudo-experiments.

The first method was based on combining Poissonian p-values with Fisher's rule [121] into an estimator [122, 123] and gave 5.1σ. The second one is the profile likelihood ratio calculation [116], which gave compatible result. Therefore, the observation of the $\nu_\mu \to \nu_\tau$ oscillation in appearance mode was established with 5.1σ [2].

Chapter 4

New ν_τ selection strategy

Since the beginning of the experiment, stringent kinematical cuts were applied for the selection of ν_τ candidates with high purity.

After having demonstrated that ν_μ do oscillate in ν_τ [2], a new goal has been set: estimate Δm^2_{23} in appearance mode and the ν_τ cross-section (σ_{ν_τ}), so far measured only by the DONuT (Direct Observation of Nu-Tau) experiment, that however could not distinguish ν_τ from $\bar{\nu}_\tau$. The OPERA experiment, indeed, is sensitive to the product of Δm^2_{23} and σ_{ν_τ}.

To reduce the statistical error in these values estimation, a new strategy has been defined with looser kinematical cuts and a multivariate analysis.

4.1 Monte Carlo simulation

Being near to the end of the experiment, more confidence on the apparatus has been reached and all background sources are now well known. A new and enlarged Monte Carlo sample was used in this analysis: it was the result of a better description of the data and of a new neutrino event generator tuned with data.

The software framework used is called OpRelease. It is written with C++ programming language and based on ROOT classes [124, 125]. It has been conceived as a tool for both the Monte Carlo (MC) data generation and the analysis of simulated data. It is managed by the Concurrent Versions System (CVS) [126] and stored on the OPERA CVS repository at CERN. A Configuration Management Tool (CMT) [127] is used in order to set the environment variables and to create the execute files.

OpRelease consists of different software packages, which simulate the specific processes of particle propagation in the detector. The simulation chain starts with the event generator Genie [128]. Its output is converted into a ROOT file format through

the package *genie2operabeam*. The generated events are then propagated through the detector geometry defined in *OpGeom* package using the electronic detector simulation and the ECC/emulsion one. The combination of these two simulations provides the complete simulation of the detector: the electronic detector simulation is called *OpRec*, while the ECC/emulsion one is called *OpEmuRec*.

In the following, a detailed description of the simulation chain is given:

GENIE simulates all the neutrino interaction processes for the three neutrino flavours, including all nuclear effects on the target. The energy range spans from tens of MeV to the PeV energy scales. Furthermore, in the range from hundreds of MeV to a few tens of GeV, the generator tuning is extensively validated using data. As a unique feature, GENIE accounts for nuclear effects on the neutrino cross-sections. The OPERA target is made of the lead isotope mixture, i.e. 0.524% ^{208}Pb, 0.241% ^{206}Pb, 0.221% ^{207}Pb and 0.014% ^{207}Pb [129].

genie2operabeam converts GENIE output into a root file with the data format required by OpRelease packages.

OpRData describes the data format.

OpGeom, the geometry package, is based on the ROOT geometry and the class TGeoManager that defines the full geometry of all detector parts. It describes the target dimensions, positions and material features. In addition, a description of the Borexino experiment, which is also located in the hall C of the Gran Sasso underground Laboratory, just upstream of the OPERA detector, and the simulation of the surrounding rock structure are considered. Moreover, the package takes into account the changes in the detector structure due to brick extraction during the run.

OpSim reproduces the particle propagation inside the detector with the concurrent creation of track hits in the various sub-detectors. OpSim is based on the ROOT VMC package4, which allows a free choice of the transport engine for particle propagation: a generalized Monte Carlo allows the user to choose the transport generator between GEANT 3.21 and Geant4, for the whole detector, or FLUKA, only for the bricks. The output of OpSim is a ROOT file including the information about the hits left by particle propagation in the detector.

OpDigit handles the results of the particle propagation and simulates the detector response for all subdetectors. It converts the OpSim output into the data format, taking into account the electronic detectors and the emulsion response, such as attenuation of the signal amplitude due to the propagation within the cables and optical fibers, and converts the energy deposit in the RPC gas and in the emulsion, respectively to a detected electric signal at the strip end and in a track segment in

emulsions.

OpRec is the reconstruction package that handles different tasks related to the electronic detectors, such as: cross-talk removal, tagging of events on time with the beam, reconstruction of the tracks with electronic detectors, muon identification and its momentum, charge and energy measurements evaluation.

OpCarac is meant to classify the OPERA events detected and reconstructed by OpRec. It decides whether the event occurred inside the detector, in the surrounding environment or in the spectrometer, and so it classifies the events according to the following classes: CONTAINED (if the interaction vertex lies inside the OPERA target), BORDERSOFTNC (NC events without 3D track), SPECTRO (if the interaction is inside the spectrometer), SIDEMUON (if particles enter the detector from the sides, for example when the CNGS neutrino beam interacts in the surrounding rock), FRONTMUON (same as the SIDEMUON where neutrino interactions take place inside the BOREXINO detector or upstream rock and UNKNOWNTYPE if none of the above appears. Only events classified as CONTAINED and BORDERSOFTNC are analysed.

OpBrickFinding predicts the brick where the neutrino interaction occurred. It creates a probability map for each brick which may contain the interaction.

OpEmuIO simulates the tracking efficiency of the scanning system and produces the micro-tracks in the emulsion films, applying a Gaussian smearing on the micro-track positions and slopes according to the measured accuracy.

OpEmuRec simulates the reconstruction and analysis steps performed in the ECC. Some algorithms, used both for Monte Carlo and data, are meant for the event reconstruction and data analysis; other algorithms are used to simulate the location chain. Different sub-packages are responsible for CSD scanning, scan back, alignment, tracking, vertexing, decay search and scan-forth steps of the emulsion data taking.

Using the framework described, I was in charge of the production of the background sample of charmed particles decaying into muons where the muon at primary vertex is not identified, as it will be reported in section 4.3.6.

4.2 Analysis chain and event selection

The analysis chain for event selection in the OPERA experiment is a combination of electronic detectors information, emulsion analysis, topological and kinematic selections. In order to evaluate the detection efficiency, I reproduced the whole chain

using the new and final MC production, meant to include all the improvements in a much larger sample, thus reducing the systematic uncertainties. The entire chain will be explained in detail in the following:

Electronic Detector Analysis

The electronic detectors and the CERN beam are synchronized with GPS (Global Positioning System) time stamp. The data acquisition trigger selects only events on time with the beam: a coincidence is required with the two 10.5 μs wide, 50 ms separated CNGS spills. In this way background events from atmospheric neutrino interactions and cosmic muon induced rock events can be reduced.

Event trigger During the CNGS beam spill, the event building is performed by collecting all the hits in a sliding time window of 3000 ns. This is the so-called "trigger-less mode". The electronic trigger is then defined as the presence of hits in X and Y projections in at least two TT planes or a TT plane with the sum of the photomultiplier signals exceeding 1500 ADC counts, and the presence of at least 10 hits. The trigger efficiency for all the τ decay channels is larger than 98%.

Event classification Triggered events are categorized as 1μ or 0μ, according to electronic detector response. If a 3D track with length$\times$density$>$660 g/cm^2 is reconstructed or the number of TT and RPC planes having at least one hit is larger than 20, it is classified as 1μ. The complementary sample is defined as 0μ. Examples of 0μ (a) and 1μ (b) events can be seen in fig. 4.1. For 1μ events, muon momentum and charge are reconstructed through the track bending in the muon spectrometer using the sagitta method. The muon momentum is determined as the momentum of the longest 3D track. This 3D track is provided by a Kalman Filter [104]. The momentum measurement was used to define the priority sample since a large fraction ($\sim 83\%$) of muons produced in $\tau \to \mu$ decays have momentum lower than 15 GeV/c, as shown in fig. 4.2. The muon reconstruction efficiency by the electronic detectors is larger than 95%. The sign of the muon charge, instead, is important to separate signal events from charmed hadrons decaying to μ^+.

The reliability of the electronic detector simulation was studied by comparing located data with a Monte Carlo sample including ν_μ simulated interactions [104].

Event containment Subsequently, the OpRec algorithm is applied and the OpCarac classification is checked to know if the event is contained in the target. The major component of external events is classified as SIDE MUON or FRONT MUON.

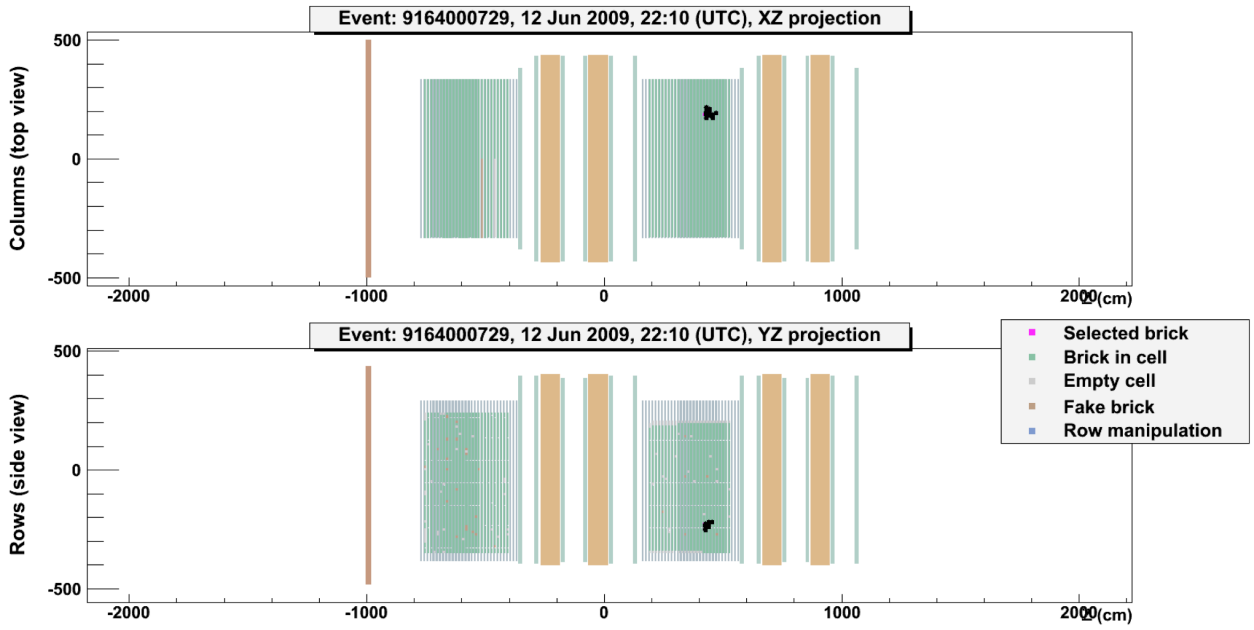

(a) An event display for 0μ event.The green zone is the target area and is followed by spectrometers, represented in brown colour. The black spots are the hits recorded in the electronic detectors. The activity in the electronic detectors is limited to a few TT planes and there is no muon track

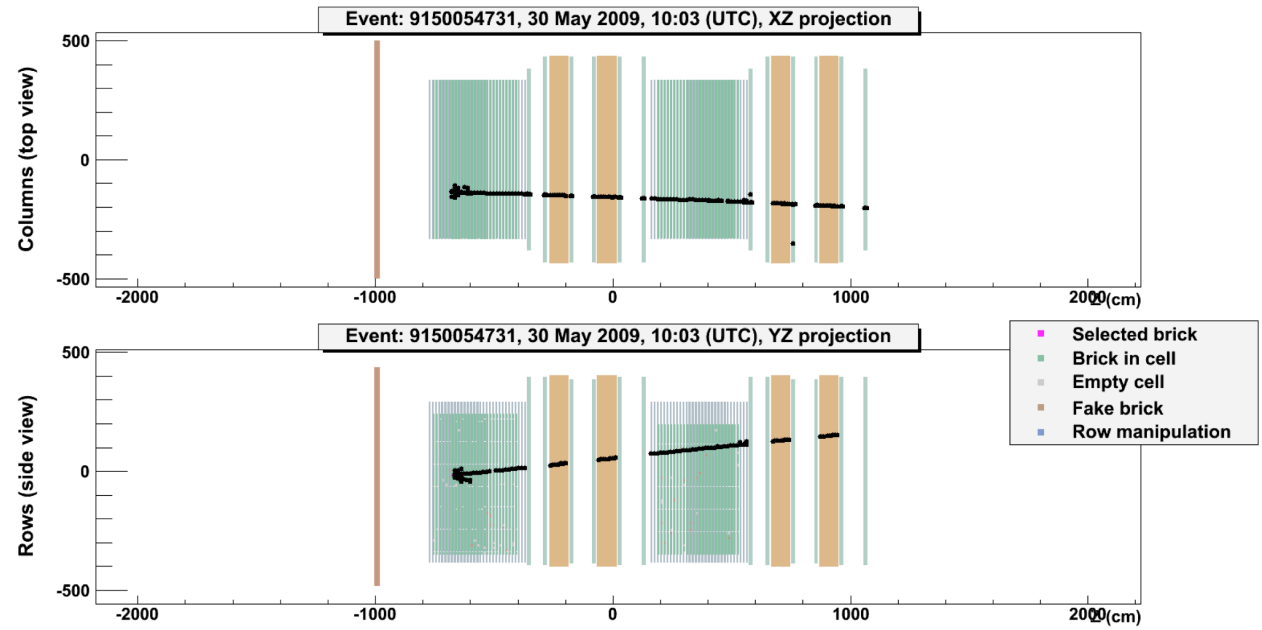

(b) An event display for 1μ event. A muon track is clearly visible, starting in the first supermodule, passing the second supermodule and exiting the detector

Figure 4.1. Event display for 0μ (a) and 1μ (b) events

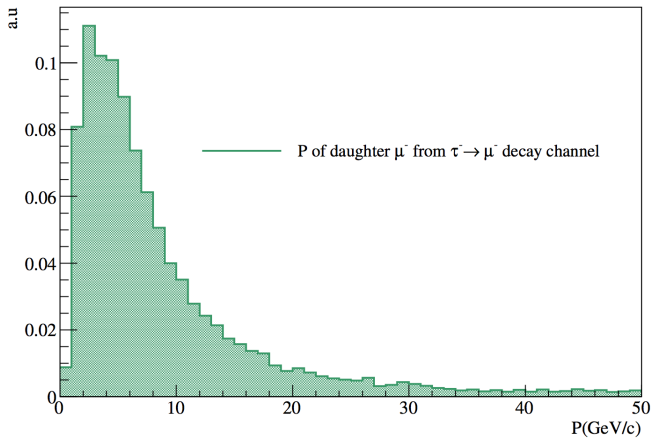

Figure 4.2. Momentum distribution of the μ^- produced in the $\tau^- \to \mu^- \bar{\nu}_\mu \nu_\tau$ decay

As mentioned before, only events marked as CONTAINED or BORDERSOFTNC are selected.

Brick finding When the trigger of the electronic detector is compatible with a neutrino interaction in the detector, the reconstruction algorithm analyses electronic detector data to build a probability map of the bricks, based on track reconstruction and energy deposit in the electronic detector, to find the bricks with higher probability to contain neutrino interactions. The most probable brick is then extracted from the detector and its CSD is analysed. If the neutrino interaction vertex is not found, the second probable brick is extracted.

OpEmuIO algorithm evaluates the probability of each brick in a cube made of $3 \times 3 \times 3$ bricks, as shown in fig. 4.3, around the neutrino interaction. Moreover, for 1μ events, prediction for the muon slope and its position in the CSD are also given, while for 0μ events the averaged centre of TT hits provides the impact point of the hadron shower on the CS. The lowest efficiencies are obtained for QE events with a single track (QE $\tau \to h$ events). The highest efficiencies are for $\tau \to \mu$ events, where the brick identification is facilitated by the presence of the muon track.

Emulsion Analysis Chain

CSD Analysis After the brick is extracted by the Brick Manipulating System, its CSD is sent to the CS scanning laboratory, in order to find the tracks corresponding to the Target Tracker hits. The CSD analysis allows to move from the centimetric accuracy of the electronic detector to the micrometric accuracy in the ECC. To connect the two CS, a first alignment is performed using the X-ray spots printed soon

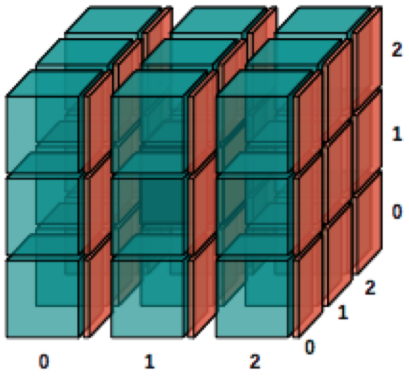

Figure 4.3. The $3 \times 3 \times 3$ matrix where the brick identification algorithm is applied. The true brick where the interaction occurred is the 111

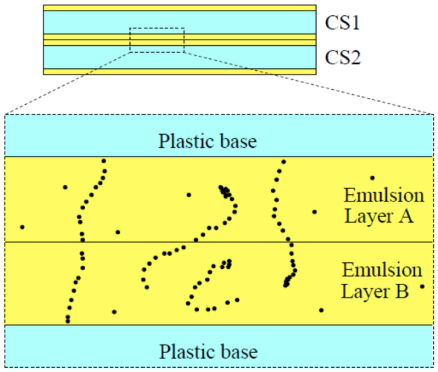

Figure 4.4. The fine alignment between the two layers is done by matching the Compton-electron tracks

after the brick extraction, while a micrometric alignment is obtained using Compton-electron tracks, originated from radioactive isotopes present in the emulsion (see fig. 4.4). The scanned area of CSD is (6×4) cm^2 around the electronic detector predictions for 1μ events and (8×6) cm^2 for 0μ ones. Tracks crossing both CS films are searched for. A coincidence of base-tracks in the two different films is called double base-track. To recover intrinsic inefficiencies affecting micro-tracks reconstruction, coincidences of a micro-track and a base-track (3/4 tracks) belonging to different films are also taken into account. Once a track crossing both CS films is found (double base-track or 3/4 track), the correspondence with tracks reconstructed by electronic detector is searched for, looking at the slope and position residual between the electronic prediction and emulsion double base tracks. A positive result consists of finding either a muon track compatible with the electronic detectors, or

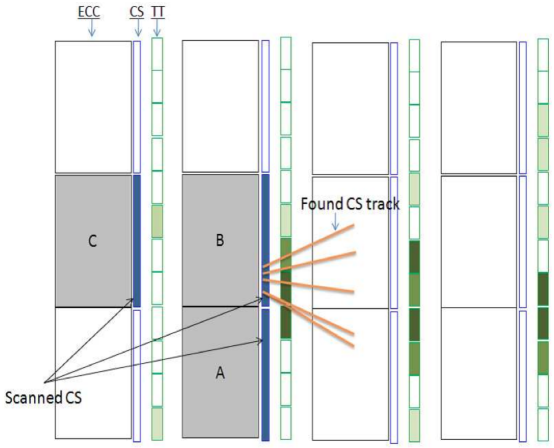

Figure 4.5. After the bricks are extracted, the CS scanning result is superimposed to a zoom of the TT display. Brick B shows a converging path and it is thus developed

an isolated 3D track consistent with the TT hits, or at least 2 converging tracks. In case of positive result, the brick is developed at LNGS laboratories and sent to one of the scanning laboratories of the Collaboration for the analysis. On the other hand, if none of the required selections is satisfied, a new CSD was attached to the ECC and it was re-inserted in the detector.

After validation, the brick is brought to surface to be exposed to high-energy cosmic rays needed for a precise film-to-film alignment. The brick is placed under a shielding structure (the cosmic pit) used to absorb soft radiations [95] for 12 hours, in order to have one penetrating track per mm^2 in the angular acceptance relevant for the scanning. The brick emulsion films are then developed with an automatic system and dispatched to the scanning laboratories.

CS to Brick Connection When a brick arrives at a scanning laboratory, tracks found on the CSD are associated with the corresponding tracks inside the brick. All CS tracks positions are projected to the most downstream film of the brick, 4500 μm upstream, then an area of about 1 mm^2 is scanned around each prediction.

All the tracks within a position tolerance of 300 μm and an angular acceptance of 60 mrad are visually checked to discard fake tracks. If a track is confirmed, it is considered connected and its position is projected to the next film to confirm the CS predictions. All candidate tracks selected will be the input of the scan-back procedure.

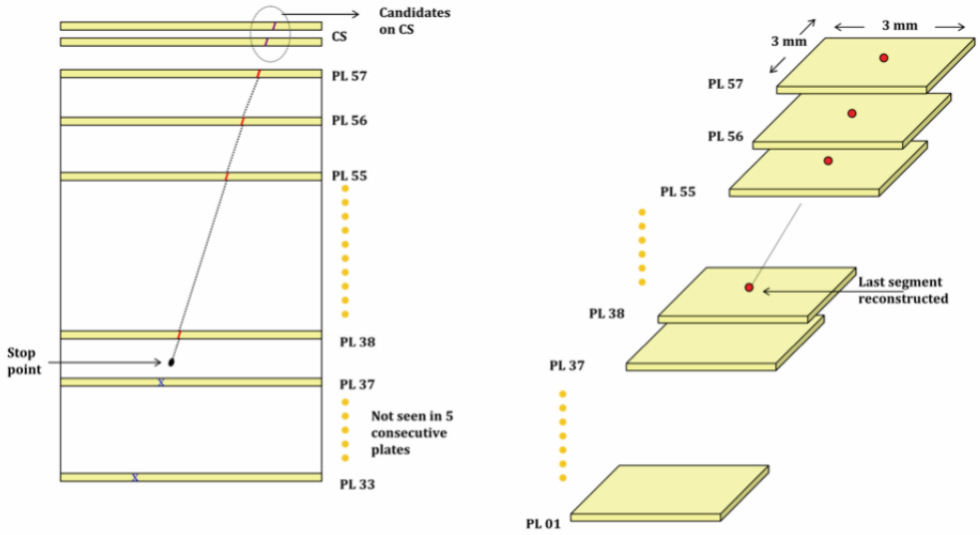

Figure 4.6. Schematic representation of the scan-back procedure. The track segments (in red) are reconstructed in the emulsion sheets (yellow). When the track disappears for 3 consecutive plates the interaction point is located

Scan-back The procedure to localize the neutrino interaction inside the brick is called *scan-back*. CS candidates connected to bricks are followed up, plate-by-plate until their disappearance. A small area (390 μm$\times$310 μm), centred at the expected position, is scanned by the microscope in order to find the predicted track. If it is found, a new prediction for the downstream plate is created by using the information of the found track. The accuracy of extrapolation from one plate to the adjacent one is around 10-20 μm. This process is iterated until no segments are found in at least 5 consecutive plates or the track exits the brick. The stopping point is then confirmed by a visual scan of the predicted area and the downstream lead plate is defined as the neutrino interaction plate (see fig. 4.6 for the schematic explanation).

The scan-back efficiency, evaluated from Monte Carlo simulation, is defined as the fraction of cases in which at least one scan-back track stops within five plates from the true primary vertex. If it exits from the most upstream plate, the track is called *passing-through* and the primary vertex will be searched for in the upstream brick, while if it exits through an edge, the primary vertex will be searched for in an adjacent brick, and the track is called *edge-out*. If one of these cases occurs, a new brick is extracted and its CSD scanned, in order to search for more tracks related to the event. The scan-back procedure is then repeated on the new brick. Neutrino interactions could occur also in the target frame or in the TT detectors, which are considered dead materials. Such events cannot be used for the neutrino oscillation

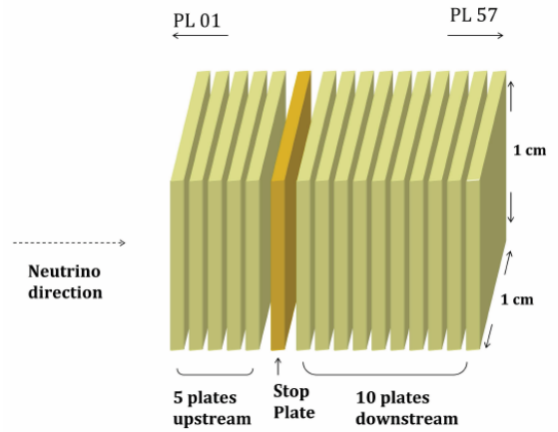

Figure 4.7. Schematic drawing of the volume scan, made of 10 plates downstream and 5 upstream of the stopping point

search, because the vertex region cannot undergo the topological analysis.

Volume scan and location Once the stopping plate has been identified, additional scanning is performed to confirm the interaction and study its topology. This procedure, called *total-scan*, consists of a volume scan performed over a 1 cm×1 cm area, centred around the predicted position of the interaction vertex, for 5 emulsion films upstream and 10 downstream with respect to the stopping point, as shown in fig. 4.7. The angular acceptance of the scanning is 0.6 rad with respect to the beam direction.

The most upstream plates act as a veto for passing through tracks, and therefore as a confirmation of the stopping point, while the ten plates downstream are meant to reconstruct the tracks produced in the neutrino interaction (and possible secondary vertices) and to classify the event as located.

The alignment between films is performed maximizing the number of high penetrating cosmic ray tracks accumulated during the dedicated exposure before the development. The alignment is done applying solid affine transformations to the emulsion film and evaluating shrinkage corrections to all the scanned films.

A dedicated software is used to reconstruct tracks and vertices. Volume tracks are reconstructed in the aligned volume with the tracking procedure, using base-tracks measured in the single emulsion layers. Only volume tracks with at least two base-tracks are considered. This track selection makes the identification of the electromagnetic showers very difficult because in this way the single base-tracks, related to the low momentum tracks, are discarded. The interaction vertex is defined

by maximizing the number of tracks attached to the vertex and by minimizing their impact parameters. This step is called *vertexing*.

The tracks used for scan-back are searched among all the reconstructed tracks. If the reconstructed scan-back track belongs to a vertex with an upstream track (*parent track*), the vertex is assumed to be a hadronic interaction and the scan-back procedure continues with the parent track. Otherwise, if the reconstructed scan-back track belongs to a vertex without a parent track, the vertex is considered the neutrino interaction vertex candidate. It could also happen that the reconstructed scan-back track does not belong to any vertex: in this case the neutrino interaction point cannot be precisely estimated.

The track information in the film immediately downstream of the vertex film is very important to improve the resolution in the determination of vertex position. Track segments in the vertex film could be missing in the reconstruction because of tracking inefficiency, therefore a visual inspection is performed looking for missing tracks. If found, they can be used to re-compute the vertex position. Electron-positron pairs coming from the conversion of photons produced in π^0 decays can be identified as couples of very-close converging segments. The presence of e^+e^- pairs can downgrade the vertex reconstruction accuracy, so they are removed for the determination of the vertex position.

All tracks having impact parameter smaller than 10 μm are attached to the primary vertex. The ones with IP$>$10 μm are candidates to be attached to a secondary vertex and have to be further studied in order to investigate whether such an anomaly could be due to their multiple scattering in the traversed lead thickness. To figure out this, a measurement of the particle momentum is performed, with the Multiple Coulomb Scattering algorithm [97]. Particles having momentum smaller than 1 GeV/c are defined as *low momentum particles* and disconnected from the vertex in order to have a more accurate determination of the vertex position. The distribution of the impact parameter of the tracks to the vertex in ν_μCC interactions is shown in fig. 4.8 both for data and simulation. More than 95% of the tracks have impact parameter smaller than 10 μm. The tail of the distribution is due to low-energy particles.

Decay Search The decay search procedure is meant to search for short lived particle decays, such as τ and charmed particles, through the different strategies that will be now described in detail:

- **Extra-track search:** tracks reconstructed in the total scan, but not associated to the primary vertex, are searched for. An extra-track is selected if the following criteria are satisfied:

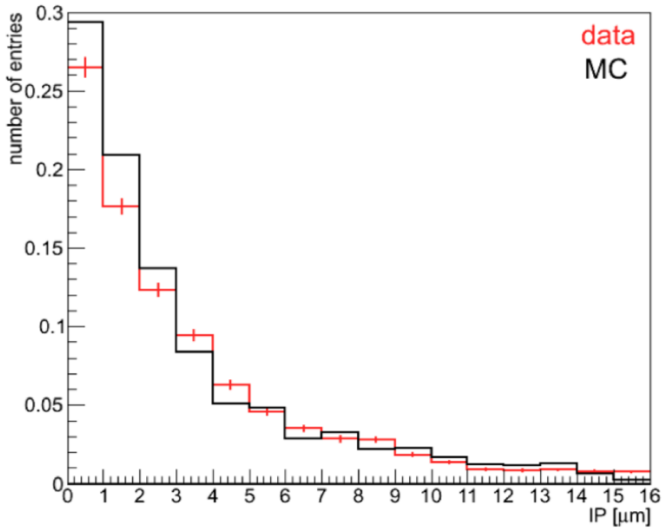

Figure 4.8. Impact parameter distribution of the primary tracks in 1μ events with respect to the reconstructed vertex, after the primary vertex definition. The distributions are normalized to unity

- the longitudinal distance z between the vertex and the most upstream segment of the track is smaller than 3.6 mm;
- the impact parameter with respect to the primary vertex is smaller than 300 μm if $z < 1$ mm, smaller than 500 μm otherwise;
- at least three segments have been reconstructed.

If the multiplicity is lower than three: extra-tracks satisfying the following criteria are also selected:

- the most upstream segment is in one of the two emulsion films upstream of the vertex;
- the impact parameter with respect to the reconstructed vertex is smaller than 500 μm.

Extra-tracks are then inspected to filter out e^+e^- pairs from γ conversion, particles not originating in the measured volume (typically, low momentum particles reconstructed as shorter tracks due to multiple Coulomb scattering) and fake tracks due to the impurity of the reconstruction program. The latter is relevant especially for bricks characterized by a high density fog. Surviving extra-tracks originating in the vertex film are analysed to check if they are low momentum tracks using the multiple scattering methods described in Section 4.2.

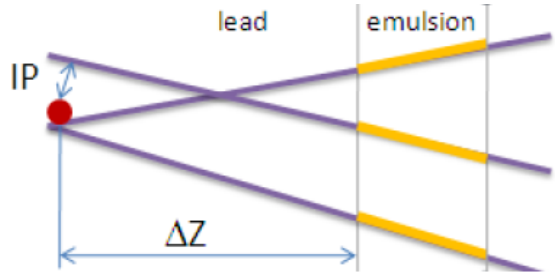

Figure 4.9. The parent search procedure consists of searching for segments connecting an extra track to the primary vertex.

- **Parent search:** a dedicated parent search procedure is applied to the extra-tracks starting downstream of the vertex film to detect long decays. A track connecting the selected extra-track to the reconstructed vertex is searched for, with the following features (see fig. 4.9):
  - impact parameter with respect to the vertex smaller than 10 μm
  - minimum distance from the daughter track smaller than 20 μm
  - kink angle, defined as the difference in slope between the parent and the daughter tracks, larger the 0.020 rad.

  Any candidate parent track selected according to these criteria is validated by visual inspection. The same procedure applies to extra-tracks originating upstream of the vertex for NC-like events.
- **In-track search:** a search for possible small kinks along the tracks attached to the primary vertex, not automatically detected in the reconstruction of total-scan data, is performed in a fiducial volume of 4 films downstream of the vertex, relevant for short-lived particle detection. This procedure is applied to all tracks for 0μ events, only to the track matching the muon prediction for 1μ events. The largest angular difference between two consecutive planes is computed in the 4 most upstream films. If it exceeds the angular resolution of the track and the kink angle is larger than 0.015 rad, it could be the hint of a τ decay.

4.3 Minimum bias selection

During the OPERA analysis, some observed events showed a τ decay topology, without satisfying the strict kinematical selection to be classified as ν_τ candidates. Aiming

at increasing the number of ν_τ candidates in order to measure Δm^2_{23} and ν_τ cross-section with reduced statistical uncertainties, I studied the optimal selection for a minimum bias analysis and I evaluated the corresponding background.

First of all, short decays were not considered for $\tau \to 1h$ and $\tau \to \mu$ decay channels, but will be included in the enlarged data sample for DIS interactions.
To define the decay topology, only the requirement $\theta_{kink} > 0.02$ rad and $z_{dec} < 2600\ \mu$m will be retained. To determine the secondary vertex position with enough precision, p_{2ry} above 1 GeV is required.
In order to reduce the background from hadron re-interactions and large angle scattering, the cut on p^T_{2ry} cannot be completely removed. The minimum threshold is set at 0.1 GeV/c.

Before reporting this study, some details about the detection efficiency estimation and the approach used to evaluate the number of expected events, Δm^2_{23} and ν_τ cross-section will be given.

4.3.1 Detection Efficiency

The τ detection efficiency is estimated by the fraction of MC events passing the different steps of the analysis chain mentioned in Section 4.2. The formula in eq. 4.3.1 is used for each decay channel.

$$\begin{aligned}\epsilon_{detection} = \epsilon_{trigger} \times \epsilon_{ED} \times \epsilon_{geometry} \times \epsilon_{BF} \times \epsilon_{CSD} \times \epsilon_{SB} \times \\ \times \epsilon_{location} \times \epsilon_{decaysearch} \times \epsilon_{kinematics} \times \epsilon_{TFD}\end{aligned} \tag{4.3.1}$$

I evaluated the efficiencies for signal and background, for all decay channels. These are reported in appendix B, step by step, and are used to evaluate the number of expected events.

4.3.2 τ signal

The number of expected τ can be defined as:

$$N^\tau_{exp} = \mathcal{M}\mathcal{N}_A P \langle\epsilon\rangle \int \Phi(E)\sigma_{\nu_\tau}(E)\mathcal{P}_{\nu_\mu \to \nu_\tau} dE \tag{4.3.2}$$

where $\mathcal{M}$ is the mass of the detector in units of kton, $\mathcal{N}_A$ is the Avogadro number, P is the value of integrated p.o.t in units of 10^{19} p.o.t, $\Phi(E)$ is the ν_μ flux in units of $\mathrm{cm}^{-2} \cdot (10^{19}\ \mathrm{p.o.t})^{-1}$ and $\langle\epsilon\rangle$ is the average location efficiency for ν_τ interactions, given by:

$$\langle\epsilon\rangle = \frac{\int \Phi(E)\sigma_{\nu_\tau}(E)\mathcal{P}_{\nu_\mu \to \nu_\tau}\epsilon(E) dE}{\int \Phi(E)\sigma_{\nu_\tau}(E)\mathcal{P}_{\nu_\mu \to \nu_\tau} dE} \tag{4.3.3}$$

Let's define $N^0_{\nu_\mu CC}$ ($N^0_{\nu_\mu NC}$) as the number of $\nu_\mu CC$ ($\nu_\mu NC$) interactions per kton and per 10^{19} p.o.t.

$$N^0_{\nu_\mu CC} = \int \Phi(E)\sigma_{\nu_\mu CC}(E)dE \qquad \left(N^0_{\nu_\mu NC} = \int \Phi(E)\sigma_{\nu_\mu NC}(E)dE\right) \tag{4.3.4}$$

The number of events localized in the 0μ channel, $N^{0\mu}_{obs}$ is given by the sum of NC events classified as 0μ, indicated as $N^{0\mu NC}_{obs}$, and CC events classified as 0μ, indicated as $N^{0\mu CC}_{obs}$:

$$\begin{aligned} N^{0\mu}_{obs} = N^{0\mu CC}_{obs} + N^{0\mu NC}_{obs} = \mathcal{M}\mathcal{N}_A P \int \Phi(E)\left(\sigma_{\nu_\mu CC}\ \epsilon^{0\mu}_{CC} + \sigma_{\nu_\mu NC}\ \epsilon^{0\mu}_{NC}\right) dE = \\ \mathcal{M}\mathcal{N}_A P\left(\langle\epsilon^{0\mu}_{CC}\rangle N^0_{\nu_\mu CC} + \langle\epsilon^{0\mu}_{NC}\rangle N^0_{\nu_\mu NC}\right) = \mathcal{M}\mathcal{N}_A P N^0_{\nu_\mu CC}\left(\langle\epsilon^{0\mu}_{CC}\rangle + \langle\alpha\rangle\langle\epsilon^{0\mu}_{NC}\rangle\right) \end{aligned} \tag{4.3.5}$$

where $\alpha = N^0_{\nu_\mu NC}/N^0_{\nu_\mu CC} \sim 0.32$

It is then possible to write the normalization factor as:

$$\mathcal{M}\mathcal{N}_A P = \frac{N^{0\mu}_{obs}}{N^0_{\nu_\mu CC}\left(\langle\epsilon^{0\mu}_{CC}\rangle + \alpha\langle\epsilon^{0\mu}_{NC}\rangle\right)} = \frac{\beta_0}{N^0_{\nu_\mu CC}} N^{0\mu}_{obs} \tag{4.3.6}$$

where $\beta_0 = \frac{1}{\left(\langle\epsilon^{0\mu}_{CC}\rangle + \alpha\langle\epsilon^{0\mu}_{NC}\rangle\right)}$ is evaluated from Monte Carlo simulations and $\langle\epsilon^{0\mu}_{CC}\rangle$ and $\langle\epsilon^{0\mu}_{NC}\rangle$ are, respectively, the average location efficiencies of $\nu_\mu CC$ and $\nu_\mu NC$ events classified as 0μ.

The number of expected τ in the 0μ sample can be written as:

$$N^\tau_{exp} = \beta_0 N^{0\mu}_{obs}\langle\epsilon\rangle\frac{N^0_\tau}{N^0_{\nu_\mu CC}} \tag{4.3.7}$$

where N^0_τ is the number of ν_τ interactions per kton and per 10^{19} p.o.t.
The number of expected τ in a certain decay channel $\tau \to i$, being $i = h,\ 3h,\ e$ is then:

$$N^{\tau\to i(0\mu)}_{exp} = \beta_0 N^{0\mu}_{obs}\langle\epsilon_{\tau\to i}\rangle\frac{N^0_\tau}{N^0_{\nu_\mu CC}} Br(\tau \to i) \tag{4.3.8}$$

where $\langle\epsilon_{\tau\to i}\rangle$ is the average efficiency for that decay channel.
Similarly, the number of expected τ in the decay channel $\tau \to \mu$ is:

$$N^{\tau\to\mu(1\mu)}_{exp} = \beta_1 N^{1\mu}_{obs}\langle\epsilon_{\tau\to\mu}\rangle\frac{N^0_\tau}{N^0_{\nu_\mu CC}} Br(\tau \to \mu) \tag{4.3.9}$$

where $\beta_1 = \frac{1}{\left(\langle\epsilon^{1\mu}_{CC}\rangle + \alpha\langle\epsilon^{1\mu}_{NC}\rangle\right)}$ is evaluated from Monte Carlo simulations and $\langle\epsilon^{1\mu}_{CC}\rangle$ and $\langle\epsilon^{1\mu}_{NC}\rangle$ are, respectively, the average location efficiencies for $\nu_\mu CC$ and $\nu_\mu NC$ events classified as 1μ.

4.3.3 Δm^2_{23} estimation

Δm^2_{23} can be estimated from the number of observed events. Being $\sin^2\theta_{23} = 0.437^{+0.179}_{-0.058}$ for Normal Hierarchy and $\sin^2\theta_{23} = 0.569^{+0.068}_{-0.186}$ for the inverted one [109], maximal mixing $\sin^2 2\theta_{23} = 1$ is assumed. The number of observed ν_τ can be written as:

$$N_{\nu_\tau} = f(\Delta m^2) = \int \Phi(E)\sigma_{\nu_\tau}(E)\epsilon(E)\mathcal{P}_{\nu_\mu\to\nu_\tau}(E)dE \tag{4.3.10}$$

where $\Phi(E)$ is the muon neutrino flux, $\sigma_{\nu_\tau}(E)$ is the ν_τ cross-section, $\epsilon(E)$ is the ν_τ detection efficiency and E is the neutrino energy.
Since, assuming $\sin^2 2\theta_{23} = 1$, the oscillation probability $\mathcal{P}_{\nu_\mu\to\nu_\tau}$ becomes $\left(\frac{\Delta m^2_{23}\cdot L}{E}\right)^2$, equation 4.3.3 becomes:

$$N_{\nu_\tau} = f(\Delta m^2) = (\Delta m^2_{23})^2 L^2 \int \Phi(E)\frac{\sigma_{\nu_\tau}(E)}{E^2}\epsilon(E)dE \tag{4.3.11}$$

The Δm^2_{23} range has been evaluated using Feldman-Cousins method [130], which is a classical frequentist calculation based on the Neyman Construction [131]. Feldman-Cousins method was conceived to avoid unphysical confidence intervals, giving the correct coverage, while other classical techniques may fail in neutrino oscillation search experiments, where the confidence region can have a particularly complicated structure due to physical constraints.

4.3.4 ν_τ cross-section estimation

The Deep-Inelastic (DIS) CC cross-section per nucleon can be defined as:

$$\sigma^{DIS}_{\nu_\tau} = \sigma^0_{\nu_l} E K(E), \quad l = e, \mu, \tau \tag{4.3.12}$$

where $\sigma^0_{\nu_l}$ is the energy-independent factor of the cross-section of flavour l and $K(E)$ is a kinematic suppression factor. Unlike electron and muon neutrinos, tau neutrino charged-current interactions produce the τ lepton with a non-negligible mass, which turns into a kinematical suppression factor. If we considered the muon cross-section, instead, we would have $\sigma^{DIS}_{\nu_\mu} = \sigma^0_{\nu_l} E$. Assuming the lepton universality, $\sigma^0_{\nu_l}$ is the same for the three leptons.

The number of ν_τ expected events includes also quasi-elastic (QE) and resonant (RES) interactions, that cannot be distinguished on an event by event basis from the DIS interactions. We have therefore to sum up the contributions from the different processes.

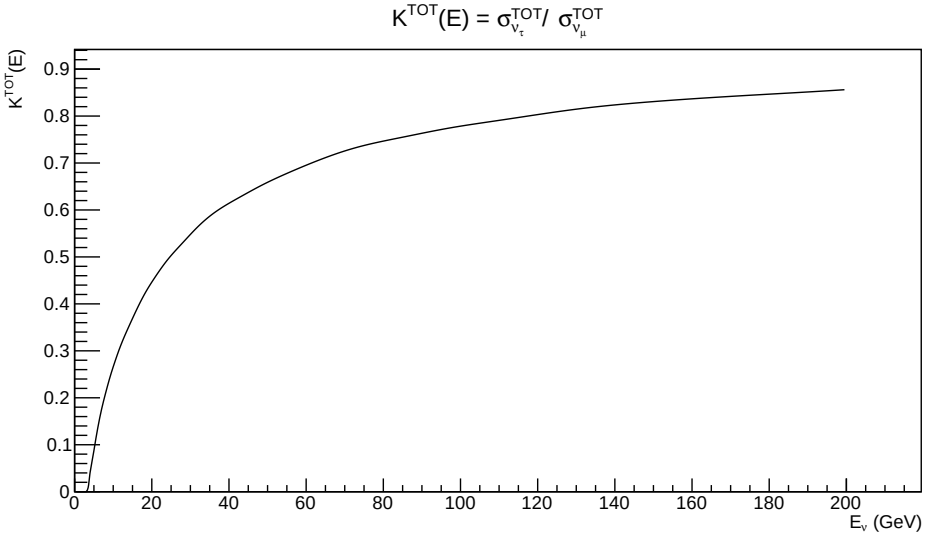

Figure 4.10. The kinematic suppression factor $K^{TOT}(E)$, defined in eq. 4.3.14

The total cross-section per nucleon will be given by:

$$\begin{aligned}\sigma^{TOT}_{\nu_\tau} = \sigma^{DIS}_{\nu_\tau} + \sigma^{QE}_{\nu_\tau} + \sigma^{RES}_{\nu_\tau} = \sigma^0_{\nu_l} E K(E) + \sigma^{QE}_{\nu_\tau} + \sigma^{RES}_{\nu_\tau} = \\ = \sigma^0_{\nu_l} E \left(K(E) + \frac{\sigma^{QE}_{\nu_\tau} + \sigma^{RES}_{\nu_\tau}}{\sigma^0_{\nu_l} E} \right) = \sigma^0_{\nu_l} E K'(E)\end{aligned} \tag{4.3.13}$$

Given the expressions of the total ν_τ and ν_μ cross sections used in Genie, it is possible to evaluate the term:

$$K^{TOT}(E) = \frac{\sigma^{TOT}_{\nu_\tau}}{\sigma^{TOT}_{\nu_\mu}} = \frac{\sigma^0_{\nu_l} E K'(E)}{\sigma^0_{\nu_l} E + (\sigma^{QE}_{\nu_\mu} + \sigma^{RES}_{\nu_\mu})} = \frac{K'(E)}{1 + \frac{\sigma^{QE}_{\nu_\mu} + \sigma^{RES}_{\nu_\mu}}{\sigma^0_{\nu_l} E}} \tag{4.3.14}$$

which is plotted in fig. 4.10.

The measured factor $K'(E)$, therefore, will be given by:

$$K'(E) = K^{TOT}(E) \cdot \left(1 + \frac{\sigma^{QE}_{\nu_\mu} + \sigma^{RES}_{\nu_\mu}}{\sigma^0_{\nu_l} E} \right) \tag{4.3.15}$$

and it is shown in fig. 4.11

The ratio $K'(E)/K^{TOT}(E)$ is shown in fig. 4.12 and is roughly equal to 1, except at below 15 GeV, where, as expected, QE interactions dominate.

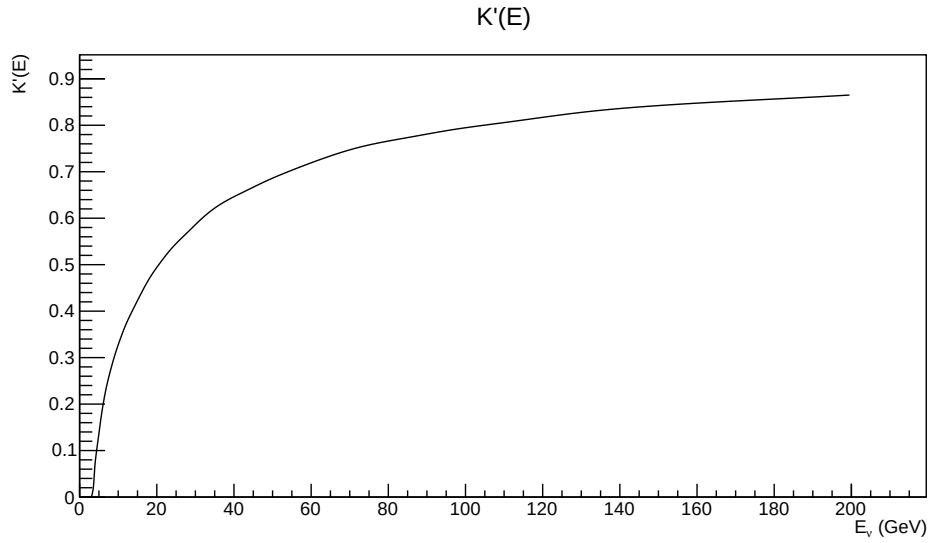

Figure 4.11. The kinematic suppression factor $K'(E)$, defined in eq. 4.3.15

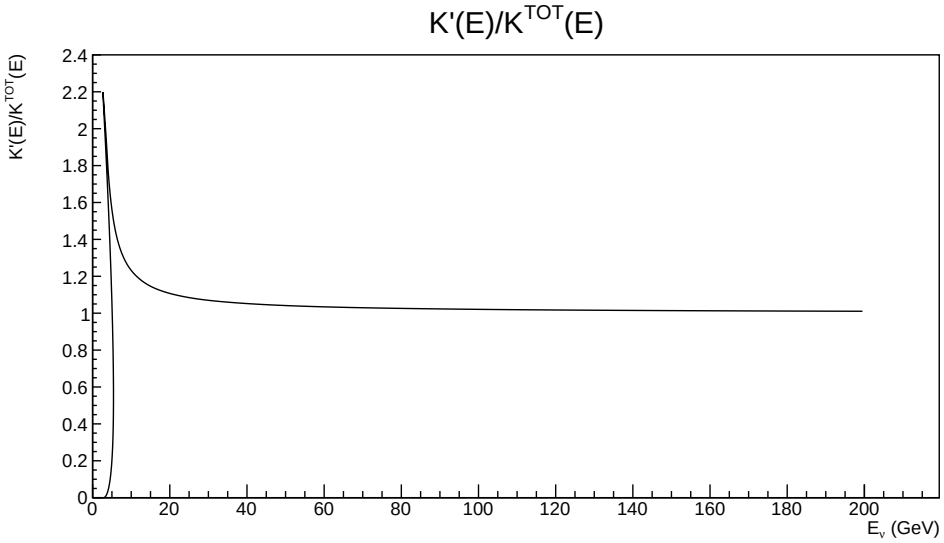

Figure 4.12. The ratio $K'(E)/K^{TOT}(E)$ is roughly equal to 1, except at low energies

The ν_τ cross section is related to the number of ν_τ as defined in eq. 4.3.2. Therefore, to measure the term $\sigma^0_{\nu_\tau}$, the number of expected and observed events can be compared:

$$\sigma^0_{\nu_\tau\ meas} = \frac{N^{obs}_{\nu_\tau} - N^{exp}_{bkg}}{N^{exp}_{\nu_\tau}} \sigma^0_{\nu_l\ SM} \tag{4.3.16}$$

4.3.5 Hadron re-interactions

In the hadronic τ decay channels, a source of background is due to re-interactions in the lead of hadrons produced in ν_μNC and in ν_μCC interactions where the primary muon is not identified.

Since positively charged pions beams are contaminated by protons, only negatively charged pion have been selected for the comparison of data and simulation. Results are valid for both π^+ and π^-. $3 \cdot 10^6$ events were simulated using Fluka, with π^- in an energy range going from 1 to 15 GeV impinged on 1 mm of lead. The validity of the Fluka description of the hadron interactions was checked by an OPERA brick test exposures at 2, 4 and 10 GeV/c π^- beam. Good agreement was found between the data and the simulation for both shape and absolute values [132].

This background source is subdominant for trident events, while it becomes significant for single prong events, since the majority of hadron re-interactions have only one prong, as it can be seen in figures 4.13.

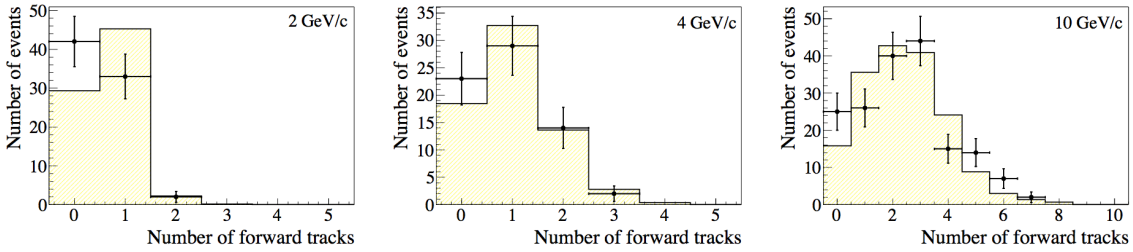

Figure 4.13. Multiplicity distributions of relativistic particle tracks in the forward hemisphere for experimental data (dots with error bars) and simulated data (histogram). The simulated distributions are normalized to the real data [132]

The p^T_{2ry} distribution for 1-prong events is characterised by an exponential behaviour, as shown in fig. 4.14. For this reason, in the kinematical criteria reported in table 3.2, a strong cut was applied on this variable for the $\tau \to 1h$ decay channel: 0.3 GeV/c in the presence of γ particles associated to the decay vertex, which is a signature of τ decaying into ρ, 0.6 GeV/c otherwise. Thanks to this cut, the number of expected events from hadron re-interaction background was: 0.022 ± 0.006 over

0.52 ν_τ candidates expected. Removing the cut on p^T_{2ry} would lead to an unaffordable large increase of this background source, therefore only events with $p^T_{2ry} > 0.1$ GeV/c will be studied.

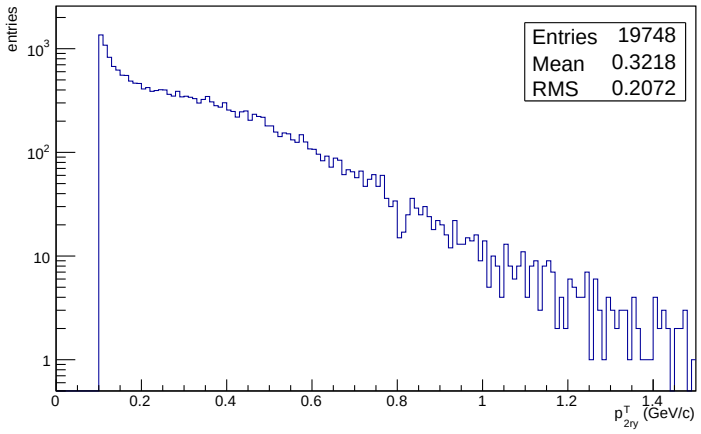

Figure 4.14. Distribution of p^T_{2ry} for 1-prong hadron re-interaction background

In table 4.1, the increase factor, evaluated as $N_{bkg_{\text{NEW CUT}}}/N_{bkg_{\text{STANDARD}}}$ and the number of expected events from this background source are calculated for different p^T_{2ry} cuts.

p^T_{2ry} **cut** (GeV/c)	**Increase Factor**	**Background events**
0.10	71	1.61
0.15	54	1.24
0.20	45	1.03
0.25	38	0.87
0.30	31	0.72

Table 4.1. Number of expected events for 1-prong hadron re-interaction background at different p^T_{2ry} cuts

Since the aim of the minimum bias selection is to estimate the product of Δm^2_{23} and ν_τ cross-section with reduced statistical uncertainty, I carried out a dedicated study to optimise this cut so that the product of their C.L. intervals was minimized.

10k pseudo-experiments were generated. For each experiment the number of signal and background expected events was generated normally distributed around

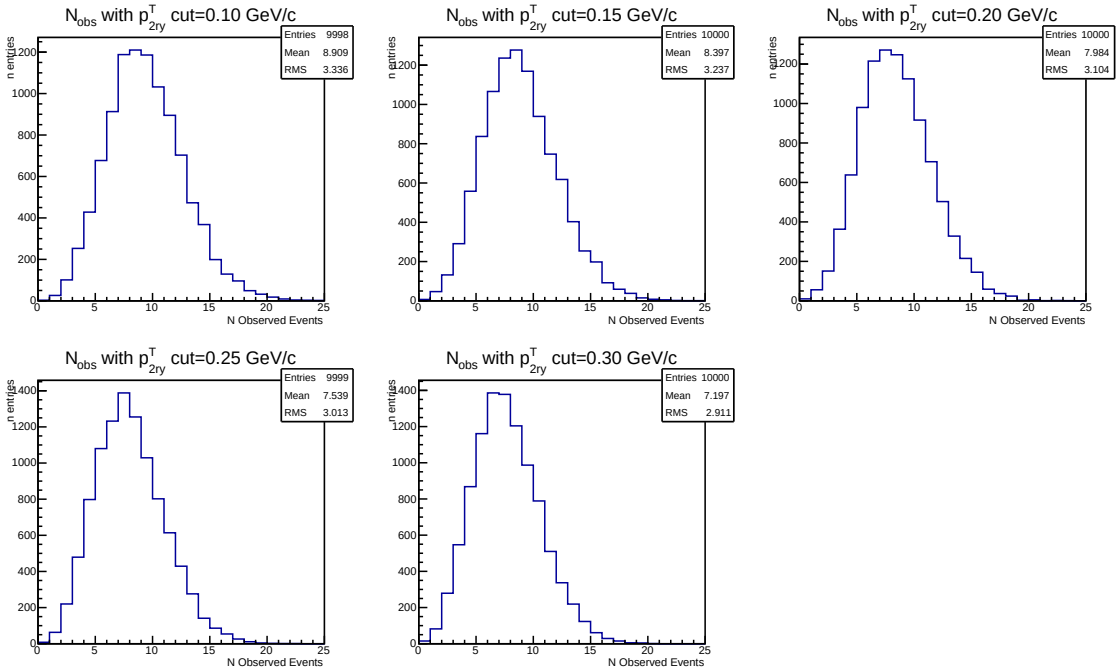

Figure 4.15. Number of observed ν_τ events for 10k pseudo-experiments

the central value, with variance equal to the total systematic uncertainty, using the values reported in table 4.1. The number of observed events, instead, was generated according to the Poisson distribution centred on the number of expected events, given by the sum of signal and background expected events. The resulting distributions are shown in figure 4.15.

For each pseudo-experiment, the 90% C.L. range for Δm^2_{23} ($R_{\Delta m^2_{23}}$) and σ_{ν_τ} ($R_{\sigma_{\nu_\tau}}$) were evaluated using Feldman-Cousins method [130]. The product of the mean of $R_{\Delta m^2_{23}}$ and the mean of $R_{\sigma_{\nu_\tau}}$ for every p^T_{2ry} cut is shown in fig. 4.16, while in table 4.2 the mean for $R_{\Delta m^2_{23}}$ and $R_{\sigma_{\nu_\tau}}$ are reported separately.

The cut for which the product of $R_{\Delta m^2_{23}}$ and $R_{\sigma_{\nu_\tau}}$ is minimised is 0.15 GeV/c, therefore for the $\tau \to 1h$ decay channel this cut will be applied, whereas for the leptonic decay channels, where this source of background is not so relevant, it is kept at 0.1 GeV/c. For $\tau \to 3h$ decay channel, instead, p^T_{2ry} is not evaluated.

4.3.6 Charm background

For $\tau \to 1h$ and $\tau \to 3h$ decay channels, background coming from charmed hadrons is made up of events where the primary muon is not identified and are, consequently,

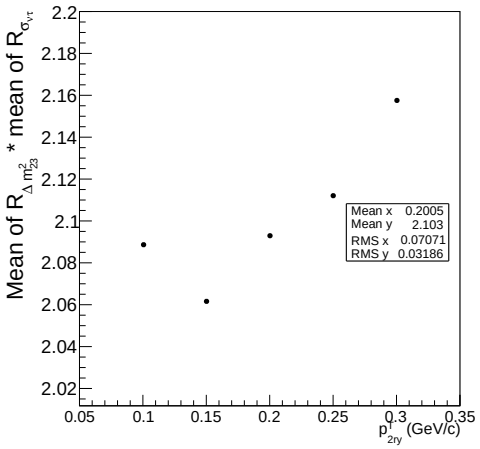

Figure 4.16. Product of the mean of $R_{\Delta}m^2_{23}$ and the mean of $R_{\sigma_{\nu_\tau}}$

p^T_{2ry} cut (GeV/c)	Mean of $R_{\Delta m^2_{23}}$ (10^{-3} eV^2)	Mean of $R_{\sigma_{\nu_\tau}}$ (10^{-38} cm^{2}GeV^{-1})
0.1	2.041	1.036
0.15	2.017	1.034
0.2	2.034	1.041
0.25	2.040	1.046
0.3	2.051	1.061

Table 4.2. Mean of $R_{\Delta m^2_{23}}$ and mean of $R_{\sigma_{\nu_\tau}}$ for different p^T_{2ry} cuts

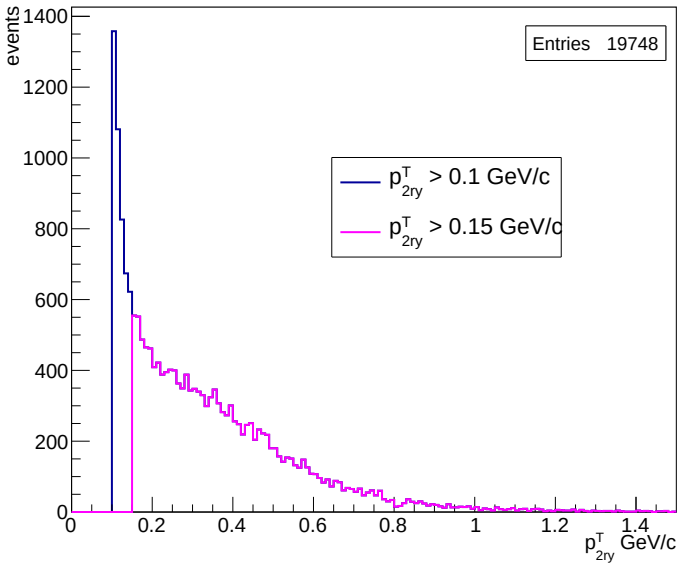

Figure 4.17. Distribution of p^T_{2ry} for 1-prong hadron re-interaction before (black line) and after (magenta line) the cut

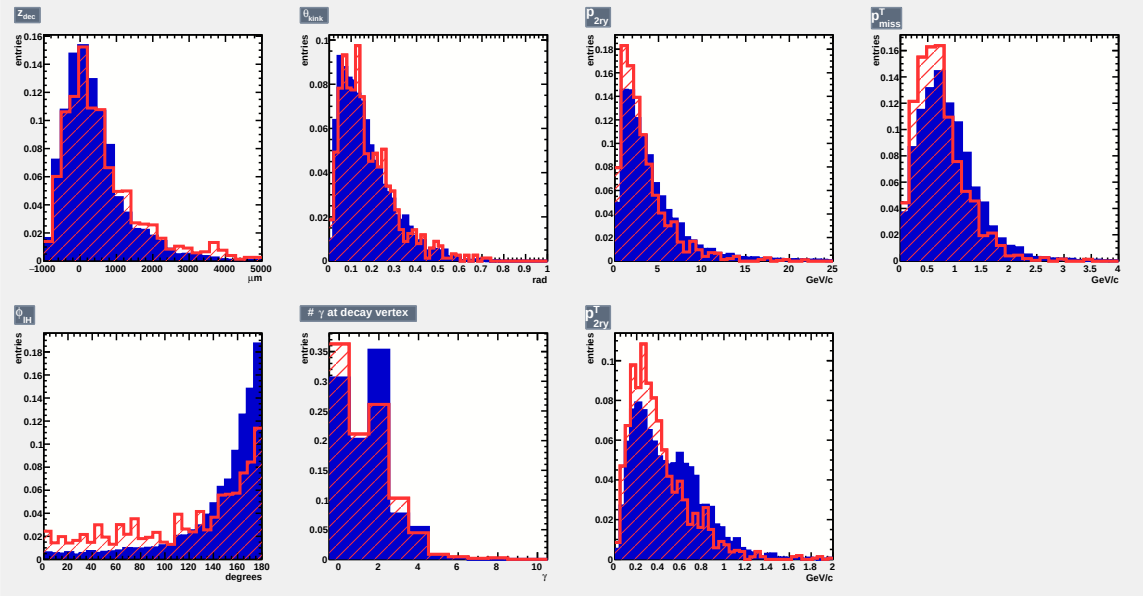

Figure 4.18. Kinematical variables for $\tau \to 1h$ (blue) and background from $charm \to 1h$ (red) normalised to unity

classified as 0μ by the electronic detectors. The selection criteria defined for 0μ events are therefore applied. The muon identification, amounting to 97% after the application of the track follow down, suppresses this background.

Since the muon at the primary vertex is not identified, the decay of τ and charm in either one or three hadronic prongs share similar behaviour. The kinematical variables used in the analysis that lead to the ν_τ appearance claim are reported in figures 4.18 and 4.19. The kinematics of charm hadron decays is very similar to τ one and the distributions of their kinematical variables are almost always overlapped, except for ϕ_{lH} angle. For this reason it is difficult to further reduce charm background contribution.

For the electronic decay channel, charm decaying into electron is the only background source. Kinematical variables are shown in figure 4.20.

The number of expected background charm events in the $\tau \to i \quad (i = h,\, 3h,\, e)$ decay channel is given by:

$$N_{exp}^{C\to i(0\mu)} = f_{C^+} Br(C \to i) \beta_0 N_{obs}^{0\mu} \langle \epsilon_{C\to i} \rangle \langle \frac{\sigma_{charm}}{\sigma_{\nu_\mu CC}} \rangle \tag{4.3.17}$$

where f_{C^+} is the fraction of positive charged charmed hadrons, amounting to 56%, and $Br(C \to i)$ are the charged charm hadronization fractions in the different decay

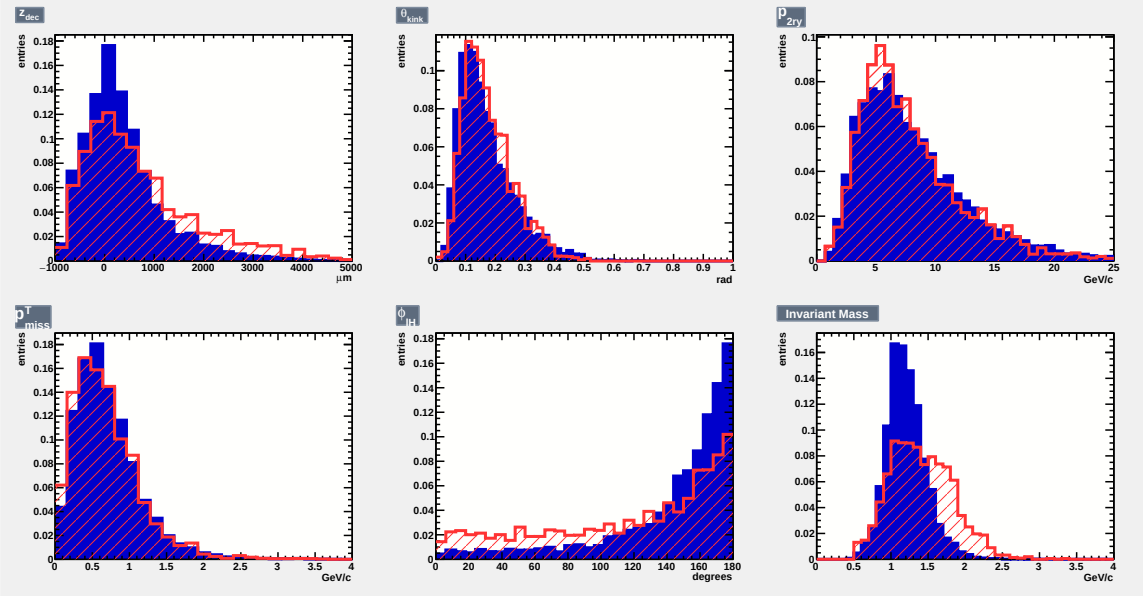

Figure 4.19. Kinematical variables for $\tau \to 3h$ (blue) and background from *charm* $\to 3h$ (red) normalised to unity

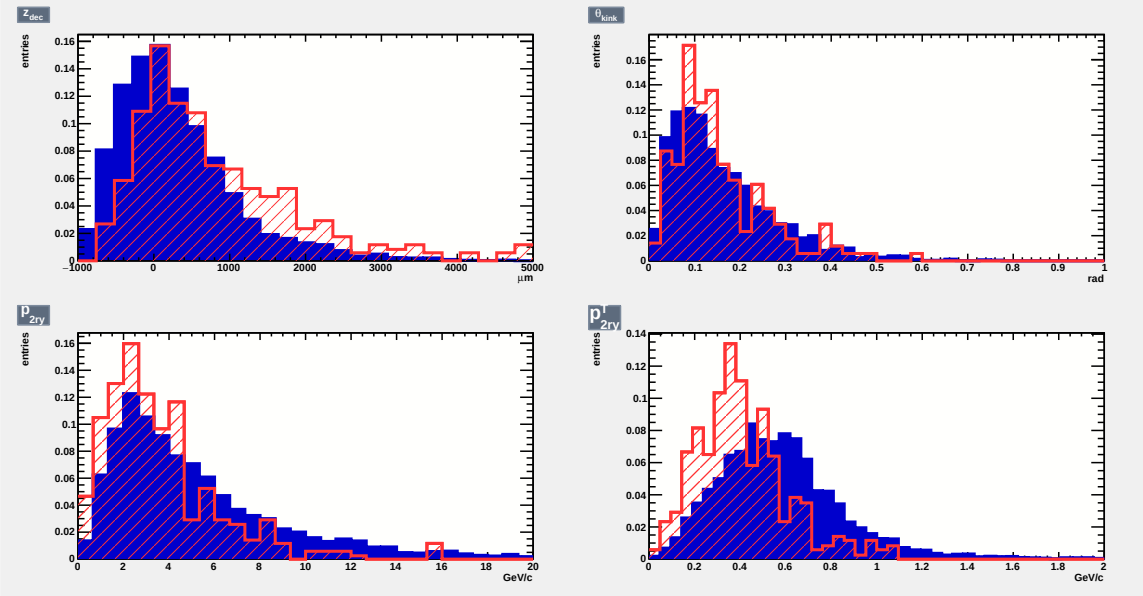

Figure 4.20. Kinematical variables for $\tau \to e$ (blue) and background from *charm* $\to e$ (red) normalised to unity

topologies, as reported in table 2.4.

The charm background in the $\tau \to \mu$ is made up by muon decay of charmed particles. The kinematical variables for the muonic decay channel are reported in figure 4.21 and compared to signal.

The charm background in this channel is largely suppressed by the following additional requirements:

- **μ-matching:** only one muon track is reconstructed by the electronic detectors and it is in agreement within 60 mrad with the slopes of the decay daughter.
- **μ-charge:** the daughter track is measured with a negative or not measured charge: the τ daughter, indeed, has always negative charge, on the contrary, charged charmed particles have a positive charge.

Moreover, *charm* $\to \mu$ background is suppressed by the small branching ratio of charm in a single muon.

The number of expected background from charm in the $\tau \to \mu$ decay channel is:

$$N_{exp}^{C \to i(1\mu)} = f_{C^+} + Br(C \to \mu)\beta_1 N_{obs}^{1\mu} \langle \epsilon_{C \to \mu} \rangle \langle \frac{\sigma_{charm}}{\sigma_{\nu_\mu CC}} \rangle \tag{4.3.18}$$

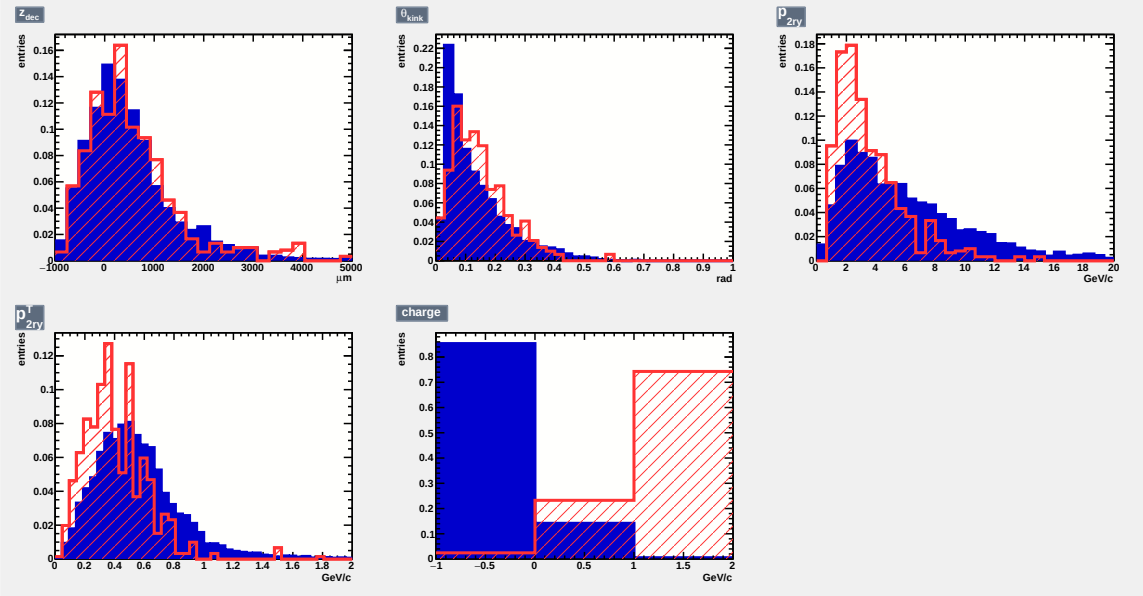

Figure 4.21. Kinematical variables for $\tau \to \mu$ (blue) and background from *charm* $\to \mu$ (red) normalised to unity

In order to study charm background in this highly pure muonic decay channel, I produced a MC sample with preselected events without any muon identified at primary vertex and with a single daughter track defined as a muon. A muon is not identified if one of the following cases occurs:

- track slopes ≥ 1 rad (2.8% of cases);
- $P_\mu \leq 100$ MeV (0.1% of cases);
- $D_{TFD} \leq 0.8$ and the track length $\times$ the density of crossed material ≤ 660 g/cm^3 (3.3% of cases).

On a sample of 926868 MC neutrino interactions with a charmed particle decaying into muon, only in $\sim 6.1\%$ of cases the muon at primary vertex satisfied at least one of the previous conditions, so a specific strategy was developed in order to make the production possible in terms of CPU time and disk quota.

The longest time and disk space in the production chain is needed for the creation of emulsion hits. For this reason, events were only processed up to OpRec, so that they were randomly located in the detector and ED hits were produced, allowing to perform Track Follow Down. No emulsion hits were produced at this time. After selecting background events, these were processed again up to the whole chain, using the same random seed in order to place the event in the same position.

4.3.7 Muon large angle scattering

Large angle scattering (LAS) of muons is a background source for $\tau \rightarrow \mu$ decay channel. Simulation for LAS was performed using the GEANT4 package. About 1.1 billion incident μ^- were generated with a flat momentum distribution between 1 and 15 GeV/c, with orthogonal incidence on the lead-film double cell. The simulation exploited a dedicated treatment of the form factors tuned for the description of the available data. Results for θ_{kink} and p^T_{2ry} were validated thanks to a detailed comparison with experimental data from the literature [133].

The probability of a LAS event in the signal region over 2 mm of lead with the standard cut ($\theta_{kink} > 0.02$ rad and $p^T_{2ry} > 250$ MeV/c) was found to be: $f^{Pb}_{LAS} = (1.2 \pm 0.1(stat.)) \times 10^{-7}/\nu^{CC}_\mu$, for an expected background of 0.0002 ± 0.0001 events.

A plot showing p^T_{2ry} distributions for LAS and comparing the old selection with the minimum bias one is shown in figure 4.22. Lowering the p^T_{2ry} cut at 0.1 GeV/c, the number of expected events from LAS background becomes 0.016 ± 0.008, 80 times larger than before.

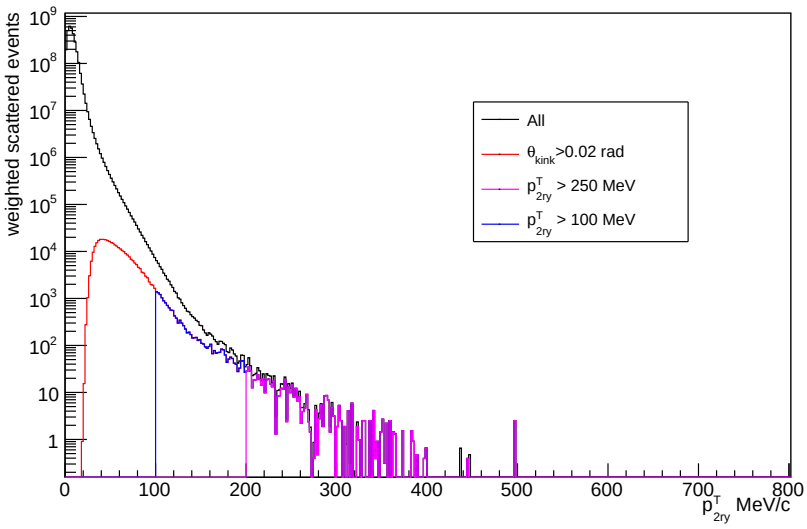

Figure 4.22. Distribution of p^T_{2ry} for the LAS background before cuts (black), after the angular cut (red) $\theta_{kink} > 0.020$ rad and after the angular and $p^T_{2ry} > 250$ MeV/c (magenta) or $p^T_{2ry} > 100$ MeV/c (blue) cuts

4.3.8 π and K decays

Since p^T_{2ry} cut is below 250 MeV/c, π and K decays within 2600 μm have been studied for this analysis.

Using a Monte Carlo (MC) sample of ν_μ^{NC} interactions, I evaluated the average number of pions and kaons per neutrino interaction vertex. This results to be 2.6 for π and 0.18 for K. The MC momenta distributions for π and K attached to the neutrino vertex are shown in fig. 4.23. Mean momentum is about 2.8 GeV for pions and 5 GeV for kaons.

The average flight length is given by:

$$\beta\gamma c\tau = \frac{P}{m} c\tau \tag{4.3.19}$$

A track is recognised in emulsion if its momentum is larger than 100 MeV, so the flight length for a 100 MeV momentum pion (eq. 4.3.20a) and kaon (eq. 4.3.20b) can be evaluated:

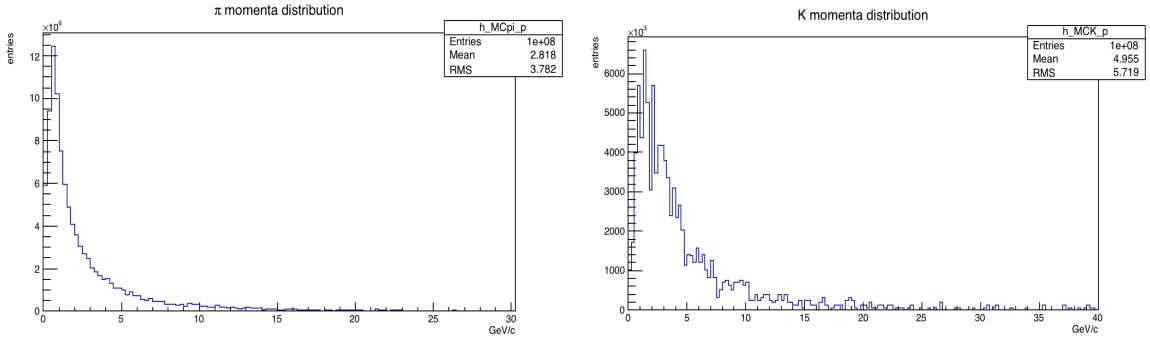

Figure 4.23. Momentum distributions for pions (left) and kaons (right) attached to the neutrino interaction vertex

$$Minimum\ Flight\ length_{\pi} = \frac{100\,MeV}{139.6\,MeV} \cdot c \cdot 1.2380 \cdot 10^{-8}\,s = 0.75\,m \qquad (4.3.20a)$$

$$Minimum\ Flight\ length_{K} = \frac{100\,MeV}{493.7\,MeV} \cdot c \cdot 2.6033 \cdot 10^{-8}\,s = 5.6\,m \qquad (4.3.20b)$$

In both cases, their minimum flight length is much larger than the cut of 0.26 cm, therefore it can be concluded that background coming from pions and kaons decay is still negligible when loosing kinematical cuts.

4.4 The Minimum bias selection

Given the studies described in the previous section, the minimum bias selection was defined and the corresponding cuts are summarised in table 4.3. The standard kinematical cuts (OLD in the table) are also reported. The new cuts are the same for all decay channels, except from p^T_{2ry} cut, which applies only to 1-prong decays. For this variable, a dedicated study was performed for $\tau \to 1h$ decays due to the outstanding increase of hadron re-interaction background, obtaining that the best cut in this decay channel is at 0.15 GeV/c. Short decays are now included for DIS interactions, but for them at least one primary track with momentum larger than 1 GeV/c satisfying IP requirement is required in order to estimate the vertex position with enough precision.

Using the minimum bias criteria, the signal to noise ratio is reduced, but replacing the cut based analysis with a multivariate technique, such as the Boosted Decision Tree analysis, it is possible to classify the events with improved purity, as it will be described in Chapter 5.

Variable	$\tau \to 1h$		$\tau \to 3h$		$\tau \to \mu$		$\tau \to e$	
	OLD	NEW	OLD	NEW	OLD	NEW	OLD	NEW
z_{dec} (μm)	$[44, 2600]$	<2600	<2600		$[44, 2600]$	<2600	<2600	
θ_{kink} (rad)	>0.02		<0.5	>0.02	>0.02		>0.02	
p_{2ry} (GeV/c)	>2	>1	>3	>1	$[1, 15]$		$[1, 15]$	>1
p^T_{2ry} (GeV/c)	$>0.6\,(0.3)$	>0.15	/		>0.25	>0.1	>0.1	
p^T_{miss} (GeV/c)	$< 1\star$	/	$< 1\star$	/	/		/	
ϕ_{lH} (rad)	$>\pi/2\star$	/	$>\pi/2\star$	/	/		/	
m, m_{min} (GeV/c^2)	/		$[0.5, 2]$	/	/		/	

Table 4.3. Minimum bias selection criteria (NEW) compared with the standard kinematical selection (OLD). The meaning of the variables has been defined in section 3.1.1.

4.5 Migration between decay channels

When analysing a ν_τ interaction in the OPERA ECC, it could happen that the τ decay topology is correctly recognised by the decay search procedure, but its decay channel is misclassified. For example, an electron not showing any shower inside the brick could be classified as a hadron, or a hadron as a muon and vice versa. This rare possibility was not taken into account in the previous efficiencies evaluation, because the effect was negligible.

Now, applying the minimum bias selection, which is almost identical for all decay channels, this contribution is still small, but worth to be evaluated and leads to an increase of efficiencies. For example, if a true $\tau \to 1h$ is misclassified as $\tau \to \mu$ this will increase the efficiency of the $\tau \to \mu$ decay channel.

For this reason, Monte Carlo events have been classified in decay channels according to the following strategy:

- if a τ decays in 3-prongs, it is classified as a $\tau \to 3h$;
- if the τ lepton has only one daughter for which $D_{TFD} > 0.8$ or the track length $\times$ density of material crossed is larger than 660 g/cm^3 (see section 3.1.1) the event is classified as $\tau \to \mu$;
- if the τ daughter shows an identified electron shower it is considered as $\tau \to e$;
- if the τ particle has only one daughter which has not been classified neither as a muon nor as an electron the event is considered as $\tau \to 1h$.

Fractional increase of the efficiency is given by:

$$\frac{\epsilon_{Mig} - \epsilon_{No\ mig}}{\epsilon_{No\ mig}} \times 100 \tag{4.5.1}$$

where ϵ_{Mig} is the detection efficiency, defined as in 4.3.1, considering the migration between decay channels and $\epsilon_{No\ Mig}$ the one without accounting for migration. The fractional increases are reported in table 4.4, separately for the categories ν_τ DIS LONG and SHORT, QE LONG and charm background LONG and SHORT for every decay channel.

	ν_τ DIS		ν_τ QE	charm	
Decay channel	LONG	SHORT	LONG	LONG	SHORT
$\tau \to 1h$	5.73	7.86	4.55	4.02	5.12
$\tau \to \mu$	0.41	0.52	/	5.04	/
$\tau \to 3h$	/	/	/	/	/
$\tau \to e$	/	/	/	/	/

Table 4.4. Fractional increase of efficiency due to migration between decay channels

The introduction of migration between decay channels makes the number of expected events more realistic and will be used in this analysis.

4.6 Number of expected events

With the new analysis strategy more signal and background events are expected, as summarized in table 4.5.

The systematic uncertainty associated to the signal takes into account contributions from the limited knowledge of the ν_τ cross-section and on the signal detection efficiency. For the signal central value, the default implementation for the ν_τ cross-section contained in the GENIE v2.6 simulation program is used. A 10% model-related systematic uncertainty can be estimated by considering the maximal deviations from the central value of the expected number of ν_τ candidates obtained when considering all available theoretical predictions. Since signal expectation is calculated by using location efficiencies determined from the 1μ and 0μ data samples, this value is at first order insensitive to systematic effects on efficiencies up to the primary vertex location level. The total systematic uncertainty on the expected signal is then set to 20%.
Using the measured sample of CNGS ν_μ^{CC} interactions with charm production, the uncertainty on the charm background has been estimated to about 20% [134].

Hadron re-interaction background has an estimated uncertainty of 30% from data-driven measurements of test-beam pion interactions in the OPERA bricks [132]. The systematic uncertainty on LAS has been obtained by a comparison between two different estimates, one based on a data-tuned GEANT4 Monte Carlo simulation [133] and the other on a direct extrapolation of data in the literature [135] and is set at 50%.

Channel	**Expected Background**				**Expected Signal**
	Charm	Had. re-interaction	Large μ-scat.	Total	
$\tau \to 1h$	0.15 ± 0.03	1.28 ± 0.38	–	1.43 ± 0.41	2.82 ± 0.56
$\tau \to 3h$	0.44 ± 0.09	0.09 ± 0.03	–	0.53 ± 0.12	1.75 ± 0.35
$\tau \to \mu$	0.008 ± 0.002	–	0.02 ± 0.008	0.03 ± 0.01	1.09 ± 0.22
$\tau \to e$	0.035 ± 0.007	–	–	0.03 ± 0.007	0.80 ± 0.16
Total	0.63 ± 0.13	1.37 ± 0.41	0.02 ± 0.008	2.0 ± 0.5	6.5 ± 1.3

Table 4.5. Expected signal and background events for the analysed data sample

Chapter 5

Results

5.1 Extended data sample

The final status of data analysis is shown in fig. 5.1. By the end of 2012, after the last run, 16872 neutrino interactions were reconstructed in the target (black line). Having discarded the ones due to false triggers (2.6%), bricks corresponding to 16428 neutrino interactions were extracted from the detector (brown line). Starting from the 2010 run, the muon momentum cut $p_\mu < 15$ GeV/c for 1μ events was applied before the analysis, therefore at least one changeable sheet doublet was scanned only for the events satisfying this request, which are 15038 out of 16428 (green line). A converging pattern or the muon track was found for 11810 of them (light green line). Almost for all of them at least one brick was scanned (light blue line), with the exception of a small fraction (about 0.5%) with high fog density of the corresponding emulsion films. The neutrino vertex was located in the brick for 7132 events (blue line). The procedure of decay search has been already performed for the 95.1% of the located interactions (pink line). In less than 5% of cases it was not possible to perform decay search procedure because the neutrino vertex was outside the fiducial volume.

Since the analysis of the bricks continued also after the discovery of the $\nu_\mu \to \nu_\tau$ appearance [2], the collected data sample is about 3.6% larger than the one reported in Chapter 3: the number of decay searched events is given in table 5.1 for each year of data taking, applying the *a-priori* selection $p_\mu < 15$ GeV/c. The number of p.o.t. is not proportional to the number of events since the detector mass decreases as the bricks are taken out in order to be scanned. In total 5603 events are used for the analysis shown in this Chapter.

In this sample, ten events survived the minimum bias criteria summarised in table 4.3. The distribution of the sum of the momenta of charged particles and γs

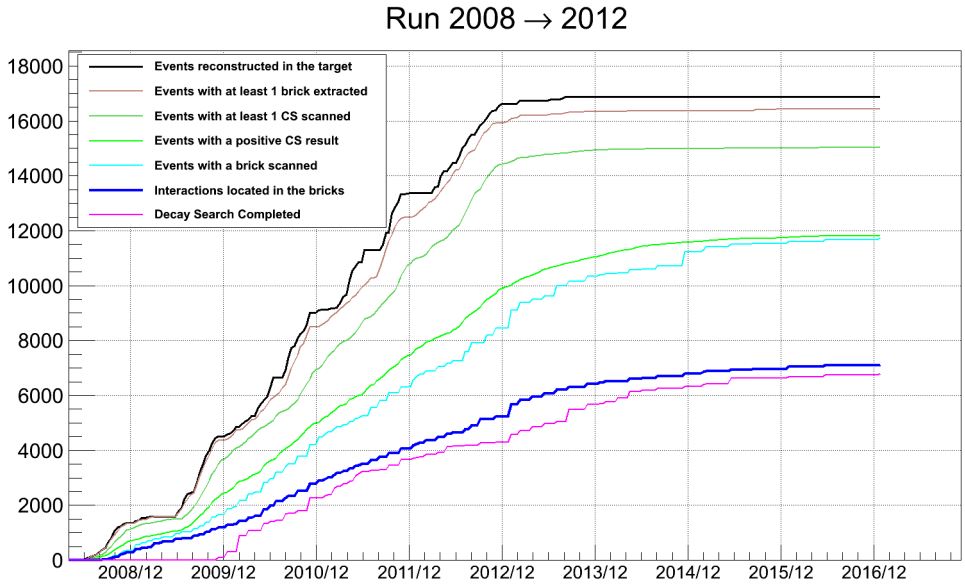

Figure 5.1. Evolution of OPERA data taking process. Number of OPERA events from the different levels of analysis chain for each year of data taking

	2008	2009	2010	2011	2012	Total
p.o.t. (10^{19})	1.74	3.53	4.09	4.75	3.86	17.97
0μ events	150	255	278	291	223	1197
1μ events ($p_\mu < 15$ GeV/c)	543	1024	1001	1031	807	4406
Total events	693	1279	1279	1322	1030	5603

Table 5.1. Extended data sample, used for the present analysis, for each run year

measured in emulsion is shown in fig. 5.2. The five events satisfying also the stringent criteria reported in table 3.2 will be referred to as "golden" events and have been already described in detail in Chapter 3, while the other ones will be called from now on "silver" events and will be described in the following section.

5.2 "Silver" events description

Out of the five "silver" events, three are ν_τ with a decay topology into single hadron, while the other two have a τ that decays into 3 hadrons.

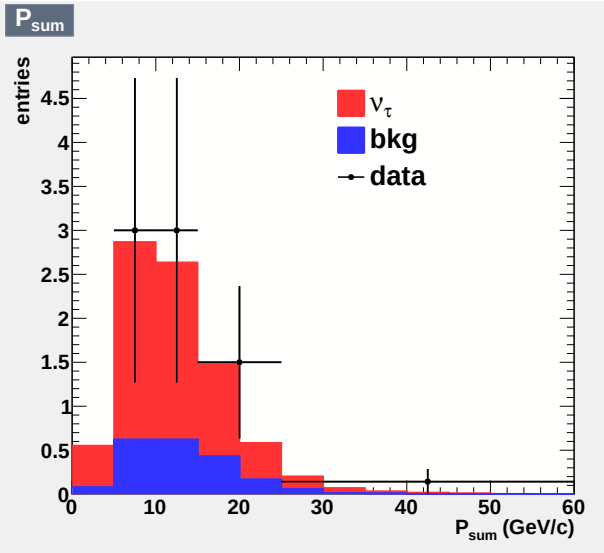

Figure 5.2. Sum of the momenta of charged particles and γs measured in emulsion: comparison between expectations and data

These events have been scanned with an angular acceptance up to $\tan\theta < 1$ for kinematical measurements and up to $\tan\theta < 3$ for the large angle track search. In all cases, no fragments at decay vertex have been found. Momenta have been estimated for primary and secondary tracks. Track follow down was performed when needed.

For all these events, I evaluated their kinematical variables, which are summarised in table 5.2. Values in bold are the ones not passing the cuts defined in table 3.2.

A brief description of all "silver" ν_τ candidates will be given in the following.

ID	Event Class.	Topology	z_{dec} (μm)	p^T_{miss} (GeV/c)	ϕ_{lH} (degrees)	p^T_{2ry} (GeV/c)	P_{2ry} (GeV/c)	θ_{kink} (mrad)	m (GeV/c^2)	γ at decay vtx
11143018505	0μ	kink	430	0.88	152	**0.24**	2.7	90	/	1
11172035775	0μ	kink	652	**1.29**	140	**0.25**	2.6	98	/	0
9190097972	0μ	kink	**10**	0.46	143	**0.33**	2.2	146	/	0
10123059807	0μ	trident	**-648**	0.60	**82**	/	6.7	231	1.2	0
11213015702	0μ	trident	407	>0.50	**47**	/	>6.3	83	**>0.94**	2

Table 5.2. Kinematical variables for "silver" events

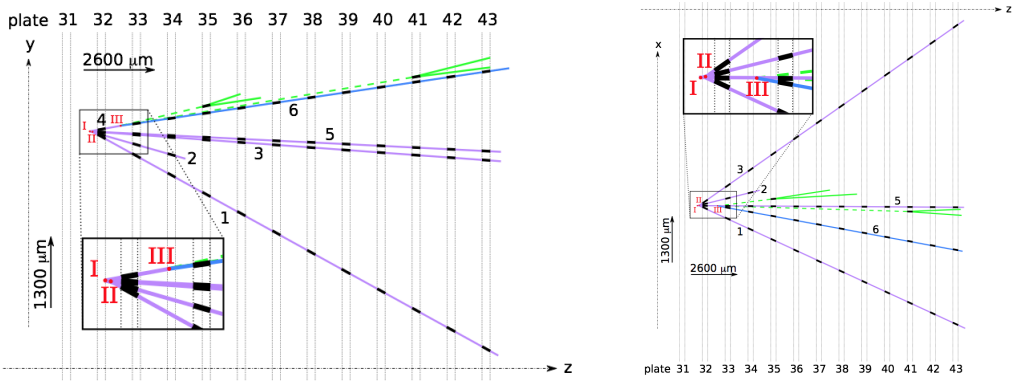

(a) (b)

Figure 5.3. Event display for the Event 11143018505: (a): yz (up) plane and (b) xz (down) plane. Base-tracks are represented in black, while volume tracks are represented in purple lines, or blue for the daughter particle. In the xz view, the parent (track 4) is not visible since it is behind track 5. For photons, only the first e^+e^- pair is shown.

Event 11143018505 The peculiarity of this event is that it has two secondary vertices within about 1 mm from the primary one. The neutrino vertex, labelled as I in 5.3 is defined by 3 tracks. Of the two secondary vertices, one (labelled as II) has 2-prongs and occurs in the same lead plate of the neutrino vertex, after a flight length of 103 μm, while the other one (labelled as III) exhibits a kink after a flight length of 1160 μm. The probability of observing an event with two secondary vertices is rather low: 0.1 events are expected with this topology. Most probable interpretations include ν_τ interaction with charm production or νNC interaction with double charm production. The discrimination between these hypothesis was performed using multivariate analysis methods. Among the most discriminating variables there are the ϕ_{lH} angle and the p_{2ry}. The event turned out to be likely a ν_τCC interaction with charm production. With respect to the non τ-charm hypothesis, the observed event has a very low probability, about 10^{-4}, which corresponds to a significance of 3.5σ [136, 137]. Nevertheless, in this hypothesis, vertex III does not satisfy the standard cut on $p^T_{2ry} > 300$ MeV/c, so it could not be considered as a "golden" candidate.

Event 11172035775 The primary vertex of this event is very downstream, about 2 mm from the downstream edge of the brick. It is made by 5 tracks, one of them exhibiting a kink after a flight length of 1100 μm, as shown in fig. 5.4. No black tracks were found pointing at the secondary vertex. A γ-ray was found pointing to primary vertex with an impact parameter of 11 μm. All tracks were followed in the

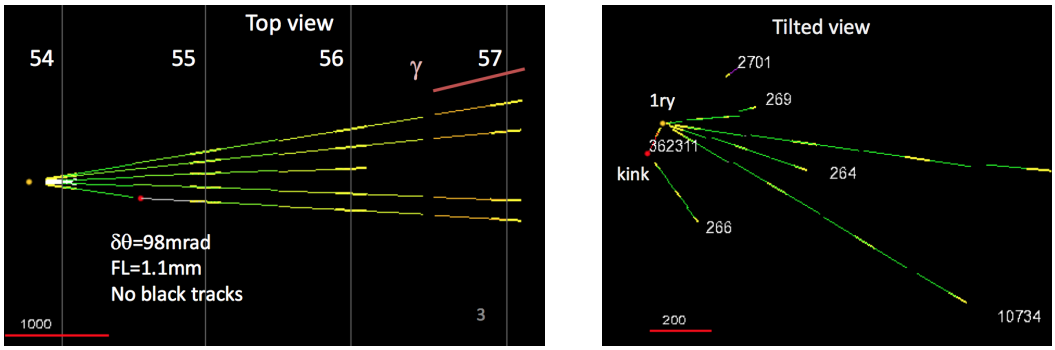

(a) (b)

Figure 5.4. Event display for the Event 11172035775: (a) Top view, (b) tilted view

downstream brick. Since the daughter track was found in the downstream brick, its momentum estimation by MCS was possible. The presence of a muon was excluded by TFD. The event does not satisfy the cut on p^T_{miss} and p^T_{2ry}.

Event 9190097972 The neutrino interaction vertex for this event has six charged tracks, one of which exhibits a kink, as shown in fig. 5.5. All tracks were recognized as hadrons: two of them stopped inside the brick, the others were classified thanks to the momentum-range correlation. The decay vertex occurred 10 μm upstream from the downstream face of the lead plate that contains the neutrino vertex, therefore it is classifies as short decay and was not considered by the previous analysis. Furthermore, the event does not satisfy the cut on the p^T_{2ry}.

Event 10123059807 This event has 7 reconstructed tracks, as it can be seen in fig. 5.6. The neutrino interaction vertex is in the lead between films 19 and 20. From the analysis of impact parameters, it turned out that all tracks could not originate from the same vertex: a short decay must have occurred. Looking at impact parameters, two hypothesis can be made on the event topology: a primary vertex with 4 tracks and a trident decay or a primary vertex composed by 3 tracks and a secondary vertex with 4 tracks attached. Other hypothesis have a probability lower than 0.01%, so have not been considered. The most probable hypothesis is the first one, with a vertex topological probability of 72.3%, evaluated on the base of the impact parameters. In addition, the 3+4 hypothesis is further suppressed by the absence of muons, which was confirmed by the TFD. One backward track was found in films 18-19 and a black segment in film 20. No γs were detected. The event was not selected as "golden" ν_τ candidate because of the short decay and the cut on ϕ_{lH}

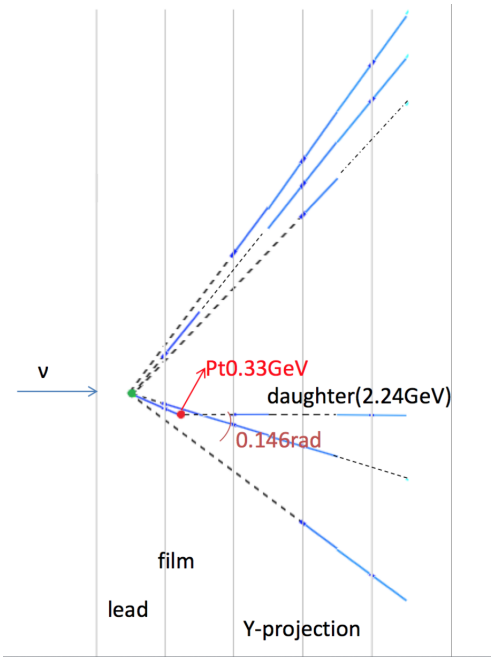

Figure 5.5. Event display for the Event 9190097972

angle.

Event 11213015702 The primary vertex of this event is in the lead between film 37-38 and is composed by two tracks and a black one. One of the two tracks, after 256 μm, decays into three hadrons which were found in the downstream film. One of the daughters ($d3$) interacts in the downstream lead, at a depth of 56 μm from the upstream face of the lead plate, forming two backwards black tracks, a grey track that exits the brick laterally after a couple of films and another track ($d3$-1) for which momentum was measured with the Multiple Coulomb Scattering. A scheme of the event is in fig. 5.7. Due to the short path length, it was not possible to directly measure its momentum, therefore an *ad hoc* procedure was used and will be described in detail. The minimum value of $d3$ momentum can be evaluated considering the momentum conservation of all the generated tracks. Black tracks are nuclear fragments evaporating from the nucleus, therefore their momentum was assumed to be the one due to Fermi motion of nucleons bound inside a nucleus. The track $d3$-1 was identified as a proton from its ionization and its $p\beta$ has been measured. Since $d3$ is a minimum ionizing particle (MIP), its energy is close to the momentum, $E \sim P$, therefore, from the evaluation of the total energy of the tracks produced in the interaction the minimum momentum was estimated.

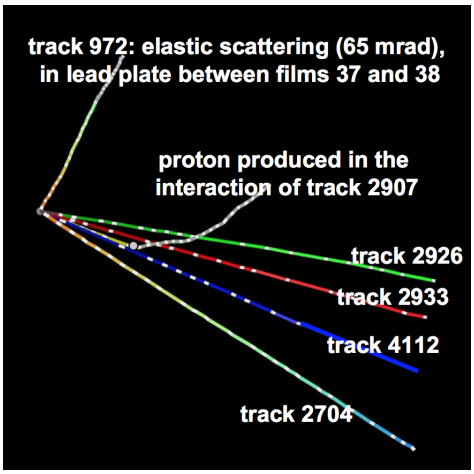

Figure 5.6. Event display for the Event 10123059807

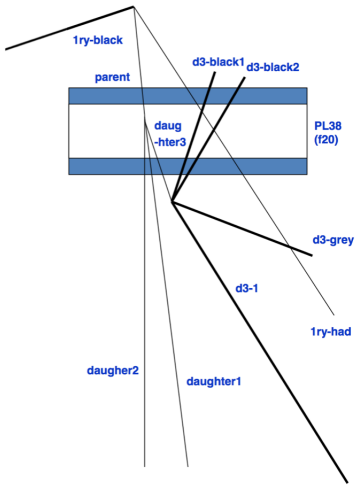

Figure 5.7. Event display for the Event 11213015702

This event does not satisfy the cut on ϕ_{lH} and m of the "golden" analysis.

5.3 Δm^2_{23}

OPERA is the first experiment that can measure Δm^2_{23} in appearance mode. The number of expected events, indeed, is proportional to the Oscillation Probability and the ν_τ cross-section: $N_{\nu_\tau} \propto \mathcal{P}_{\nu_\mu \to \nu_\tau} \cdot \sigma_{\nu_\tau}$, so, assuming the maximal mixing $\sin^2 2\theta_{23} = 1$ and standard σ_{ν_τ}, Δm^2_{23} can be evaluated as described in section 4.3.3.

Given 10 observed events, with 6.5 signal and 2.0 background expected events, it results:

$$\Delta m^2_{23} = (2.8 \pm 0.6) \cdot 10^{-3} \text{ eV}^2 \text{ at } 68\% \ C.L. \tag{5.3.1}$$

The 90% C.L. interval is $[1.84; 3.73] \cdot 10^{-3}\text{eV}^2$.

The result has been compared with the one given by PDG 2016 [109], which is $(2.50^{+0.13}_{-0.13}) \cdot 10^{-3}\text{eV}^2$, and the ones found in disappearance mode by other experiments such as DAYA-BAY, T2K and MINOS. The comparison with ranges at 68% C.L. is shown in fig. 5.8, where the previous value given by the OPERA Collaboration [2] is also reported. The measurement performed in this thesis is in agreement with the PDG value within 1σ.

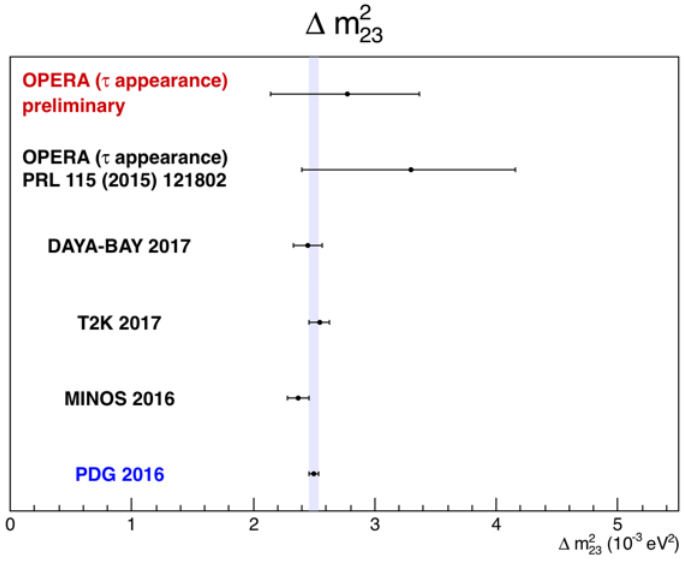

Figure 5.8. Comparison of Δm^2_{23} from different experiments at 68% C.L.

5.4 ν_τ cross-section

Up to now, σ_{ν_τ} has been measured only by the DONuT (Direct Observation of Nu-Tau) experiment, which observed 9 ν_τCC interactions, from a total of 578 observed neutrino interactions, but could not separate ν_τ from $\bar{\nu}_\tau$ [3].

ν_τ cross-section is given by 4.3.4:

$$\sigma_{\nu_\tau} = \sigma^0_{\nu_\tau} E K'(E)$$

as it has been described in section 4.3.4.

As already pointed out, OPERA is sensitive to the product of Δm^2_{23} and σ_{ν_τ}, since the observed events are τ neutrinos from the oscillation of ν_μ. Therefore, to evaluate ν_τ cross-section, Δm^2_{23} has been fixed. Assuming $\Delta m^2_{23} = 2.5 \cdot 10^{-3}$ eV^2 and the maximal mixing $\sin^2 2\theta_{23} = 1$:

$$\sigma^0_{\nu_\tau\ meas} = \frac{N^{obs}_{\nu_\tau} - N^{exp}_{bkg}}{N^{exp}_{\nu_\tau}} \sigma^0_{\nu_l\ SM} = (8^{+4}_{-3}) \cdot 10^{-39}\ \text{cm}^2\text{GeV}^{-1}\ at\ 68\% C.L. \qquad (5.4.1)$$

The range at 90% C.L is $[3.6; 14.9] \cdot 10^{-39}$ cm^2 GeV^{-1}. The measurement performed in this thesis is in agreement with the SM value [109], which is $6.7 \cdot 10^{-39}$ cm^2 GeV^{-1}, within 1σ.

The result is affected by the MC σ_{ν_τ} uncertainties, which are related especially to the QE and RES terms, not known with high precision yet, and are more relevant at low energies. This is taken into account as a 20% uncertainty on the number of expected events.

5.5 Statistical significance

I have evaluated the significance of ν_τ observation following two different approaches: one based on P-values and the other one based on the Likelihood method. Both approaches use the expectation in each channel separately. The observed significance only depends on the number of candidates observed in real data and on the estimated level of background for the considered channel.

5.5.1 P-value

The first method to evaluate the significance of the observed ν_τ candidates is based on the Poisson statistics. Let's consider a counting experiment which observes N_{obs}

events with an estimated background of N_{bkg} events. The P-value of the experiment (P_v) is defined as the probability that background fluctuations could produce a number of events equal or larger than N_{obs}.

The same definition can be applied to an experiment like OPERA, where the signal is searched in N different independent channels, each with an estimated background $N_{bkg}(i)$, $i = 1, .., N$. Different channels can be treated as independent experiments. The Fisher's method [121], in cases like this, is often used to combine the results of independent experiments, but it is not valid any more for small level of background in counting experiments. The problem arises when combining the P_v of each channel in order to derive the global significance of the experiment. The mathematical basis of the Fisher's method is that the quantity $-2\ln(P_v)$ shows a χ^2 distribution with 2 degrees of freedom, denoted hereafter χ^2_2. In case of different observation channels (i=1,..,N), the combined value $\sum_{i=1}^{N} -2\ln(P_v(i))$ follows a χ^2_{2N} distribution. The global significance of the experiment is then deduced from the fraction of the area of this distribution below the observed χ^2_{2N} value. According to the Fisher's formula, the combined P-value, P_F, can be evaluated as:

$$P_F = P\sum_{i=1}^{N}\frac{(-\ln P)^i}{i!} \tag{5.5.1}$$

where $P = \prod_{i=1}^{N} P_v(i)$. Nevertheless, when N_{bkg} is small (less than 10), as in the OPERA experiment, the P_v distribution is not uniform and, therefore, $-2\ln(P_v)$ does not follow a χ^2_2 distribution.

To overcome the problem, the key is to consider an experiment with n observed events as a virtual experiment with a number of events chosen randomly between n and $n+1$ [122]. This smearing procedure reflects the fact that an experiment with n events may transform into an experiment with $n+1$ events by just adding some more data. The P_v corresponding to this "smeared state", denoted as $P_{v_{smear}}$, is given by:

$$\begin{aligned} P_{v_{smear}} &= P_v[n+1] + \Delta P_v \times u \\ \Delta P_v &= P_v[n] - P_v[n+1] \\ P_v[n] &= \sum_{j=n}^{\infty}\frac{n_{bkg}^j}{j!}e^{-n_{bkg}} \end{aligned} \tag{5.5.2}$$

where n_{bkg} is the expected number of background events and u is a random number uniformly distributed between 0 and 1.
The distribution of the p-values evaluated by this method becomes continuous and flat. Consequently $-2\ln P_{v_{smear}}$ obeys a χ^2_2 distribution, recovering the validity of the Fisher's method.

A numerical method can be used to combine P-values, based on the production of a large set of pseudo-experiments.
I have simulated a set of 10^{10} background only pseudo experiments by looping over the following steps, for each channel:

1. A value of N_{obs} (i) is generated according to the Poisson distribution
2. Poisson P-value $P_v[N_{obs}(i)]$ is calculated

Then $P = \prod_{i=1}^{N} (P_v[N_{obs}(i)])$ is evaluated. All pseudo-experiments are sorted in increasing order of P. P-value is obtained as the fraction of pseudo experiments having P equal or smaller than the one of the real experiment [138].
Considering 1.43 events of expected background and 6 observed events in the $\tau \to 1h$ decay channel, 0.52 events of expected background and 3 observed events in the $\tau \to 3h$ decay channel, 0.03 events of expected background and 1 observed event in the $\tau \to \mu$ decay channel, and 0.03 events of expected background in the $\tau \to e$ decay channel with no observed events, as reported in table 4.5, the combined P-value is $1 \cdot 10^{-5}$, corresponding to a significance of 4.2σ. As expected, with the minimum bias selection, significance decreases respect to the standard analysis, since the number of background expected events is larger.

However, the fact that 5 out of 10 ν_τ candidates survived also the stringent kinematical cuts should be taken into account. For this reason, instead of considering 4 channels, 8 channels can be defined: 4 "golden" channels undergoing the analysis with high signal to noise ratio, and other 4 "silver" channels, complementing to the minimum bias selection, as reported in table 5.3.

With this strategy, P_v is $3 \cdot 10^{-8}$, corresponding to a significance of 5.4 σ.

5.5.2 Likelihood ratio

The other approach to calculate the significance is the likelihood ratio (LR), in which the likelihood of observing N_{obs} events is considered, given the background only hypothesis and signal plus background hypothesis.

The expectation value of the observed events can be written as $\mathcal{E}[N_{obs}] = \mu s + b$, where μ is the strength parameter, s the expected signal and b the expected background. More specifically, $\mu = 0$ corresponds to the background only hypothesis case and $\mu = 1$ to the signal plus background case.

The likelihood function is built by multiplying the Poisson probabilities of each channel:

$$\mathcal{L}(\mu) = \text{Poisson}(N_{obs}|\mu s_i + b_i) = \prod_{i=1}^{channels} \frac{(b_i + \mu s_i)^{n_i} \exp(-b_i - \mu s_i)}{n_i!} \qquad (5.5.3)$$

Channel	**Expected Background**				**Expected Signal**	Observed
	Charm	Had. re-interaction	Large μ-scat.	Total		
$\tau \to 1h$	0.023	0.024	–	0.047	0.57	3
	0.13	1.26	–	1.39	2.25	3
$\tau \to 3h$	0.21	0.003	–	0.21	1.1	1
	0.23	0.08	–	0.31	0.66	2
$\tau \to \mu$	0.003	–	0.0002	0.003	0.55	1
	0.005	–	0.016	0.021	0.54	0
$\tau \to e$	0.035	–	–	0.03	0.75	0
	0.0004	–	–	0.0004	0.04	0
Total	0.63	1.37	0.02	2.0 ± 0.5	6.5 ± 1.3	10

Table 5.3. Expected signal and background events for the analysed data sample considering 8 channels: for each decay channel the first line refers to the "golden" analysis, while the second one to the "silver" one

The likelihood ratio between the background only hypothesis and the signal plus background hypothesis is defined as:

$$LR = -2\ln\left(\frac{\mathcal{L}_{b+s}(0)}{\mathcal{L}_{b+s}(\hat{\mu})}\right) = -2\ln\left(\frac{\prod_{i=1}^{channels} \frac{b_i^{n_i}\exp(-b_i)}{n_i!}}{\prod_{i=1}^{channels} \frac{(b_i+\hat{\mu}s_i)^{n_i}\exp(-b_i-\hat{\mu}s_i)}{n_i!}}\right) = \\ = -2\ln\mathcal{L}_{s+b}(0) + 2\ln\mathcal{L}_{s+b}(\hat{\mu}) = \chi^2(0) - \chi^2(\hat{\mu}) = \Delta\chi^2 \tag{5.5.4}$$

where the $\hat{\mu}$ was the maximum likelihood estimator for μ.

I implemented this method using RooStats [139]. The Profile likelihood ratio one sided has been chosen, corresponding to $\mu = 0$, with the Frequentist calculator, using $128 \cdot 10^7$ pseudo-experiments. Considering 4 channels, as in table 4.5, $P_{value} = 2.1 \cdot 10^{-5}$, corresponding to 4.1σ, while with the strategy of considering 8 different channels reported in table 5.3, $P_{value} = 7.0 \cdot 10^{-8}$, corresponding to a significance of 5.3σ. The Profile Likelihood Ratio considering 8 different channels is shown in fig. 5.9, where the red distribution corresponds to the background only hypothesis and data is represented by a black line.

5.6 Multivariate analysis

So far, only the number of expected background events in each decay channel, together with the number of observed events, has been used to evaluate the ν_τ appear-

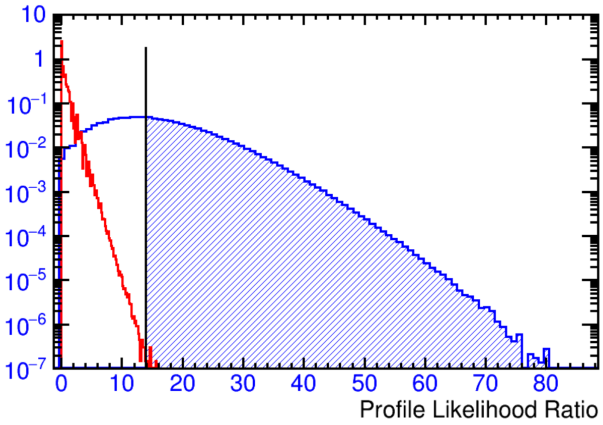

Figure 5.9. Profile Likelihood Ratio using $128 \cdot 10^7$ MC pseudo-experiments. The red distributions corresponds to the background-only hypothesis, while the blue one considers the signal+background hypothesis. The black line represents the data

ance significance, without considering the features of the events.

To improve the significance evaluation and perform signal to background separation, namely classifying the 10 ν_τ candidates as signal or background, a multivariate analysis can be used. Different multivariate methods have been tested. The one that gives the best discrimination power is the Boosted Decision Tree (BDT). A detailed description of this method can be found in Appendix A.1. Results will be described in this section.

Different multivariate techniques have been considered and their performances for signal to background discrimination compared. The result of the comparison is shown in fig. 5.10. As a result, BDT gave the best performance, and therefore, was chosen for the multivariate analysis.

The input sample for BDT training contained Monte Carlo events that passed all the analysis chain described in section 4.2, showed a decay topology and survived the minimum bias requests in table 4.3. The signal sample is made of DIS and QE ν_τ interactions, in proportion to the number of expected events for each type.

ν_τ events have been weighted for the oscillation probability $\mathcal{P}_{\nu_\mu \to \nu_\tau}$ (see eq. 2.1), while charm events according to the charmed particle hadronization fractions reported in table 2.4.

MC events were split randomly into two samples: one was used for BDT training, while the other one for testing the results. All the parameters used for training, described in Appendix A.1, such as the boosting parameter, the number of trees, the separation depth between them, the minimum number of events in a node and the

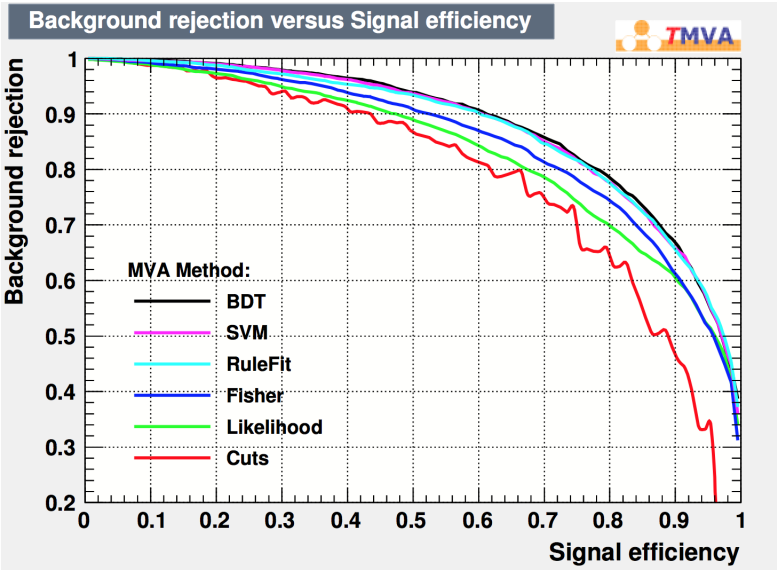

Figure 5.10. Comparison of the different methods for the multivariate analysis. The best performance is obtained using BDT method

splitting mode for the nodes have been optimised for each decay channel in order to obtain the best agreement between test and training.

The measured ν_τ candidates are reported on the plots as golden or silver vertical lines.

5.7 $\tau \to 1h$

The single hadron decay channel is constituted by 96% of DIS interactions. The background component includes charm decay and hadron re-interaction. Hadron re-interaction represents the major source of background, being the 89% of the total. Six ν_τ candidates have been selected decaying into a single hadron.

The following input variables have been used: z_{dec}, θ_{kink}, p_{2ry}, p^T_{2ry}, p^T_{miss}, ϕ_{lH} and the number of γs at decay vertex. The requirements for a γ to be reconstructed are: $p_\gamma > 500$ MeV/c and both slopes<1 rad.

The distribution of kinematical variables are shown in fig. 5.11, where signal is represented in blue and background in red. Distributions for both samples are normalised to unity. Vertical lines represent measured values.

The variable with the best discrimination power is the ϕ_{lH} angle.

To maximize the performance of the BDT analysis, it is desirable to choose uncorrelated variables with good discriminating power. The correlation between them

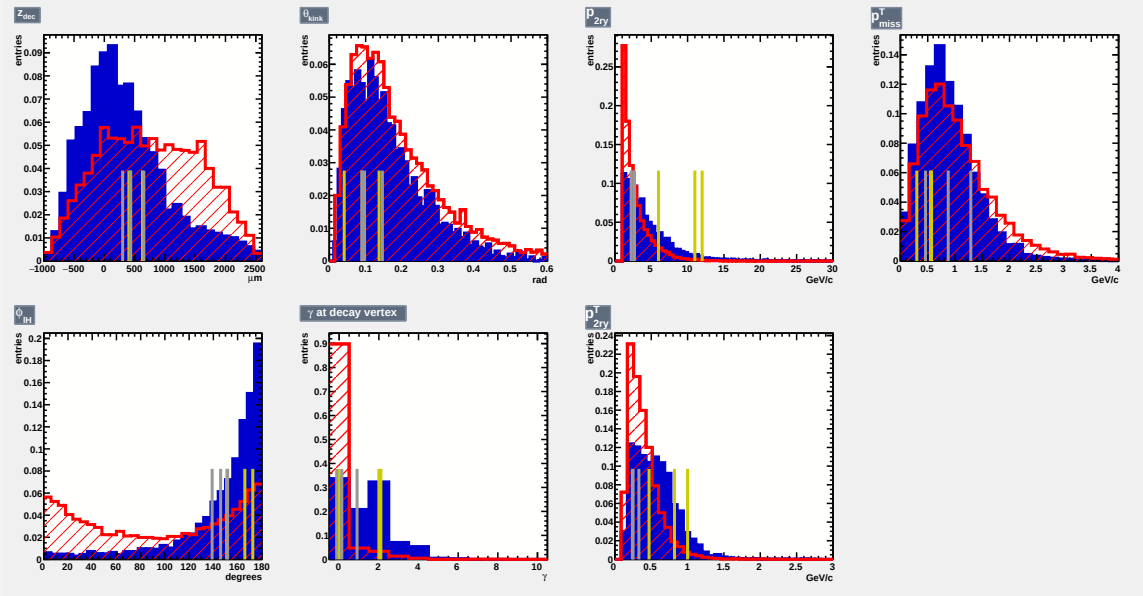

Figure 5.11. Distribution of the kinematical variables used for the BDT analysis in the $\tau \to 1h$ decay channel

is shown in fig. 5.12 by means of two matrices, one for signal and one for background.

Even though some variables, such as p^T_{2ry} and p^{2ry}, show a correlation larger than 50% for signal, this are not correlated in the same way for background, thus recovering their discriminating power. The same applies for p^T_{2ry} and θ_{kink}, which are correlated only for background.

The BDT training was performed using the AdaBoost algorithm, described in Appendix A.1.2 with the boosting parameter $\beta = 0.5$. 314 trees were created with a depth of 3 separations. The minimum number of events in a node was set to 10% of the initial training sample. The splitting in the nodes was performed using the gini index, given by $P(1-P)$, where P stands for the purity of a node. The number of cuts has been left free, therefore all possible cuts on the training sample are tried by the algorithm in order to find the best one.

As an example, the check for over-training is shown in fig. 5.13. The Kolmogorov-Smirnov test result is 0.29 for signal and 0.014 for background. The test sample reproduces the distribution of the training in both cases.

The BDT response is reported in fig. 5.14, where the measured values are also shown. MC distributions are normalised to the number of expected events shown in table 4.5.

The best cut can be chosen in terms of purity and efficiency. In this analysis, a cut where the product of purity × efficiency is maximised has been chosen. As

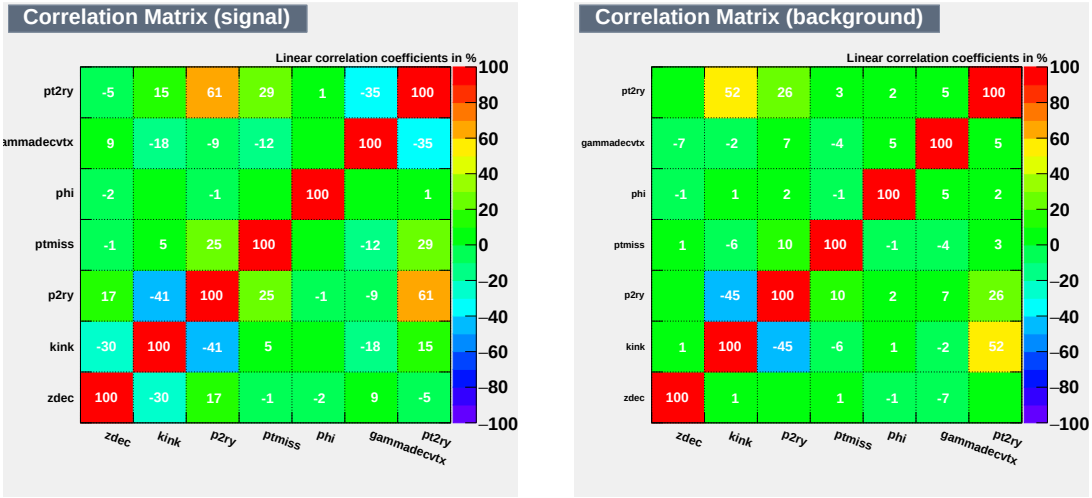

(a) (b)

Figure 5.12. Correlation Matrices of the variables used in the $\tau \to 1h$ decay channel for signal (a) and background (b)

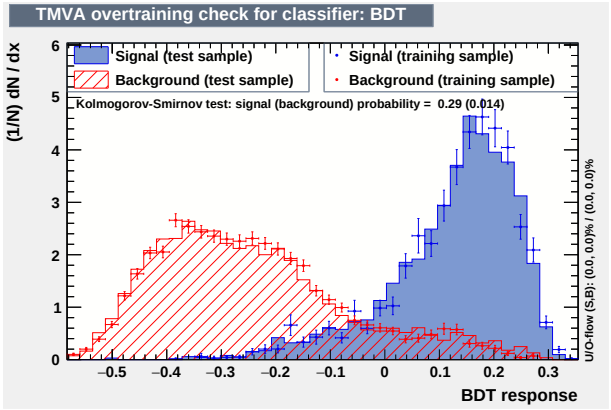

Figure 5.13. BDT over-training check for the $\tau \to 1h$ decay channel

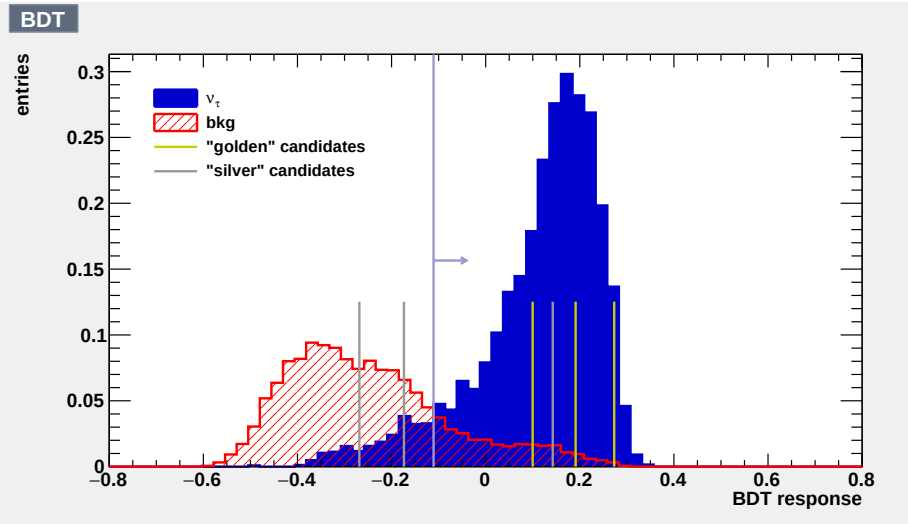

Figure 5.14. BDT response for the $\tau \to 1h$ decay channel

shown in fig. 5.15, the best cut is -0.11, having 92% of signal and rejecting 81% of background.

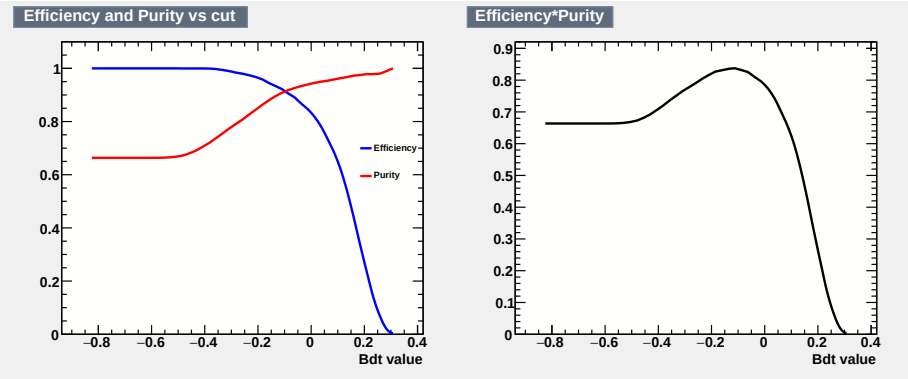

Figure 5.15. Efficiency and Purity for the BDT response in $\tau \to 1h$ decay channel

Events above the cut are considered signal-like, while the ones below background-like. The events 9190097972 and 11172035775 are below the cut, in agreement with the expectation of 1.43 ± 0.41 expected background event. This result is a confirmation of the good understanding of the expected background.

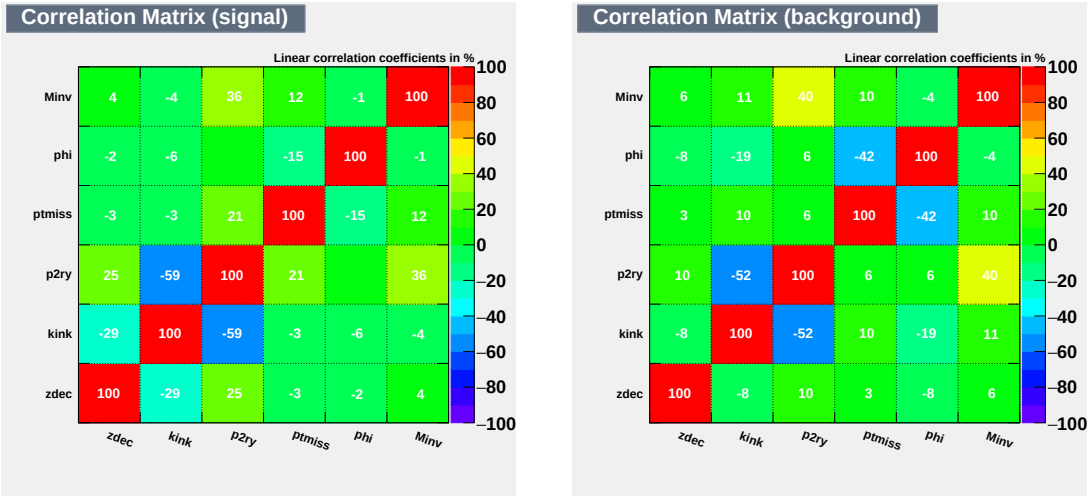

(a) (b)

Figure 5.16. Correlation Matrices of the variables for the $\tau \to 3h$ decay channel for signal (a) and background (b)

5.8 $\tau \to 3h$

For the three hadrons decay channel, signal sample includes 82% of DIS events and 18% of QE. Background consists of charm decay (83%) and hadron re-interaction (17%). Three ν_τ candidates have been selected.

Since charm and τ decays have very similar behaviour, we expect that the separation between signal and background with the BDT will be less efficient in this decay channel.

The variables evaluated for this decay channel are: z_{dec}, θ_{kink}, p_{2ry}, p^T_{miss}, ϕ_{lH}, m and m_{min}. The correlation between them is shown in fig. 5.16. Since for invariant mass and minimum invariant mass there is a correlation larger than 70%, the latter has been eliminated, given its inferior discriminating power.

The distributions of the variables used for the BDT analysis are shown in fig. 5.17, normalised to unity. τ events have been weighted for the oscillation probability $\mathcal{P}_{\nu_\mu \to \nu_\tau}$, while charm events according to every charmed particle production rate.

The BDT training was performed using the AdaBoost algorithm with $\beta = 0.5$ for the boosting. 200 trees were created with a depth of 2 separations. The minimum number of events in a node was set to 10% of the initial training sample. The separation was performed using the gini index with $nCut = 20$, which is a good compromise between computing time and step size [120].

The BDT response is reported in fig. 5.18, normalised to the number of expected

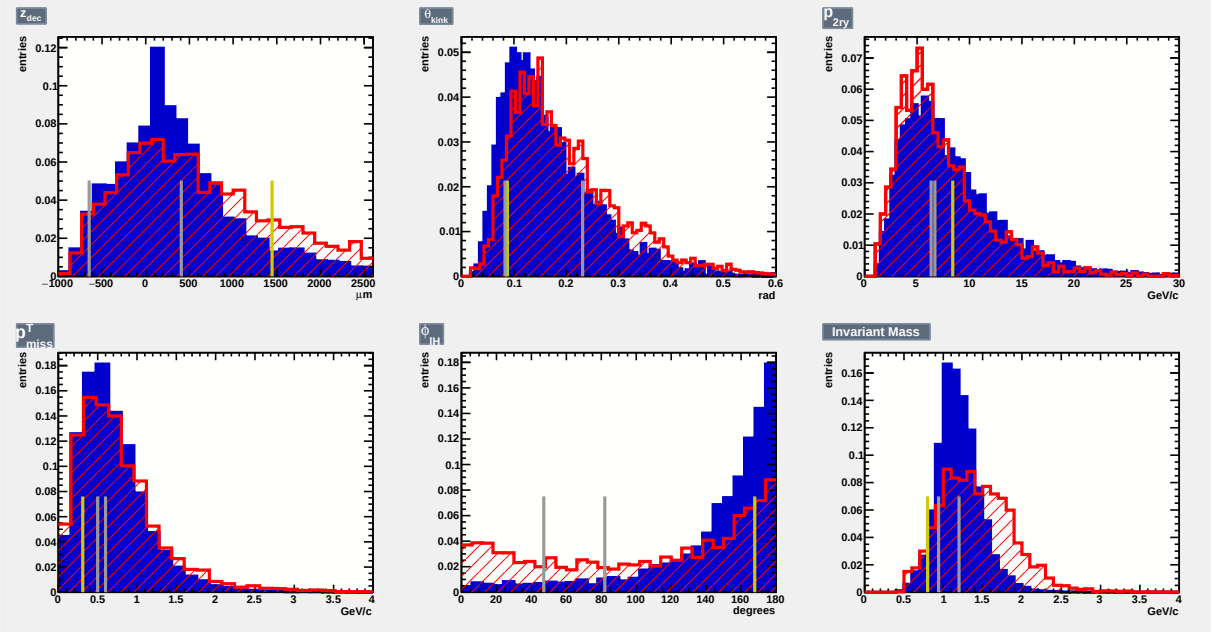

Figure 5.17. Distribution of the kinematical variables used for the BDT analysis in the $\tau \to 3h$ decay channel

events shown in table 4.5. As expected, the signal and background distributions are almost superimposed. The cut was evaluated as before by maximising where the product of purity $\times$ efficiency. As shown in fig. 5.19 this happens at -0.23, having 98% of signal, and rejecting 20% of background.

The "golden" ν_τ candidate lies in the peak of signal and also the two "silver" events are above the defined cut. Nevertheless, since the two distributions are overlapped, the BDT does not add discriminating power to the counting method.

5.9 $\tau \to \mu$

In $\tau \to \mu$ decay channel, charm background is strongly reduced by the daughter muon charge measurement, which is negative for signal. Cases in which the charge is not measured are also taken into account. In addition to muon charge, only z_{dec}, θ_{kink}, p_{2ry} and p^T_{2ry} are used for the analysis.

Signal sample is composed for 90% by DIS and for 10% by QE events. Background includes charm decay (32%) and large angle scattering (68%). Only one candidate is selected in this decay channel.

Correlations between variables are below the critical values and different between

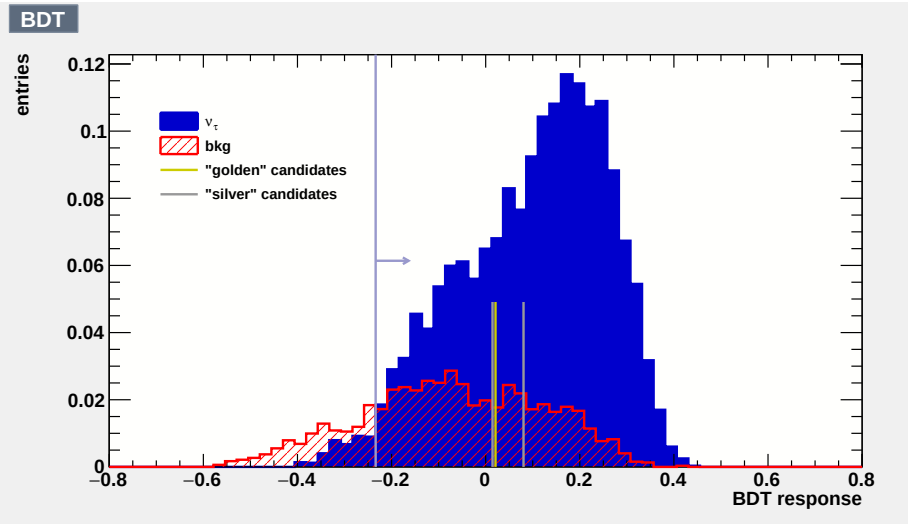

Figure 5.18. BDT response for $\tau \to 3h$ decay channel

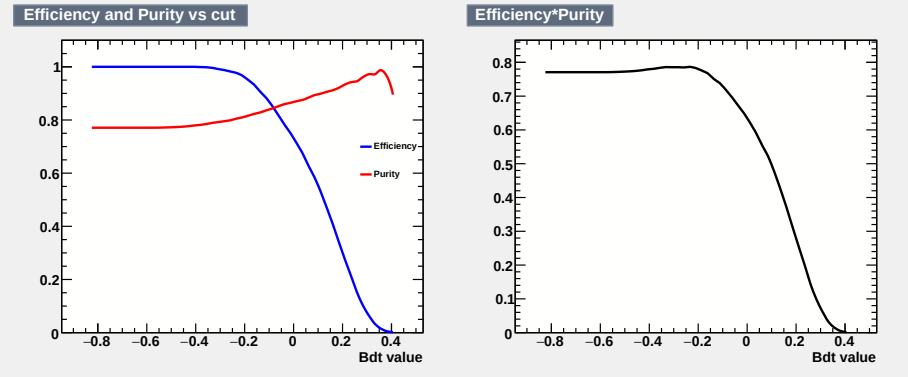

Figure 5.19. Efficiency and Purity for the BDT response in the $\tau \to 3h$ decay channel

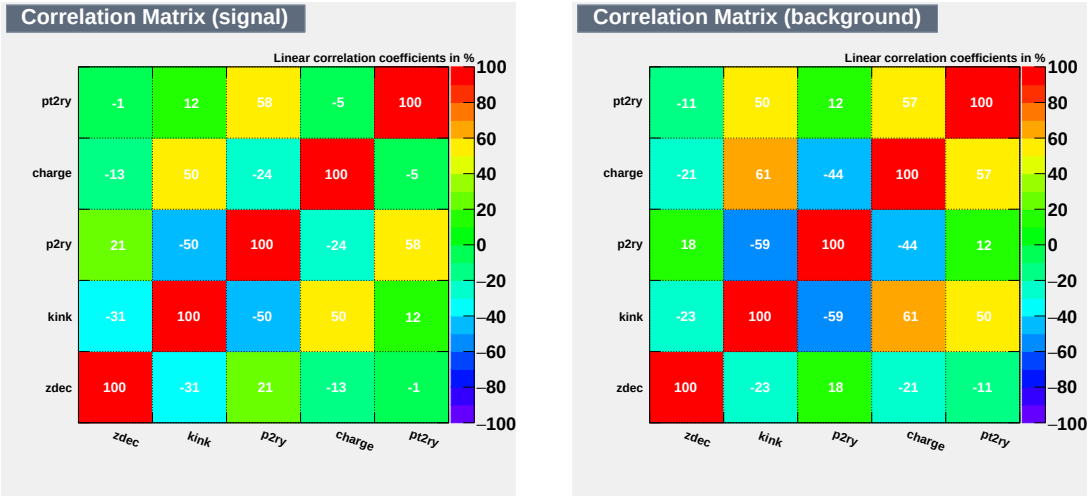

(a) (b)

Figure 5.20. Correlation Matrices for signal (a) and background (b) variables for the muon decay channel

signal and background, as shown in fig. 5.20, so all variables will be used in the analysis.

Variables distributions are shown in fig. 5.21. These are normalised to unity. All variables show a good discrimination power between signal and background. The ones with the larger discriminating power are p^T_{2ry}, θ_{kink} and the muon charge.

The BDT training was performed using the AdaBoost algorithm with $\beta = 0.5$ for the boosting. 400 trees were created with a depth of 2 separations. The minimum number of events in a node was set to 5% of the initial training sample. The separation was performed using the gini index with $nCut = 20$.

The BDT response is reported in fig. 5.22, together with the values for the ν_τ candidate. MC distributions are normalised to the number of expected events shown in table 4.5. The two background sources are well separated each other, having difference characteristics. Their distributions are, nevertheless, overlapped to the signal one.

The best cut between the signal and the background is evaluated by maximising the product of purity $\times$ efficiency. As shown in fig. 5.23, the best cut is -0.26, having 99.8% signal and rejecting 15.7% of background. Since the number of expected events is small, it is indeed more efficient to take a larger background without discarding signal.

The "golden" ν_τ candidate lies in a signal-only region, likely due to the statistics

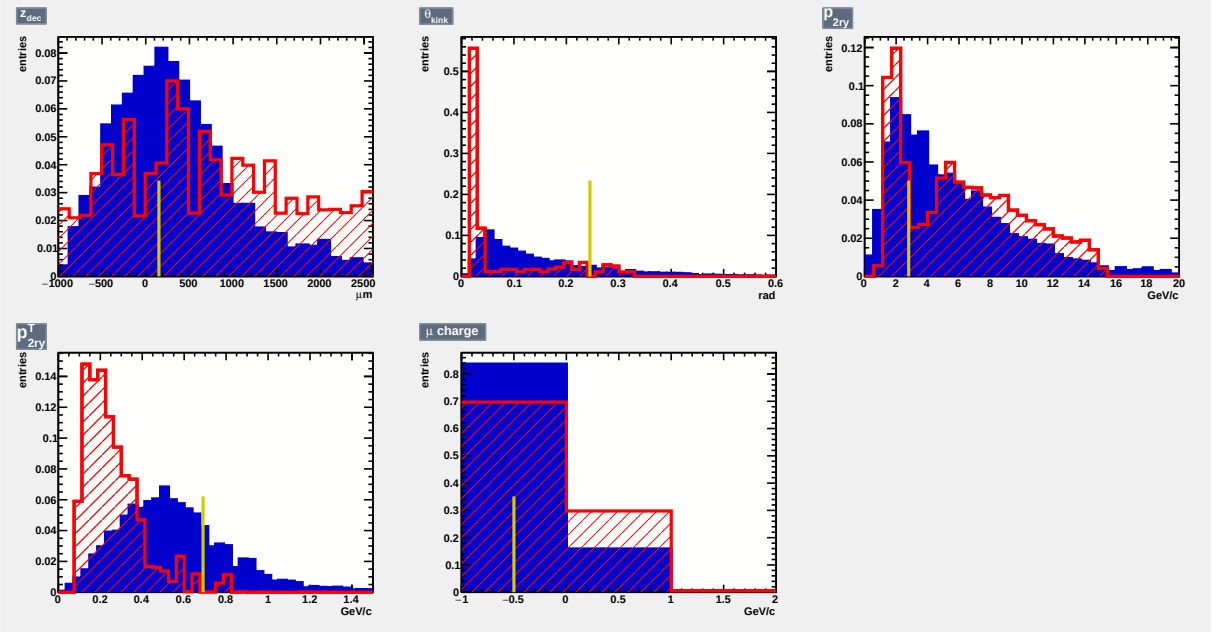

Figure 5.21. Distribution of the kinematical variables used for the BDT analysis in the $\tau \to \mu$ decay channel

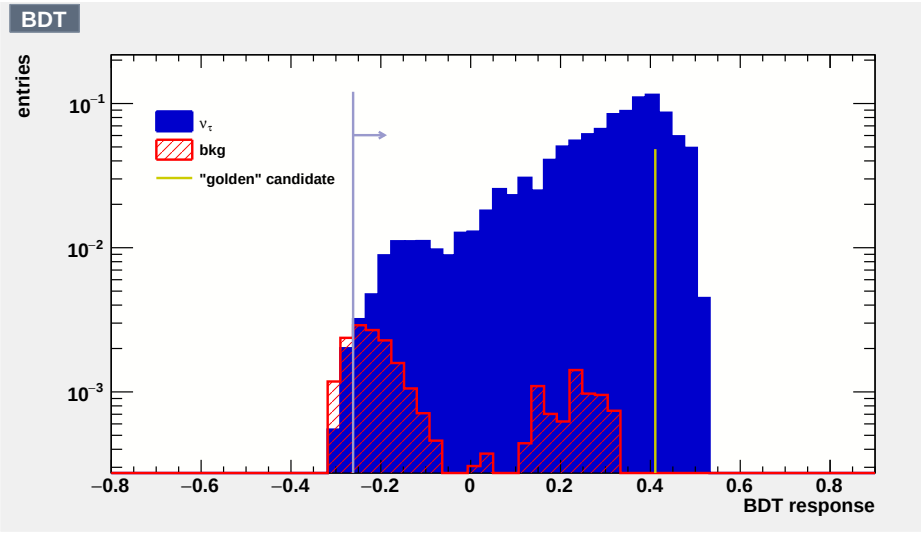

Figure 5.22. BDT response for $\tau \to \mu$ decay channel. The logarithmic scale has been used

available. Therefore the charm background has been fitted with a Gaussian distribution, which appears to be a largely conservative assumption, in order to evaluate

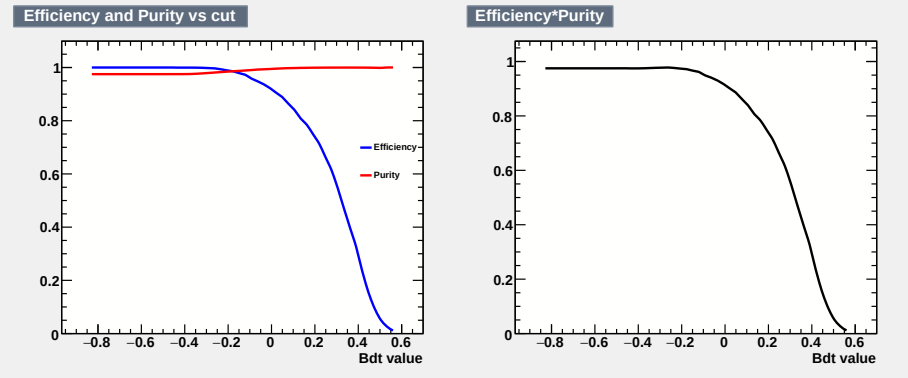

Figure 5.23. Efficiency and Purity for the BDT response in $\tau \to \mu$ decay channel

a value for the event $f(BDT)$.

5.9.1 Observation of the τ lepton number measurement

Lepton number of τ neutrinos has never been measured. In the muon decay channel, the OPERA experiment can distinguish neutrinos from anti-neutrinos looking at the charge of the muon produced in τ decays. The charge of the muon daughter of the ν_τ candidate in this decay channel has been measured to be negative at 5.6σ level [140].

For the lepton number measurement, an additional background source has to be considered, on top of the charm and LAS background. The CNGS beam, indeed, has a 2% contamination of $\bar{\nu}_\mu$ which could oscillate into a $\bar{\nu}_\tau$. Exotic processes such has $\bar{\nu}_\mu \to \nu_\tau$ or $\nu_\mu \to \bar{\nu}_\tau$ will not be considered here. The number of $\bar{\nu}_\tau$ expected, whose τ^+ decays into a μ^+ with a misidentified or not measured charge, is 0.0024 ± 0.0005.

This background source amounts to 9% of the total background, while the other contributions coming from LAS and $charm \to \mu$ are respectively 62% and 29%. The kinematical distributions of the variables used in the analysis are reported in fig. 5.24, where the contributions coming from the different background sources have been distinguished with different colours.

The BDT result is shown in fig. 5.25. In order to evaluate a value for the event $f(BDT)$ a conservative gaussian fit has been performed.

The significance for the observation of a ν_τ in this decay channel can be performed improving the result of the counting method with the one of the BDT analysis: this is evaluated as the probability that the background produce one event with signal-like characteristics as the observed one, according to the BDT response.

For the significance estimation, the Likelihood method has been used. The number of observed events n is a random variable that obeys the Poisson statistics. This is combined with the probability density function $f(BDT)$ given by the BDT re-

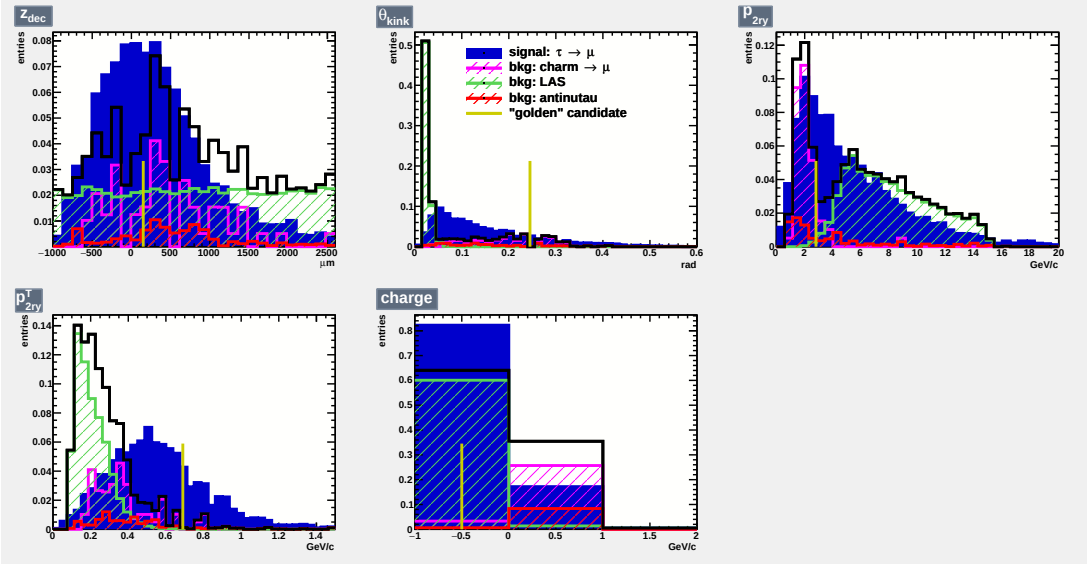

Figure 5.24. Distribution of the kinematical variables used for the BDT analysis in the $\tau \to \mu$ decay channel for the lepton number measurement

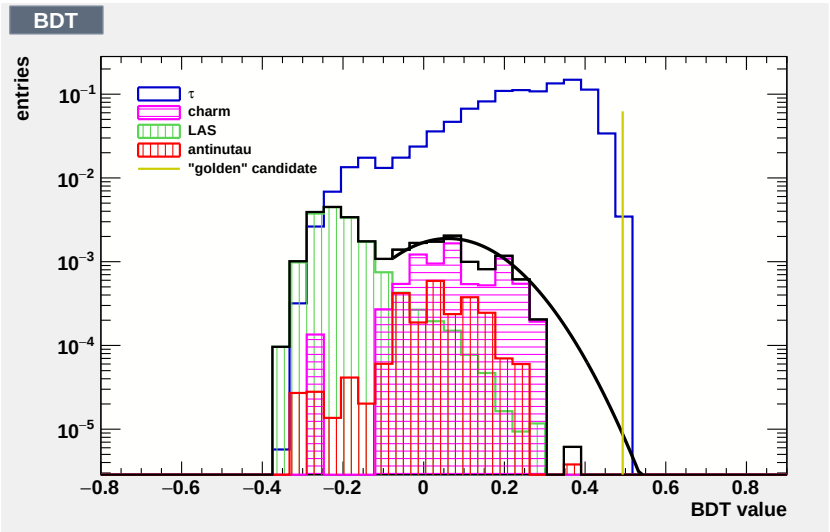

Figure 5.25. BDT response for $\tau \to \mu$ decay channel, considering also the background coming from oscillated $\bar{\nu}_\mu$. The logarithmic scale has been used and the three background sources are highlighted with different colours

sponse for background, which is shown in black in fig. 5.25. The extended likelihood function assumes the form:

$$\mathcal{L} = \frac{b^n e^{-b}}{n!} \cdot \prod_{i=1}^{n} f(BDT_i) \tag{5.9.1}$$

where n is the number of observed events and b the number of background expected events.

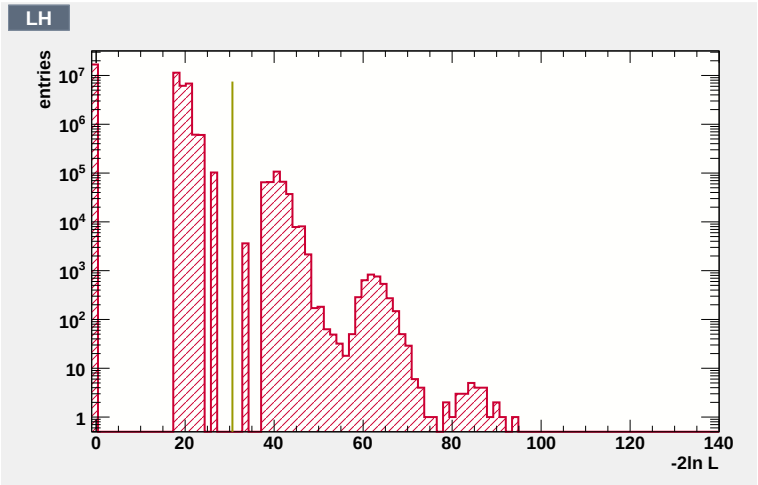

Figure 5.26. Likelihood function for 10^9 MC pseudo-experiments. The green line represents the value of the ν_τ candidate

A sample of 10^9 MC pseudo-experiments was generated according to the background only hypothesis. For each pseudo-experiment the number of observed events was generated according to the Poisson distribution with mean value on the number of background expected events. Each event has been taken randomly from the $charm \to \mu$ or LAS MC sample, according to the relative proportions the BDT value has been evaluated. Then, for each MC experiment, $\mathcal{L}$ has been calculated. The distribution of $-2\ln\mathcal{L}$ is shown in fig. 5.26.

The P-value of the experiment is defined as the probability that background fluctuations have $-2\ln\mathcal{L} > -2\ln\mathcal{L}^*$, where $\mathcal{L}^*$ is the observed value for the ν_τ candidate.

The P-value is $3.15 \cdot 10^{-4}$, corresponding to a significance of 3.4σ. This result allows to claim for the first observation of the τ lepton number.

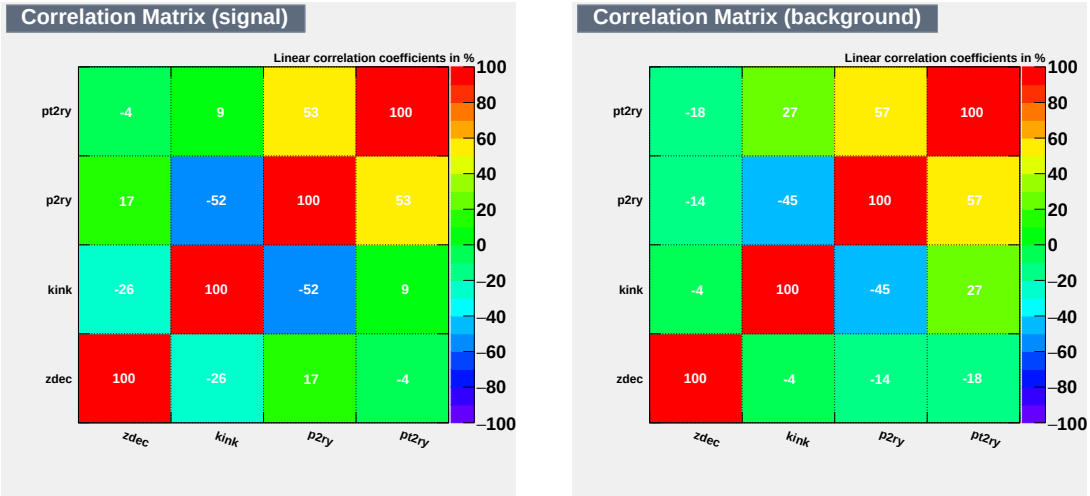

(a) (b)

Figure 5.27. Correlation Matrices for signal (a) and background (b) variables for the $\tau \to e$ decay channel

5.10 $\tau \to e$

Even though no $\tau \to e$ candidates have been found, the multivariate study of signal to background discrimination has been carried out also for this decay channel, in view of estimating the overall significance for ν_τ appearance using the BDT probability functions.

Signal sample includes a mixture of DIS (94%) and QE (6%) events, while background comes only from charm decays. Due to the similar behaviour of τ and charm decays variable distributions, it is difficult to discriminate signal and background.

The variables evaluated for this decay channel are: z_{dec}, θ_{kink}, p_{2ry} and p^T_{2ry}.

The correlation between them is shown in fig. 5.27: it is very similar for the two samples, but all are below 60%. All variables have been used for the analysis.

The variables distributions are shown in fig. 5.28, normalised to unity. As expected, the distributions are similar for all variables.

The BDT training was performed using the AdaBoost algorithm with $\beta = 0.5$ for the boosting. 138 trees were created with a depth of 2 separations. The minimum number of events in a node was set to 15% of the initial training sample. The separation was performed using the gini index with $nCut = 20$.

The BDT response is reported in fig. 5.29, normalised at the number of expected events shown in table 4.5. The background distribution is completely overlapped

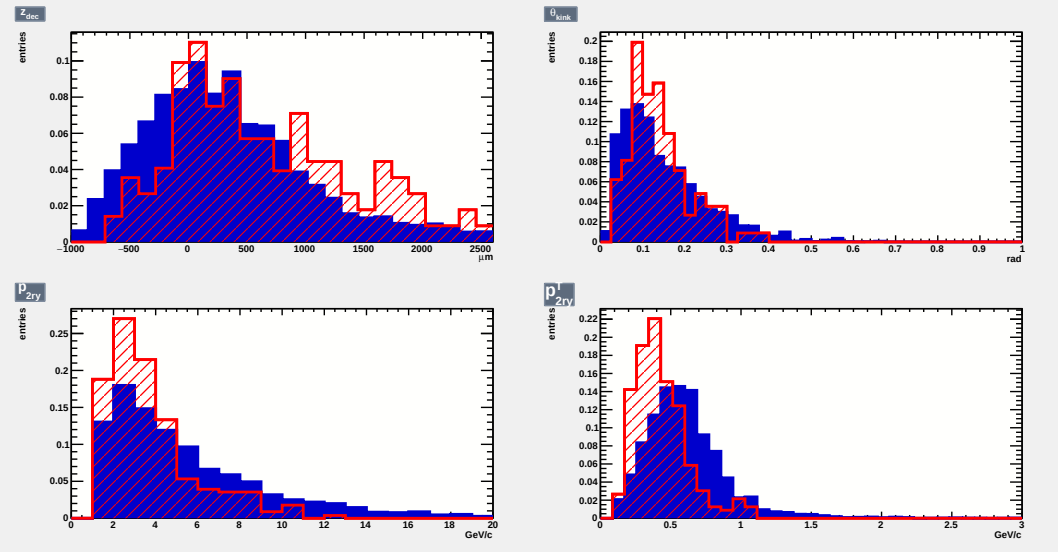

Figure 5.28. Distribution of the kinematical variables used for the BDT analysis in the $\tau \to e$ decay channel

to the signal one, therefore the BDT does not discriminate more than the counting method.

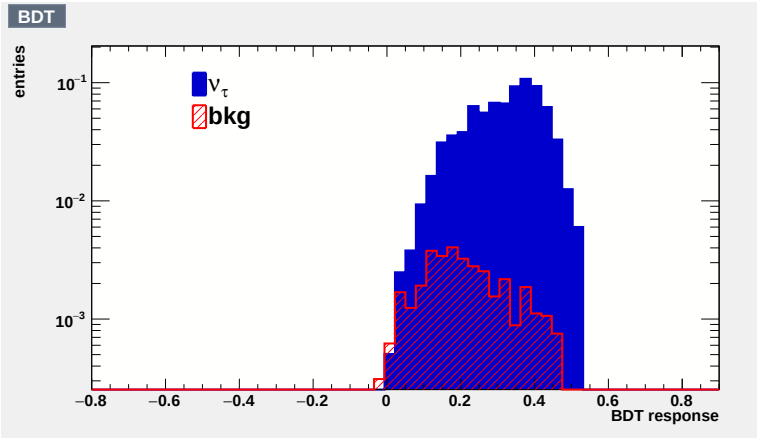

Figure 5.29. BDT response for $\tau \to e$ decay channel. The logarithmic scale has been used

5.11 Overall Significance

The discriminating power of the BDT analysis can be used to compute the overall significance of ν_τ appearance with the extended analysis using the Likelihood method.

The significance of the observation of 10 ν_τ candidates is evaluated as the probability that background not only can produce a number of events larger than or equal to the measured data, but also has the features which are signal-like or background-like as the observed ones, according to the BDT response. Therefore, for each decay channel, the Poisson distribution of the observed events has been combined with the probability density function $f(BDT)$ given by the BDT response for background. The extended likelihood function is:

$$\mathcal{L} = \prod_{ch=1}^{4} \left(\frac{b_{ch}^{n_{ch}} e^{-b_{ch}}}{n_{ch}!} \cdot \prod_{i=1}^{n_{ch}} f(BDT_{ch_i}) \right) \tag{5.11.1}$$

where, for each pseudo-experiment, ch is the index over the 4 decay channels, i is the index over the number of observed events n_{ch} in that channel, b_{ch} is the expected background in the ch^{th} decay channel.

The P-value is defined as the probability that background fluctuations have $-2\ln\mathcal{L} > -2\ln\mathcal{L}^*$, where $\mathcal{L}^*$ is the measured value. 205 pseudo-experiments over 692192181 have $-2\ln\mathcal{L} > -2\ln\mathcal{L}^*$, as it can be seen in fig. 5.30, so the P-value is $2.96 \cdot 10^{-7}$, corresponding to a significance of 5.0σ.

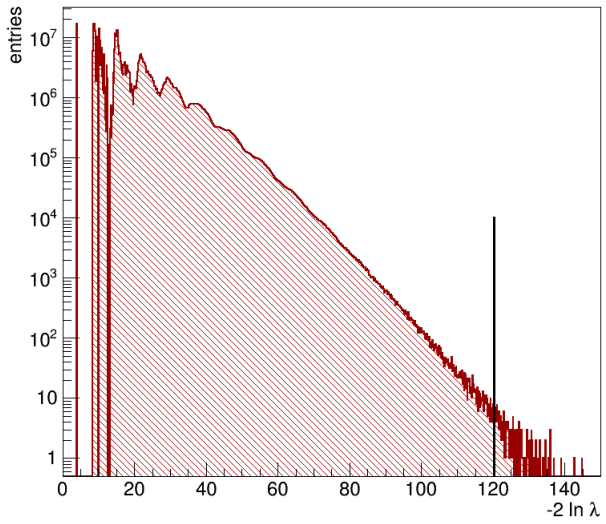

Figure 5.30. Likelihood function for overall ν_τ appearance significance evaluation. The measured value for the data is indicated with a line

Conclusions

The OPERA experiment played the key role of demonstrating unambiguously the $\nu_\mu \to \nu_\tau$ oscillation. It took data from 2008 to 2012, integrating a beam intensity of 1.8×10^{20} protons on target. Five ν_τ candidates were found satisfying stringent kinematical cuts, with 0.25 expected events of background: the absence of signal was excluded with a significance of 5.1σ, thus claiming the discovery of $\nu_\mu \to \nu_\tau$ oscillation in the CNGS beam [2]. I contributed to the validation of the fifth ν_τ candidate, in the Naples emulsion Laboratory, with a specific analysis for large angle track search ($\tan\theta \leq 3$ rad) that I had implemented, meant to strongly suppress the hadron re-interaction background hypothesis.

Given the full Monte Carlo validation with data in all corners of the parameter space, a likelihood approach is well justified and therefore the Collaboration has decided to define a new strategy with looser cuts for the selection of ν_τ candidates. Looser cuts have the advantage of reducing the statistical uncertainty on the measurement of Δm^2_{23}.
I defined a new strategy for the ν_τ selection, replacing the stringent kinematical cuts with minimum bias ones, optimised to minimise the statistical uncertainty on the measurements. Applying these criteria, 6.5 ν_τ candidates and 2.0 background events are expected.
At the end of data taking, 5603 neutrino events had been fully analysed and have been used for this analysis. Within this sample, 10 ν_τ candidate events satisfied the minimum bias criteria.

The number of observed ν_τ candidates after background subtraction is a function of $\sigma^{CC}_{\nu_\tau} \cdot \Delta m^2_{23}$. Assuming the maximal mixing $\sin^2 2\theta_{23} = 1$ and fixing $\sigma^{CC}_{\nu_\tau}$ to the SM value it is possible to measure Δm^2_{23}, while fixing Δm^2_{23} to the present global best fit it is possible to measure $\sigma^{CC}_{\nu_\tau}$.

The measurement of Δm^2_{23}, done for the first time in appearance mode, is $2.8 \pm 0.6 \cdot 10^{-3}$ eV^2 at 68% C.L. The result is consistent within 1σ with the measurements done in disappearance mode by other experiments and with the PDG 2016 best fit [109].

σ_{ν_τ} is proportional to the energy, with a constant term $\sigma^0_{\nu_\tau}$ and a kinematic

suppression factor K(E), which takes into account the suppression due to the heavier τ lepton mass. I did the first ever evaluation of $\sigma^0_{\nu_\tau}$, so far measured only by the DONuT experiment, with no separation between ν_τ and $\bar{\nu}_\tau$ [3]. It results to be $(8^{+4}_{-3}) \cdot 10^{-39}$ cm^2 GeV^{-1}, compatible with the Standard Model prediction within 1σ.

To perform signal to background separation, I used the Boosted Decision Tree (BDT) method, a multivariate machine learning method used to classify observations. With this analysis, two events in the $\tau \to 1h$ decay channel were classified as background-like, in agreement with expectations, while the other eight were signal-like.

Combining the Poisson counting method and BDT results in the $\tau \to \mu$ decay channel, including also the background due to the $\bar{\nu}_\mu$ beam contamination, I have obtained the first observation of the leptonic number with τ neutrinos with a significance of more than 3σ.

Finally, I evaluated the significance of the observation of neutrino oscillations with this new analysis using three different approaches: the first one based on Poisson statistics and p-values, the second one on the likelihood ratio and the third one combining in the extended likelihood function the Poisson statistics and the BDT probability density functions. All results lead to a significance above 5σ.

Appendix A

Multivariate Analysis

The analysis based on the statistical principle of multivariate statistics is called Multivariate analysis (MVA). It involves the analysis of several statistical outcome variables at the same time.

A multivariate classifier is a class of "supervised learning" algorithms which makes use of training events, for which the desired output is known, to determine the mapping function that describes a decision boundary (classification) or an approximation of the underlying functional behaviour defining the target value (regression). The mapping function can contain various degrees of approximations and it may be a single global function or a set of local models.

In this thesis, the Toolkit for Multivariate Analysis (TMVA) provided by ROOT-integrated environment [125] has been used. TMVA is specifically designed for high-energy physics applications.

A.1 Boosted Decision Tree

The Boost Decision Trees (BDT) is a MVA machine learning method used to classify observations. It is based on trees of binary choices taken on one single variable at a time until a stop criterion is fulfilled.

The decision tree strategy originated in the 80's from the field of pattern recognition. Since then, several methods focusing on the improvement of performances and reliability have been exploited, such as the *Boosting* method, which formed the Boosted Decision Tree.

Nowadays, BDT has many applications in the financial analysis, medical diagnostics and pattern recognition. In high energy physics, however, the method is relatively new and it was first used by the MiniBooNE experiment for particle identification [141, 142]. Recently, many analyses, especially in the Large Hadron Collider

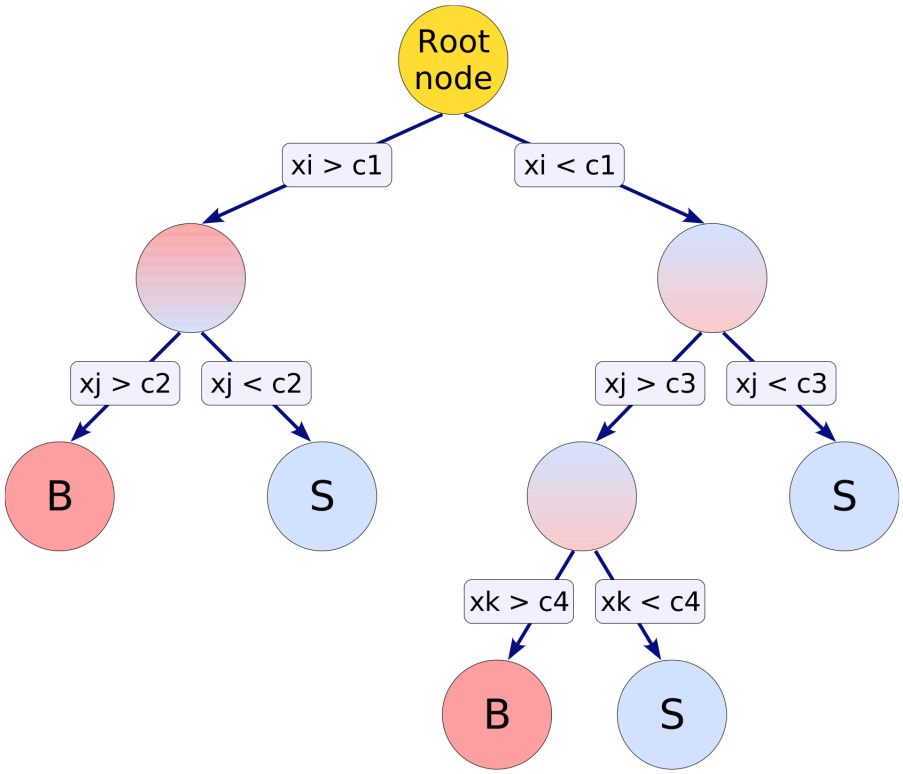

Figure A.1. Schematic view of a decision tree

experiments, have been performed using this method.

A.1.1 Decision Tree

The decision tree is a binary tree classifier, since the target variable is binary, taking a value of either 1 (true) or 0 (false).
To apply the method, Monte-Carlo samples are equally divided into training and testing samples. This can be set by even/odd separation or it can be done randomly.

A sequential series of rectangular cuts which split the data into *nodes* and *leaves* is applied to the training sample. Whereas a cut-based analysis is able to select only one hypercube of the phase space, the decision tree is able to split the phase space into a large number of hypercubes. An example of a decision tree and the splitting process is illustrated in figure A.1.

The initial node is referred as the *root node* and contains all the events and an associated cut variable characterizing the event. This cut splits the node into two daughter nodes. Repeated left/right (yes/no) decisions are taken on one single

variable at a time until a stop criterion is fulfilled. The split for each node is defined by assessing the cut values for each variable giving the best signal over background separation. According to the amount of events in the final node (leaf), they are classified as signal-like or background-like.

The splitting is based on the following criterion:

$$\text{Gini}_{root} = \text{Gini}_{left\ daughter} - \text{Gini}_{right\ daughter} \tag{A.1.1}$$

where Gini$= P(1-P)$ and P stands for purity:

$$P = \frac{\sum_i W_i^s}{\sum_i W_i^s + \sum_j W_j^b} \tag{A.1.2}$$

with W^s weight of signal events and W^b that of background events.

The splitting process continues on the daughter nodes with a different cut variable for each step. Decision whether to stop the splitting or not depends either on the remaining events in the node or on the predefined number of splittings. The node that is not split anymore is called a *leaf*. Moreover, if a leaf has a purity higher than 0.5 or a pre-defined value, it is called *signal leaf*, otherwise, *background leaf*.

Since the splitting criterion is always a cut on a single variable, the training procedure selects the variable and cut value that optimises the increase in the separation index between the parent node and the sum of the indices of the two daughter nodes, weighted by their relative fraction of events. The cut values are optimised by scanning over the variable range with a granularity, namely a number of cuts ($nCut$) that can be set. It has been proved that $nCuts = 20$ is a good compromise between computing time and step size. Finer stepping values do not increase noticeably the performance of the BDTs. If $nCuts = -1$, an algorithm that tests all possible cuts on the training sample and finds the best one will be invoked.

The BDT response is a value between 1, that defines signal-like events, and -1, which defines background-like events.

A.1.2 Boosting

A Boosted Decision Tree classifier consists of a *forest* of the decision trees described in the previous section. A single tree, indeed, has a limited discrimination power and is highly susceptible to over-training. To go beyond this problem, many decision trees $(t_1, t_2, t_3, \ldots, t_n)$ can be created and combined into a stronger classifier. This process is called *Boosting* and increases the performance and the statistical robustness of the group of model. It is based on the re-weighting of all the misclassified events and the creation a new decision tree. With this method the learning process gets more

stable and the combined discriminating output gets smoother compared to a single decision tree.

Different types of boosting exist, such as Adaptive Boost, which is the default one, and Gradient Boost (BDTG). The AdaBoost method will be now described in detail.

AdaBoost

A first decision tree is created using the training sample. For each tree, the misclassification rate is calculated as follows, using the weighted sum of the misclassified events in each leaf, over the initial weight of all training sample:

$$\alpha_n = \beta \times \ln \frac{1 - \epsilon_n}{\epsilon_n} \tag{A.1.3}$$

with β the boosting parameter. The misclassified events are weighted with the factor e^{α_n}, so that misclassified events in the current decision tree will have higher weights in the next tree. A new tree is then created from the boosted sample. Since the misclassified events have a higher weight from the previous training, the algorithm works harder on them. Repeating these steps, a forest made of N decision trees is created.
The final BDT result for an event x is obtained with the following equation:

$$D(x) = \frac{1}{\sum_{n=1}^{N} \alpha_n} \sum_{n=1}^{N} \alpha_n D_n(x) \tag{A.1.4}$$

where $D_n(x)$ is the n^{th} decision tree output for the i^{th} event.

A.1.3 Graphical Results

In the following, graphical and numerical procedures used in the thesis will be described.

Input variable distribution: the normalized distribution of all input variables for signal and background is calculated. An example is shown in figure A.2 (a). This helps to understand whether a variable is useful or not to distinguish between signal and background.

Correlations between input variables: the correlations between variables is shown thanks to two matrices, one for signal and another one for background. An example is shown in figure A.2 (b).

Overtraining check: the test is performed dividing the MC sample in two groups: one is used for training, the other one to obtain an independent output spectrum. If test and training samples have the same output distributions, the algorithm is not overtrained. The compatibility is performed using the Kolmogorov-Smirnov test. To have no overtraining, a good overlap between testing and training sample is needed, as obtained in figure A.2 (c). Usually, overtraining occurs when a machine learning problem has too few degrees of freedom, because too many model parameters of an algorithm were adjusted to too few data points.

Receiver Operating Characteristic (ROC) curve: the ROC curve describes the efficiency of the BDT method and displays the background rejection versus the signal efficiency. A good ROC curve lies in the upper right corner. Moreover, the integral over this curve gives a numerical statement. The BDT is more efficient as much as the numerical statement is closer to one. This can be used also to compare different MVA methods, as it has been done in figure A.2 (d).

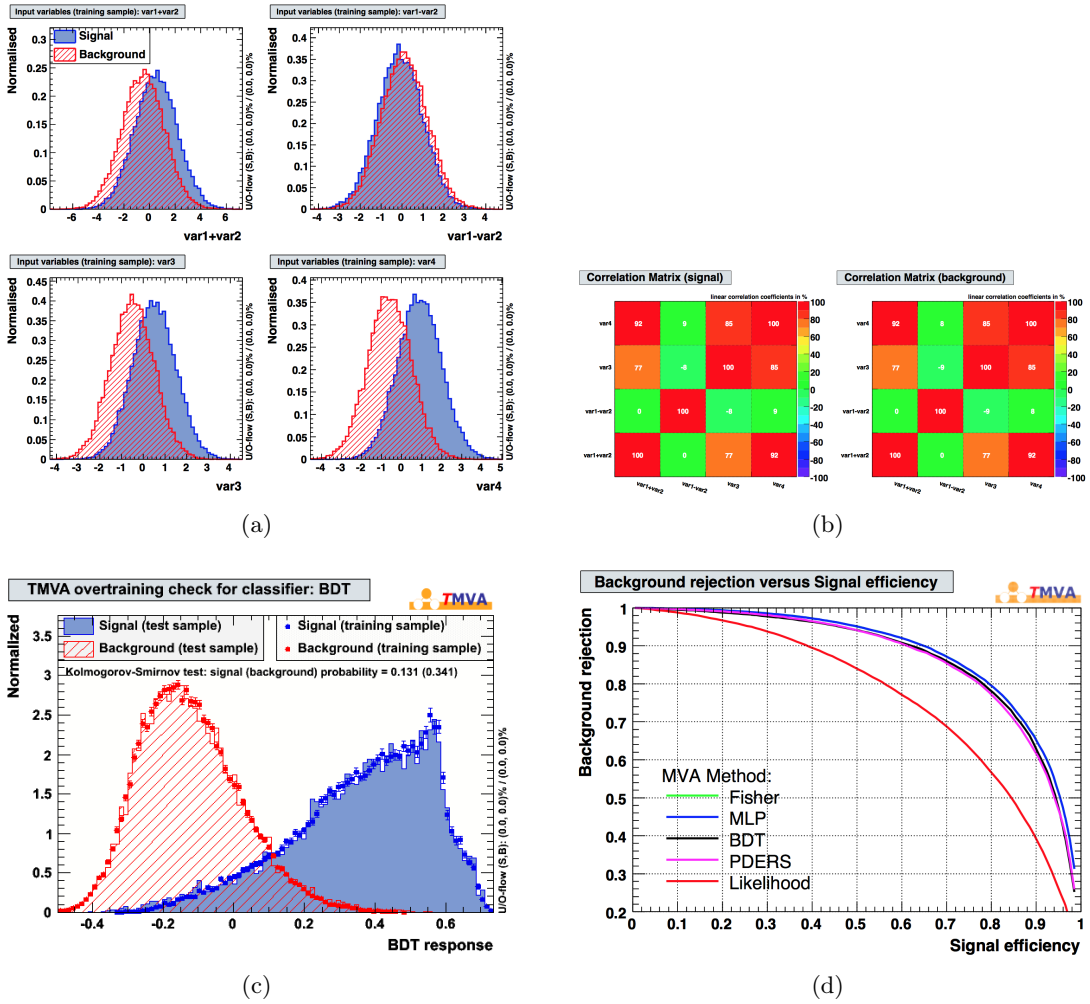

Figure A.2. BDT evaluation plots obtained via the TMVA toolkit: (a): input variable distribution; (b): correlation matrix; (c): overtraining check; (d): ROC curve

Appendix B

Efficiencies evaluation

Efficiencies of the analysis chain were estimated using the Monte Carlo simulation, going through all the steps described in Section 4.2.

Signal events have been weighted for the oscillation probabilities. Efficiencies for the DIS and QE signal interactions, in case of long and short decays, have been estimated separately. To evaluate the efficiencies for the charm background, events have been weighted for the hadronization fractions reported in table 2.4. In addition, the ν_μ CC and ν_μ NC efficiencies, used for the evaluation of the number of expected events, have been estimated separately for the 1μ and 0μ classification.

In the tables, "BF" stands for Brick Finding, "CS" for Changeable Sheets, "SB" for Scan-Back, "LOC" for Location and "DS" for Decay Search. "Kinematical Selection" refers to the cuts reported in table 3.2 and "Minimum Bias" to the cuts reported in table 4.3.

Table B.1. Efficiencies for $\tau \to 1h$ decay channel, DIS interactions, long decays

Step	Events	Oscillated	Efficiency
Total events	21414	198.11	100.00 ± 0.00
Electronic Detector Trigger	21414	198.11	100.00 ± 0.00
Event Classification	13579	156.81	79.16 ± 0.33
OpCarac	13139	151.26	76.35 ± 0.33
BF	11513	130.84	66.04 ± 0.34
CS	10335	110.29	55.67 ± 0.34
SB	9565	99.00	49.97 ± 0.34
LOC	9109	94.44	47.67 ± 0.34
DS	4961	49.29	24.88 ± 0.29
Topology	4961	49.29	24.88 ± 0.29
Minimum Bias	3375	35.56	17.95 ± 0.25
Kinematical Selection	1058	12.14	6.13 ± 0.15

Table B.2. Efficiencies for $\tau \to 1h$ decay channel, DIS interactions, short decays

Step	Events	Oscillated	Efficiency
Total events	17696	254.87	100.00 ± 0.00
Electronic Detector Trigger	17696	254.87	100.00 ± 0.00
Event Classification	12388	203.83	79.97 ± 0.34
OpCarac	11938	196.40	77.06 ± 0.35
BF	10502	169.09	66.35 ± 0.37
CS	9368	140.11	54.97 ± 0.38
SB	8770	127.79	50.14 ± 0.38
LOC	8347	121.35	47.61 ± 0.38
DS	2684	34.61	13.58 ± 0.27
Topology	2684	34.61	13.58 ± 0.27
Minimum Bias	1821	22.94	9.00 ± 0.23
Kinematical Selection	0	0.00	0.00 ± 0.00

Table B.3. Efficiencies for $\tau \to 1h$ decay channel, QE interactions, long decays

Step	Events	Oscillated	Efficiency
Total events	4987	107.10	100.00 ± 0.00
Electronic Detector Trigger	4978	106.79	99.72 ± 0.06
Event Classification	4183	94.88	88.59 ± 0.52
OpCarac	3971	89.80	83.85 ± 0.57
BF	2774	64.39	60.12 ± 0.70
CS	1072	17.88	16.69 ± 0.58
SB	892	14.73	13.75 ± 0.54
LOC	843	13.68	12.78 ± 0.53
DS	293	4.39	4.10 ± 0.33
Topology	293	4.39	4.10 ± 0.33
Minimum Bias	200	3.17	2.96 ± 0.28
Kinematical Selection	59	0.87	0.81 ± 0.15

Table B.4. Efficiencies for $\tau \to \mu$ decay channel, DIS interactions, long decays

Step	Events	Oscillated	Efficiency
Total events	12186	113.67	100.00 ± 0.00
Electronic Detector Trigger	12186	113.67	100.00 ± 0.00
Event Classification	11585	105.99	93.24 ± 0.20
OpCarac	11297	103.21	90.80 ± 0.24
BF	7756	84.73	74.54 ± 0.44
CS	6374	60.93	53.60 ± 0.45
SB	6240	59.47	52.32 ± 0.45
LOC	5893	56.33	49.56 ± 0.45
DS	3416	31.46	27.67 ± 0.41
Topology	3416	31.46	27.67 ± 0.41
Minimum Bias	2701	26.61	23.41 ± 0.38
Kinematical Selection	1919	20.79	18.29 ± 0.33

Table B.5. Efficiencies for $\tau \to \mu$ decay channel, DIS interactions, short decays

Step	Events	Oscillated	Efficiency
Total events	9981	143.59	100.00 ± 0.00
Electronic Detector Trigger	9981	143.59	100.00 ± 0.00
Event Classification	9261	131.03	91.26 ± 0.26
OpCarac	9028	126.95	88.41 ± 0.29
BF	7251	106.05	73.86 ± 0.45
CS	5994	75.83	52.81 ± 0.49
SB	5854	73.53	51.21 ± 0.49
LOC	5562	69.71	48.55 ± 0.50
DS	1852	20.96	14.60 ± 0.39
Topology	1852	20.96	14.60 ± 0.39
Minimum Bias	1459	16.60	11.56 ± 0.35
Kinematical Selection	0	0.00	0.00 ± 0.00

Table B.6. Efficiencies for $\tau \to \mu$ decay channel, QE interactions, long decays

Step	Events	Oscillated	Efficiency
Total events	6062	127.67	100.00 ± 0.00
Electronic Detector Trigger	6060	127.57	99.92 ± 0.02
Event Classification	5798	119.81	93.84 ± 0.26
OpCarac	5527	114.53	89.71 ± 0.36
BF	4381	99.96	78.30 ± 0.57
CS	2395	43.19	33.83 ± 0.63
SB	2373	42.74	33.47 ± 0.63
LOC	2254	40.56	31.77 ± 0.62
DS	786	12.78	10.01 ± 0.43
Topology	786	12.78	10.01 ± 0.43
Minimum Bias	660	11.18	8.76 ± 0.40
Kinematical Selection	464	7.97	6.24 ± 0.34

Table B.7. Efficiencies for $\tau \to 3h$ decay channel, DIS interactions, long decays

Step	Events	Oscillated	Efficiency
Total events	20274	193.56	100.00 ± 0.00
Electronic Detector Trigger	20274	193.56	100.00 ± 0.00
Event Classification	9870	126.76	65.49 ± 0.35
OpCarac	9535	122.42	63.25 ± 0.35
BF	8383	106.12	54.83 ± 0.35
CS	8067	99.14	51.22 ± 0.34
SB	7921	96.88	50.05 ± 0.34
LOC	7515	91.93	47.50 ± 0.34
DS	6225	74.79	38.64 ± 0.32
Topology	6224	74.78	38.63 ± 0.32
Minimum Bias	5268	66.49	34.35 ± 0.31
Kinematical Selection	2924	38.18	19.72 ± 0.25

Table B.8. Efficiencies for $\tau \to 3h$ decay channel, DIS interactions, short decays

Step	Events	Oscillated	Efficiency
Total events	17486	261.03	100.00 ± 0.00
Electronic Detector Trigger	17486	261.03	100.00 ± 0.00
Event Classification	10168	174.61	66.89 ± 0.37
OpCarac	9841	168.94	64.72 ± 0.38
BF	8718	146.17	56.00 ± 0.38
CS	8365	135.94	52.08 ± 0.38
SB	8201	132.74	50.85 ± 0.38
LOC	7780	125.50	48.08 ± 0.38
DS	3831	54.93	21.04 ± 0.31
Topology	3826	54.82	21.00 ± 0.31
Minimum Bias	3215	44.83	17.17 ± 0.29
Kinematical Selection	1757	25.54	9.79 ± 0.23

Table B.9. Efficiencies for $\tau \to 3h$ decay channel, QE interactions, long decays

Step	Events	Oscillated	Efficiency
Total events	5857	123.89	100.00 ± 0.00
Electronic Detector Trigger	5857	123.89	100.00 ± 0.00
Event Classification	3778	90.82	73.31 ± 0.63
OpCarac	3667	87.96	71.00 ± 0.63
BF	2907	69.86	56.39 ± 0.65
CS	2650	57.91	46.74 ± 0.65
SB	2567	55.80	45.04 ± 0.65
LOC	2431	52.39	42.29 ± 0.64
DS	1732	36.20	29.22 ± 0.60
Topology	1732	36.20	29.22 ± 0.60
Minimum Bias	1612	34.79	28.08 ± 0.58
Kinematical Selection	1369	30.03	24.24 ± 0.55

Table B.10. Efficiencies for $\tau \to e$ decay channel, DIS interactions, long decays

Step	Events	Oscillated	Efficiency
Total events	16996	173.01	100.00 ± 0.00
Electronic Detector Trigger	16988	172.87	99.92 ± 0.02
Event Classification	13441	157.88	91.26 ± 0.31
OpCarac	12818	148.23	85.68 ± 0.33
BF	11205	126.42	73.07 ± 0.36
CS	9510	95.22	55.04 ± 0.38
SB	8333	76.93	44.47 ± 0.38
LOC	7938	73.08	42.24 ± 0.38
DS	3309	32.13	18.57 ± 0.30
Topology	3309	32.13	18.57 ± 0.30
Minimum Bias	2488	26.30	15.20 ± 0.27
Kinematical Selection	2206	24.75	14.31 ± 0.26

Table B.11. Efficiencies for $\tau \to e$ decay channel, DIS interactions, short decays

Step	Events	Oscillated	Efficiency
Total events	15209	247.72	100.00 ± 0.00
Electronic Detector Trigger	15200	247.48	99.90 ± 0.02
Event Classification	12446	224.13	90.48 ± 0.31
OpCarac	11790	207.82	83.89 ± 0.34
BF	10282	176.12	71.10 ± 0.38
CS	8474	125.47	50.65 ± 0.40
SB	7256	98.69	39.84 ± 0.41
LOC	6894	93.45	37.72 ± 0.40
DS	1932	25.68	10.37 ± 0.27
Topology	1932	25.68	10.37 ± 0.27
Minimum Bias	1389	17.37	7.01 ± 0.23
Kinematical Selection	1319	16.87	6.81 ± 0.23

Table B.12. Efficiencies for $\tau \to e$ decay channel, QE interactions, long decays

Step	Events	Oscillated	Efficiency
Total events	3090	65.05	100.00 ± 0.00
Electronic Detector Trigger	3077	64.63	99.35 ± 0.12
Event Classification	3053	64.13	98.58 ± 0.20
OpCarac	2777	57.47	88.34 ± 0.54
BF	2346	48.35	74.32 ± 0.77
CS	1592	28.82	44.29 ± 0.90
SB	1016	15.92	24.47 ± 0.85
LOC	995	15.51	23.84 ± 0.84
DS	187	2.84	4.36 ± 0.43
Topology	187	2.84	4.36 ± 0.43
Min bias	149	2.46	3.78 ± 0.39
Kinematical Selection	109	2.09	3.22 ± 0.33

Table B.13. Efficiencies for $charm \rightarrow 1h$ decay channel, DIS interactions, long decays

Step	Events	Weighted	Efficiency
Total events	31891	10470.06	100.00 ± 0.00
Electronic Detector Trigger	31891	10470.06	100.00 ± 0.00
Event Classification	9104	1922.52	18.36 ± 0.25
OpCarac	8737	1844.10	17.61 ± 0.25
BF	7782	1637.08	15.64 ± 0.24
CS	7189	1503.79	14.36 ± 0.23
SB	6782	1417.41	13.54 ± 0.23
LOC	6436	1343.87	12.84 ± 0.22
DS	3751	779.58	7.45 ± 0.18
Topology	1063	238.14	2.27 ± 0.10
Minimum Bias	334	74.81	0.71 ± 0.06
Kinematical Selection	87	17.16	0.16 ± 0.03

Table B.14. Efficiencies for $charm \rightarrow 1h$, short decays

Step	Events	Weighted	Efficiency
Total events	33093	11500.17	100.00 ± 0.00
Electronic Detector Trigger	33093	11500.17	100.00 ± 0.00
Event Classification	9393	2210.18	19.22 ± 0.25
OpCarac	8945	2102.79	18.28 ± 0.24
BF	7733	1806.08	15.70 ± 0.23
CS	6525	1504.82	13.09 ± 0.22
SB	6164	1422.35	12.37 ± 0.21
LOC	5825	1343.13	11.68 ± 0.21
DS	2013	457.61	3.98 ± 0.13
Topology	608	148.73	1.29 ± 0.07
Kinematical Selection	0	0.00	0.00 ± 0.00
Min bias	163	39.00	0.34 ± 0.04

Table B.15. Efficiencies for *charm* $\rightarrow \mu$ decay channel, DIS interactions, long decays

Step	Events	Weighted	Efficiency
Total events	11044	2795.47	100.00 ± 0.00
Electronic Detector Trigger	11044	2795.47	100.00 ± 0.00
Event Classification	10779	2724.55	97.46 ± 0.15
OpCarac	10608	2681.22	95.91 ± 0.19
BF	7498	1902.28	68.05 ± 0.44
CS	6798	1729.99	61.89 ± 0.46
SB	6644	1692.38	60.54 ± 0.47
LOC	6278	1594.95	57.05 ± 0.47
DS	3280	857.97	30.69 ± 0.43
Topology	3280	857.97	30.69 ± 0.43
Minimum Bias	31	8.69	0.31 ± 0.05
Kinematical Selection	12	3.46	0.12 ± 0.03

Table B.16. Efficiencies for *charm* $\rightarrow \mu$ decay channel, DIS interactions, short decays

Step	Events	Weighted	Efficiency
Total events	9958	2870.82	100.00 ± 0.00
Electronic Detector Trigger	9958	2870.82	100.00 ± 0.00
Event Classification	9728	2803.37	97.65 ± 0.15
OpCarac	9571	2757.70 96.06 ± 0.19	
BF	6578	1904.35	66.33 ± 0.47
CS	5746	1671.57	58.23 ± 0.50
SB	5650	1645.21	57.31 ± 0.50
LOC	5337	1554.17	54.14 ± 0.50
DS	2034	606.45	21.12 ± 0.40
Topology	2034	606.45	21.12 ± 0.40
Minimum Bias	12	3.62	0.001 ± 0.03
Kinematical Selection	0	0.00	0.00 ± 0.00

Table B.17. Efficiencies for $charm \to 3h$ decay channel, DIS interactions, long decays

Step	Events	Weighted	Efficiency
Total events	31891	10470.06	100.00 ± 0.00
Electronic Detector Trigger	31891	10470.06	100.00 ± 0.00
Event Classification	9104	1922.52	18.36 ± 0.25
OpCarac	8737	1844.10	17.61 ± 0.25
BF	7782	1637.08	15.64 ± 0.24
CS	7189	1503.79	14.36 ± 0.23
SB	6782	1417.41	13.54 ± 0.23
LOC	6436	1343.87	12.84 ± 0.22
DS	3751	779.58	7.45 ± 0.18
Topology	2688	541.43	5.17 ± 0.16
Minimum Bias	1110	222.93	2.13 ± 0.10
Kinematical Selection	514	104.95	1.00 ± 0.07

Table B.18. Efficiencies for $charm \to 3h$ decay channel, DIS interactions, short decays

Step	Events	Weighted	Efficiency
Total events	33093	11500.17	100.00 ± 0.00
Electronic Detector Trigger	33093	11500.17	100.00 ± 0.00
Event Classification	9393	2210.18	19.22 ± 0.25
OpCarac	8945	2102.79	18.28 ± 0.24
BF	7733	1806.08	15.70 ± 0.23
CS	6525	1504.82	13.09 ± 0.22
SB	6164	1422.35	12.37 ± 0.21
LOC	5825	1343.13	11.68 ± 0.21
DS	2013	457.61	3.98 ± 0.13
Topology	1405	308.88	2.69 ± 0.11
Minimum Bias	487	106.22	0.92 ± 0.07
Kinematical Selection	215	49.62	0.43 ± 0.04

Table B.19. Efficiencies for $charm \rightarrow e$ decay channel, DIS interactions, long decays

Step	Events	Weighted	Efficiency
Total events	31891	10470.06	100.00 ± 0.00
Electronic Detector Trigger	31891	10470.06	100.00 ± 0.00
Event Classification	1232	262.44	2.51 ± 0.11
OpCarac	1167	248.81	2.38 ± 0.11
BF	1046	223.16	2.13 ± 0.10
CS	903	191.78	1.83 ± 0.09
SB	789	167.48	1.60 ± 0.09
LOC	753	159.53	1.52 ± 0.09
DS	289	60.83	0.58 ± 0.05
Topology	288	60.58	0.58 ± 0.05
Minimum Bias	85	18.08	0.17 ± 0.03
Kinematical Selection	85	18.08	0.17 ± 0.03

Table B.20. Efficiencies for $charm \rightarrow e$ decay channel, DIS interactions, short decays

Step	Events	Weighted	Efficiency
Total events	33093	11500.17	100.00 ± 0.00
Electronic Detector Trigger	33093	11500.17	100.00 ± 0.00
Event Classification	742	163.59	1.42 ± 0.08
OpCarac	705	155.05	1.35 ± 0.08
BF	605	132.37	1.15 ± 0.07
CS	468	101.95	0.89 ± 0.06
SB	380	83.19	0.72 ± 0.06
LOC	361	78.75	0.68 ± 0.06
DS	96	20.72	0.18 ± 0.03
Topology	95	20.50	0.18 ± 0.03
Minimum Bias	30	6.37	0.06 ± 0.02
Kinematical Selection	30	6.37	0.06 ± 0.02

Table B.21. Efficiencies for $\nu_\mu CC \quad 1\mu$

Total events	42041	42041.00	100.00 ± 0.00
Electronic Detector Trigger	42041	42041.00	100.00 ± 0.00
Event Classification	40012	40012.00	95.17 ± 0.10
OpCarac	39031	39031.00	92.84 ± 0.13
BF	24201	24201.00	57.57 ± 0.24
CS	21117	21117.00	50.23 ± 0.24
SB	20734	20734.00	49.32 ± 0.24
LOC	19537	19537.00	46.47 ± 0.24
Topology	913	913.00	2.17 ± 0.07

Table B.22. Efficiencies for $\nu_\mu CC \quad 0\mu$

Total events	42041	42041.00	100.00 ± 0.00
Electronic Detector Trigger	42041	42041.00	100.00 ± 0.00
Event Classification	2029	2029.00	4.83 ± 0.10
OpCarac	1927	1927.00	4.58 ± 0.10
BF	1645	1645.00	3.91 ± 0.09
CS	1431	1431.00	3.40 ± 0.09
SB	1333	1333.00	3.17 ± 0.09
LOC	1257	1257.00	2.99 ± 0.08
Topology	1257	1257.00	2.99 ± 0.08

Table B.23. Efficiencies for $\nu_\mu NC \quad 1\mu$

Total events	10869	10869.00	100.00 ± 0.00
Electronic Detector Trigger	10852	10852.00	99.84 ± 0.04
Event Classification	8612	8612.00	79.23 ± 0.39
OpCarac	8022	8022.00	73.81 ± 0.42
BF	6135	6135.00	56.44 ± 0.48
CS	4034	4034.00	37.11 ± 0.46
SB	3521	3521.00	32.39 ± 0.45
LOC	3312	3312.00	30.47 ± 0.44
Topology	3312	3312.00	30.47 ± 0.44

Table B.24. Efficiencies for $\nu_\mu NC \quad 0\mu$

Total events	10869	10869.00	100.00 ± 0.00
Electronic Detector Trigger	10852	10852.00	99.84 ± 0.04
Event Classification	2240	2240.00	20.61 ± 0.39
OpCarac	2144	2144.00	19.73 ± 0.38
BF	1799	1799.00	16.55 ± 0.36
CS	1601	1601.00	14.73 ± 0.34
SB	1549	1549.00	14.25 ± 0.34
LOC	1455	1455.00	13.39 ± 0.33
Topology	383	383.00	3.52 ± 0.18

List of Figures

List of Tables

Bibliography

[1] Y. Fukuda et al. Evidence for oscillation of atmospheric neutrinos. *Phys. Rev. Lett.*, 81:1562–1567, 1998.

[2] N. Agafonova et al. Discovery of τ Neutrino Appearance in the CNGS Neutrino Beam with the OPERA Experiment. *Phys. Rev. Lett.*, 115(12):121802, 2015.

[3] K. Kodama et al. Final tau-neutrino results from the DONuT experiment. *Phys. Rev.*, D78:052002, 2008.

[4] J. Chadwick. The intensity distribution in the magnetic spectrum of beta particles from radium (B + C). *Verh. Phys. Gesell.*, 16:383–391, 1914.

[5] Laurie M. Brown. The idea of the neutrino. *Phys. Today*, 31N9:23–28, 1978.

[6] W. Pauli. Letter to a physicist's gathering at tubingen. *Ristampato in: R. Kronig, V. Weisskopf (Eds.), W. Pauli, Collected Scientific Papers, Vol. 2, Interscience. New York, 1964*, page 1313, December 4, 1930.

[7] J. Chadwick. Possible Existence of a Neutron. *Nature*, 129:312, 1932.

[8] J. Chadwick. The Existence of a Neutron. *Proc. Roy. Soc. Lond.*, A136(830):692–708, 1932.

[9] E. Fermi. An attempt of a theory of beta radiation. 1. *Z. Phys.*, 88:161–177, 1934.

[10] H. Bethe and R. Peierls. The 'neutrino'. *Nature*, 133:532, 1934.

[11] Kan Chang Wang. A suggestion on the detection of the neutrino. *Phys. Rev.*, 61:97–97, Jan 1942.

[12] F. Reines and C.L. Cowan. Detection of the free neutrino. *Phys.Rev.*, 92:830–831, 1953.

[13] B. T. Cleveland, Timothy Daily, Raymond Davis, Jr., James R. Distel, Kenneth Lande, C. K. Lee, Paul S. Wildenhain, and Jack Ullman. Measurement of the solar electron neutrino flux with the Homestake chlorine detector. *Astrophys. J.*, 496:505–526, 1998.

[14] F. Reines. The neutrino: From poltergeist to particle. *Rev. Mod. Phys.*, 68:317–327, 1996.

[15] B. Pontecorvo. Electron and Muon Neutrinos. *Sov. Phys. JETP*, 10:1236–1240, 1960. [Zh. Eksp. Teor. Fiz.37,1751(1959)].

[16] G. Danby, J. M. Gaillard, Konstantin A. Goulianos, L. M. Lederman, Nari B. Mistry, M. Schwartz, and J. Steinberger. Observation of High-Energy Neutrino Reactions and the Existence of Two Kinds of Neutrinos. *Phys. Rev. Lett.*, 9:36–44, 1962.

[17] Ezzat G. Bakhoum. Are there 'neutrino flavors'? More on the equation H = mv**2. 2003.

[18] Martin L. Perl et al. Evidence for Anomalous Lepton Production in e+ - e- Annihilation. *Phys. Rev. Lett.*, 35:1489–1492, 1975.

[19] S. Schael et al. Precision electroweak measurements on the Z resonance. *Phys. Rept.*, 427:257–454, 2006.

[20] K. Kodama et al. Observation of tau-neutrino interactions. *Phys. Lett.*, B504:218–224, 2001.

[21] G. P. S. Occhialini and C. F. Powell. Nuclear Disintegrations Produced by Slow Charged Particles of Small Mass. *Nature*, 159:186–190, February 1947.

[22] S. L. Glashow. Partial Symmetries of Weak Interactions. *Nucl. Phys.*, 22:579–588, 1961.

[23] Steven Weinberg. A Model of Leptons. *Phys. Rev. Lett.*, 19:1264–1266, 1967.

[24] Georges Aad et al. Observation of a new particle in the search for the Standard Model Higgs boson with the ATLAS detector at the LHC. *Phys. Lett.*, B716:1–29, 2012.

[25] Serguei Chatrchyan et al. Observation of a new boson at a mass of 125 GeV with the CMS experiment at the LHC. *Phys. Lett.*, B716:30–61, 2012.

[26] M. Goldhaber, L. Grodzins, and A. W. Sunyar. Helicity of Neutrinos. *Phys. Rev.*, 109:1015–1017, 1958.

[27] T. Kajita. Atmospheric neutrino observation in Super-Kamiokande: Evidence for nu/mu oscillations. pages 107–122, 1998.

[28] R. N. Mohapatra et al. Theory of neutrinos: A White paper. *Rept. Prog. Phys.*, 70:1757–1867, 2007.

[29] Takehiko Asaka and Mikhail Shaposhnikov. The νmsm, dark matter and baryon asymmetry of the universe. *Physics Letters B*, 620(12):17 – 26, 2005.

[30] E. Fermi. Trends to a Theory of beta Radiation. (In Italian). *Nuovo Cim.*, 11:1–19, 1934. [,535(1934)].

[31] V. M. Lobashev. The search for the neutrino mass by direct method in the tritium beta-decay and perspectives of study it in the project KATRIN. *Nucl. Phys.*, A719:153–160, 2003.

[32] Ch. Kraus et al. Final results from phase II of the Mainz neutrino mass search in tritium beta decay. *Eur. Phys. J.*, C40:447–468, 2005.

[33] K. Eitel. Direct neutrino mass experiments. *Nucl. Phys. Proc. Suppl.*, 143:197–204, 2005. [,587(2005)].

[34] V. N. Aseev et al. An upper limit on electron antineutrino mass from Troitsk experiment. *Phys. Rev.*, D84:112003, 2011.

[35] K. Assamagan et al. Upper limit of the muon-neutrino mass and charged pion mass from momentum analysis of a surface muon beam. *Phys. Rev.*, D53:6065–6077, 1996.

[36] R. Barate et al. An Upper limit on the tau-neutrino mass from three-prong and five-prong tau decays. *Eur. Phys. J.*, C2:395–406, 1998.

[37] K. N. Abazajian et al. Cosmological and Astrophysical Neutrino Mass Measurements. *Astropart. Phys.*, 35:177–184, 2011.

[38] P. A. R. Ade et al. Planck 2015 results. XIII. Cosmological parameters. *Astron. Astrophys.*, 594:A13, 2016.

[39] B. Pontecorvo. Mesonium and anti-mesonium. *Sov.Phys.JETP*, 6:429, 1957.

[40] Ziro Maki, Masami Nakagawa, and Shoichi Sakata. Remarks on the unified model of elementary particles. *Prog.Theor.Phys.*, 28:870–880, 1962.

[41] V.N. Gribov and B. Pontecorvo. Neutrino astronomy and lepton charge. *Phys.Lett.*, B28:493, 1969.

[42] F. Capozzi, G. L. Fogli, E. Lisi, A. Marrone, D. Montanino, and A. Palazzo. Status of three-neutrino oscillation parameters, circa 2013. *Phys. Rev.*, D89:093018, 2014.

[43] M. C. Gonzalez-Garcia, Michele Maltoni, and Thomas Schwetz. Updated fit to three neutrino mixing: status of leptonic CP violation. *JHEP*, 11:052, 2014.

[44] D. V. Forero, M. Tortola, and J. W. F. Valle. Neutrino oscillations refitted. *Phys. Rev.*, D90(9):093006, 2014.

[45] Stephen F. King and Christoph Luhn. Neutrino Mass and Mixing with Discrete Symmetry. *Rept. Prog. Phys.*, 76:056201, 2013.

[46] L. Wolfenstein. Neutrino Oscillations in Matter. *Phys. Rev.*, D17:2369–2374, 1978.

[47] Carlo Giunti and Alexander Studenikin. Neutrino electromagnetic properties. *Phys. Atom. Nucl.*, 72:2089–2125, 2009.

[48] Boris Kayser. Neutrino physics. *eConf*, C040802:L004, 2004.

[49] John N. Bahcall, Aldo M. Serenelli, and Sarbani Basu. New solar opacities, abundances, helioseismology, and neutrino fluxes. *Astrophys. J.*, 621:L85–L88, 2005.

[50] Raymond Davis, Jr., Don S. Harmer, and Kenneth C. Hoffman. Search for neutrinos from the sun. *Phys. Rev. Lett.*, 20:1205–1209, 1968.

[51] F. Kaether, W. Hampel, G. Heusser, J. Kiko, and T. Kirsten. Reanalysis of the GALLEX solar neutrino flux and source experiments. *Phys. Lett.*, B685:47–54, 2010.

[52] K. S. Hirata et al. Observation of B-8 Solar Neutrinos in the Kamiokande-II Detector. *Phys. Rev. Lett.*, 63:16, 1989.

[53] Y. Suzuki. Kamiokande solar neutrino results. *Nucl. Phys. Proc. Suppl.*, 38:54–59, 1995.

[54] Y. Fukuda et al. Solar neutrino data covering solar cycle 22. *Phys. Rev. Lett.*, 77:1683–1686, 1996.

[55] Y. Fukuda et al. Measurements of the solar neutrino flux from Super-Kamiokande's first 300 days. *Phys. Rev. Lett.*, 81:1158–1162, 1998. [Erratum: Phys. Rev. Lett.81,4279(1998)].

[56] J. Hosaka et al. Solar neutrino measurements in super-Kamiokande-I. *Phys. Rev.*, D73:112001, 2006.

[57] J. P. Cravens et al. Solar neutrino measurements in Super-Kamiokande-II. *Phys. Rev.*, D78:032002, 2008.

[58] K. Abe et al. Solar neutrino results in Super-Kamiokande-III. *Phys. Rev.*, D83:052010, 2011.

[59] M. H. Ahn et al. Measurement of Neutrino Oscillation by the K2K Experiment. *Phys. Rev.*, D74:072003, 2006.

[60] A. Bellerive, J. R. Klein, A. B. McDonald, A. J. Noble, and A. W. P. Poon. The Sudbury Neutrino Observatory. *Nucl. Phys.*, B908:30–51, 2016.

[61] S. N. Ahmed et al. Measurement of the total active B-8 solar neutrino flux at the Sudbury Neutrino Observatory with enhanced neutral current sensitivity. *Phys. Rev. Lett.*, 92:181301, 2004.

[62] P. Alivisatos et al. KamLAND: A Liquid scintillator anti-neutrino detector at the Kamioka site. 1998.

[63] M. P. Decowski. KamLAND's precision neutrino oscillation measurements. *Nucl. Phys.*, B908:52–61, 2016.

[64] F. Capozzi, E. Lisi, A. Marrone, D. Montanino, and A. Palazzo. Neutrino masses and mixings: Status of known and unknown 3ν parameters. *Nucl. Phys.*, B908:218–234, 2016.

[65] Eli Waxman. Extra Galactic sources of high energy neutrinos. *Phys. Scripta*, T121:147–152, 2005.

[66] T. J. Haines et al. Calculation of Atmospheric Neutrino Induced Backgrounds in a Nucleon Decay Search. *Phys. Rev. Lett.*, 57:1986–1989, 1986.

[67] K. S. Hirata et al. Experimental Study of the Atmospheric Neutrino Flux. *Phys. Lett.*, B205:416, 1988. [,447(1988)].

[68] R. M. Bionta et al. Contained Neutrino Interactions in an Underground Water Detector. *Phys. Rev.*, D38:768–775, 1988.

[69] Mayly C. Sanchez et al. Measurement of the L/E distributions of atmospheric neutrinos in Soudan 2 and their interpretation as neutrino oscillations. *Phys. Rev.*, D68:113004, 2003.

[70] S. H. Ahn et al. Detection of accelerator produced neutrinos at a distance of 250-km. *Phys. Lett.*, B511:178–184, 2001.

[71] M. H. Ahn et al. Indications of neutrino oscillation in a 250 km long baseline experiment. *Phys. Rev. Lett.*, 90:041801, 2003.

[72] P. Adamson et al. Combined analysis of ν_μ disappearance and $\nu_\mu \to \nu_e$ appearance in MINOS using accelerator and atmospheric neutrinos. *Phys. Rev. Lett.*, 112:191801, 2014.

[73] M. Apollonio et al. Initial results from the CHOOZ long baseline reactor neutrino oscillation experiment. *Phys. Lett.*, B420:397–404, 1998.

[74] M. Apollonio et al. Search for neutrino oscillations on a long baseline at the CHOOZ nuclear power station. *Eur. Phys. J.*, C27:331–374, 2003.

[75] F. Ardellier et al. Letter of intent for Double-CHOOZ: A Search for the mixing angle theta(13). 2004.

[76] J. K. Ahn et al. RENO: An Experiment for Neutrino Oscillation Parameter θ_{13} Using Reactor Neutrinos at Yonggwang. 2010.

[77] D. A. Dwyer, K. M. Heeger, B. R. Littlejohn, and P. Vogel. Search for Sterile Neutrinos with a Radioactive Source at Daya Bay. *Phys. Rev.*, D87(9):093002, 2013.

[78] K. Abe et al. Indication of Electron Neutrino Appearance from an Accelerator-produced Off-axis Muon Neutrino Beam. *Phys. Rev. Lett.*, 107:041801, 2011.

[79] D. S. Ayres et al. NOvA: Proposal to build a 30 kiloton off-axis detector to study nu(mu) —> nu(e) oscillations in the NuMI beamline. 2004.

[80] Y. Abe et al. Indication for the disappearance of reactor electron antineutrinos in the Double Chooz experiment. *Phys. Rev. Lett.*, 108:131801, 2012.

[81] J. K. Ahn et al. Observation of reactor electron antineutrinos disappearance in the reno experiment. *Phys. Rev. Lett.*, 108:191802, May 2012.

[82] Jiajie Ling. Observation of electron-antineutrino disappearance at Daya Bay. *AIP Conf. Proc.*, 1560:206–210, 2013.

[83] K. Abe et al. Observation of Electron Neutrino Appearance in a Muon Neutrino Beam. *Phys. Rev. Lett.*, 112:061802, 2014.

[84] K. Abe et al. First combined analysis of neutrino and antineutrino oscillations at T2K. 2017.

[85] S. T. Petcov and M. Piai. The LMA MSW solution of the solar neutrino problem, inverted neutrino mass hierarchy and reactor neutrino experiments. *Phys. Lett.*, B533:94–106, 2002.

[86] M. Güler et al. An appearance experiment to search for $\nu_\mu \to \nu_\tau$ oscillations in the CNGS beam: experimental proposal. Technical Report CERN-SPSC-2000-028. LNGS-2000-25. SPSC-P-318, CERN, Geneva, Jul 2000.

[87] H. Shibuya et al. The OPERA emulsion detector for a long baseline neutrino oscillation experiment. 1997.

[88] M. Guler et al. Status report on the OPERA experiment. 2001.

[89] CERN web page: http://proj-cngs.web.cern.ch/proj cngs/. Cngs 2006-2012.

[90] R. Acquafredda et al. The OPERA experiment in the CERN to Gran Sasso neutrino beam. *JINST*, 4:P04018, 2009.

[91] R. Baldy et al. The CERN Neutrino beam to Gran Sasso (NGS). 1999.

[92] A. Ferrari, A. Guglielmi, and P. R. Sala. CNGS neutrino beam systematics for theta(13). *Nucl. Phys. Proc. Suppl.*, 145:93–97, 2005. [,93(2005)].

[93] T. Nakamura et al. The OPERA film: New nuclear emulsion for large-scale, high-precision experiments. *Nucl. Instrum. Meth.*, A556:80–86, 2006.

[94] C. Amsler et al. A new application of emulsions to measure the gravitational force on antihydrogen. *JINST*, 8:P02015, 2013.

[95] E. Barbuto et al. Atmospheric muon flux measurements at the external site of the Gran Sasso Lab. *Nucl. Instrum. Meth.*, A525:485–495, 2004.

[96] Yu. A. Gornushkin. Search for nu/mu —> nu/tau oscillations in appearance mode in the OPERA experiment. *Phys. Part. Nucl.*, 42:553–557, 2011. [Nucl. Phys. Proc. Suppl.218,303(2011)].

[97] N. Agafonova et al. Momentum measurement by the Multiple Coulomb Scattering method in the OPERA lead emulsion target. 2011.

[98] A. Anokhina et al. Emulsion sheet doublets as interface trackers for the OPERA experiment. *JINST*, 3:P07005, 2008.

[99] K. Morishima and T. Nakano. Development of a new automatic nuclear emulsion scanning system, S-UTS, with continuous 3D tomographic image read-out. *JINST*, 5:P04011, 2010.

[100] N. Armenise et al. High-speed particle tracking in nuclear emulsion by last-generation automatic microscopes. *Nucl. Instrum. Meth.*, A551:261–270, 2005.

[101] L. Arrabito et al. Hardware performance of a scanning system for high speed analysis of nuclear emulsions. *Nucl. Instrum. Meth.*, A568:578–587, 2006.

[102] G. Sirri. *Automatic scanning of emulsion films for the OPERA experiment.* PhD thesis, Bologna U., 2003.

[103] T. Adam et al. The OPERA experiment target tracker. *Nucl. Instrum. Meth.*, A577:523–539, 2007.

[104] N. Agafonova et al. Study of neutrino interactions with the electronic detectors of the OPERA experiment. *New J.Phys.*, 13:053051, 2011.

[105] S. Dusini et al. Design and prototype tests of the RPC system for the OPERA spectrometers. *Nucl. Instrum. Meth.*, A508:175–180, 2003.

[106] R. Zimmermann, J. Ebert, C. Hagner, B. Koppitz, V. Savelev, W. Schmidt-Parzefall, J. Sewing, and Y. Zaitsev. The precision tracker of the OPERA detector. *Nucl. Instrum. Meth.*, A555:435–450, 2005. [Erratum: Nucl. Instrum. Meth.A557,690(2006)].

[107] Raoul Zimmermann. A General track reconstruction scheme and its application to the OPERA drift tubes. 2007.

[108] A. Bergnoli et al. The OPERA VETO system. *Nucl. Instrum. Meth.*, A602:653–657, 2009.

[109] C. Patrignani et al. Review of Particle Physics. *Chin. Phys.*, C40(10):100001, 2016.

[110] N. Agafonova et al. Search for $\nu_\mu \to \nu_\tau$ oscillation with the OPERA experiment in the CNGS beam. *New J. Phys.*, 14:033017, 2012.

[111] N. Agafonova et al. Observation of a first ν_τ candidate in the OPERA experiment in the CNGS beam. *Phys.Lett.*, B691:138–145, 2010.

[112] N. Agafonova et al. New results on $\nu_\mu \to \nu_\tau$ appearance with the OPERA experiment in the CNGS beam. 2013.

[113] N. Agafonova et al. Evidence for $\nu_\mu \to \nu_\tau$ appearance in the CNGS neutrino beam with the OPERA experiment. *Phys. Rev.*, D89(5):051102, 2014.

[114] N. Agafonova et al. Observation of tau neutrino appearance in the CNGS beam with the OPERA experiment. *PTEP*, 2014(10):101C01, 2014.

[115] Edmond L. Berger, D. DiBitonto, M. Jacob, and W. James Stirling. The Minimum Invariant Mass: A Technique for Heavy Quark Searches at Collider Energy. *Phys. Lett.*, B140:259–263, 1984.

[116] K. A. Olive et al. Review of Particle Physics. *Chin. Phys.*, C38:090001, 2014.

[117] T. Fukuda, S. Fukunaga, H. Ishida, K. Kodama, T. Matsuo, S. Mikado, S. Ogawa, H. Shibuya, and J. Sudo. Automatic scanning of nuclear emulsions with wide-angle acceptance for nuclear fragment detection. *JINST*, 8:P01023, 2013.

[118] Tsutomu Fukuda. Measurement of charged particle ionisation loss with grain counting in the OPERA emulsion films. *OPERA public note*, 179, 2015.

[119] A. Alexandrov et al. A new fast scanning system for the measurement of large angle tracks in nuclear emulsions. *JINST*, 10(11):P11006, 2015.

[120] Hoecker et al. TMVA: Toolkit for Multivariate Data Analysis. *PoS*, ACAT:040, 2007.

[121] R. A. Fisher. *Statistical Methods for Research Workers*. Cosmo study guides. Cosmo Publications, 1925.

[122] Osamu Sato. A method to combine the P-values of different experiments. *OPERA public note*, 173, July 21, 2014.

[123] Luc Demortier. P Values: What They Are and How to Use Them. *CDF/MEMO/STATISTICS/PUBLIC/8662*, June 13, 2007.

[124] R. Brun, F. Rademakers, and S. Panacek. ROOT, an object oriented data analysis framework. *Conf. Proc.*, C000917:11–42, 2000.

[125] ROOT website: http://root.cern.ch.

[126] J. K. Munro, Jr., J. E. Cleaves, E. L. Williams, Jr., D. J. Nypaver, K. U. Kasemir, and R. D. Meyer. Use of EPICS for high level control of SNS conventional facilities. *eConf*, C011127:TUAP030, 2001. [,131(2001)].

[127] Grigory Rybkin. ATLAS software configuration and build tool optimisation. *J. Phys. Conf. Ser.*, 513:052031, 2014.

[128] C. Andreopoulos et al. The GENIE Neutrino Monte Carlo Generator. *Nucl. Instrum. Meth.*, A614:87–104, 2010.

[129] Costas Andreopoulos, Christopher Barry, Steve Dytman, Hugh Gallagher, Tomasz Golan, Robert Hatcher, Gabriel Perdue, and Julia Yarba. The GENIE Neutrino Monte Carlo Generator: Physics and User Manual. 2015.

[130] Gary J. Feldman and Robert D. Cousins. A Unified approach to the classical statistical analysis of small signals. *Phys. Rev.*, D57:3873–3889, 1998.

[131] A. P. Dempster. A selection of early statistical papers of j. neyman. university of california press, berkeley, 1967. *Science*, 160(3828):661–663, 1968.

[132] Hirokazu Ishida et al. Study of hadron interactions in a lead-emulsion target. *PTEP*, 2014(9):093C01, 2014.

[133] A. Longhin, A. Paoloni, and F. Pupilli. Large-angle scattering of multi-GeV muons on thin Lead targets. *IEEE Trans. Nucl. Sci.*, 62(5):2216–2225, 2015.

[134] N. Agafonova et al. Procedure for short-lived particle detection in the OPERA experiment and its application to charm decays. *Eur. Phys. J.*, C74(8):2986, 2014.

[135] G. E. Masek, L. D. Heggie, Y. B. Kim, and R. W. Williams. Scattering of 2-Bev/c Muons in Carbon and Lead. *Phys. Rev.*, 122:937–948, 1961.

[136] Eduardo Medinaceli. A neutrino interaction with two vertices topology detected by OPERA. In *NuPhys2015: Prospects in Neutrino Physics (NuPhys) London, UK, December 16-18, 2015*, 2016.

[137] Marco Roda. Appearance of rare physics phenomena in the OPERA neutrino experiment. *PoS*, NEUTEL2015:081, 2015.

[138] D.V. Zaykin, Lev A. Zhivotovsky, P.H. Westfall, and B.S. Weir. Truncated product method for combining p-values. *Genetic Epidemiology*, 22(2):170–185, 2002.

[139] Roostats: https://twiki.cern.ch/twiki/bin/view/roostats/webhome.

[140] A. Bertolin U. Kose A. Longhin, A. Paoloni. Studies on the charge of the penetrating track of the third OPERA ν_τ candidate. *OPERA public note*, 161, 13 November 2013.

[141] Byron P. Roe, Hai-Jun Yang, Ji Zhu, Yong Liu, Ion Stancu, and Gordon McGregor. Boosted decision trees, an alternative to artificial neural networks. *Nucl. Instrum. Meth.*, A543(2-3):577–584, 2005.

[142] Hai-Jun Yang, Byron P. Roe, and Ji Zhu. Studies of boosted decision trees for MiniBooNE particle identification. *Nucl. Instrum. Meth.*, A555:370–385, 2005.